

REPORT DOCUMENTATION PAGE

Form Approved
OMB No. 0704-0168

Public reporting burden for this collection of information is estimated to be 1 hour per response, including the time for reviewing instructions, searching existing data sources, gathering and maintaining the data needed, and completing and reviewing the collection of information. Send comments regarding this burden estimate or any other aspect of this collection of information, including suggestions for reducing this burden, to Washington Headquarters Services, Directorate for Information Operations and Reports, 1215 Jefferson Davis Highway, Suite 1204, Arlington, VA 22202-4302, and to the Office of Management and Budget, Paperwork Reduction Project, O-124-0188, Washington, DC 20503.

1. AGENCY USE ONLY (leave blank)	2. REPORT DATE	3. REPORT TYPE AND DATES COVERED
	28 Dec 93	Final 15 Sep 93 - 14 Sep 93
4. TITLE AND SUBTITLE		5. FUNDING NUMBERS
Multiple scale Methods for stability Analyses of fluid-structure systems (u)		F49620-92-J-0505
6. AUTHOR(S)		
A. K. Liu		
7. PERFORMING ORGANIZATION NAME(S) AND ADDRESS(ES)		8. PERFORMING ORGANIZATION REPORT NUMBER
Dept of Mechanical Engineering Northwestern University Evanston, IL 60208		AFOSR-TR-94-0690
9. SPONSORING/MONITORING AGENCY NAME(S) AND ADDRESS(ES)		10. SPONSORING/MONITORING AGENCY REPORT NUMBER
AFWRI/VA Building 423, DC 20330-0001		DTIC ELECTED DEC 09 1994 F
11. SUPPLEMENTARY NOTES		
12a. DISTRIBUTION/AVAILABILITY STATEMENT		
Approved for public release; distribution is unlimited		
13. ABSTRACT (Maximum 200 words)		
<p>Multiple scale methods, which are based on discrete and continuous reproducing kernels, wavelets, and integral window transforms are developed. In this development, a microscope is constructed with a flexible space-time localized window function which translates and dilates in space and time to cover the entire domain of interest. This microscope can magnify, examine, and record the image of the various scales and frequencies of the response locally within the support of the window function. The degree of magnification will depend on the power of the microscope, a flexible space-scale and time-frequency window function. This complete characterization of the unknown response is performed through the integral window transform. This localization process can be achieved by dilating the flexible multiple-scale window function. The zoom in and zoom out capability of the window function is especially useful in examining complex flow phenomena, such as flow induced vibration, dynamic stability of flow-structure interaction, turbulence structures, and high frequency structural dynamics response.</p>		

14. SUBJECT TERMS	15. NUMBER OF PAGES	
Multiple scale Methods, integral transforms, wavelets	91	
16. PRICE CODE		
17. SECURITY CLASSIFICATION OF REPORT	18. SECURITY CLASSIFICATION OF THIS PAGE	19. SECURITY CLASSIFICATION OF ABSTRACT
Unclassified	Unclassified	Unclassified
20. LIMITATION OF ABSTRACT		

NSN 7540-01-280-5500

Standard Form 298 (Rev. 2-89)
Prescribed by ANSI Std Z39-18
298-102

REPORT DOCUMENTATION PAGE

Final Report on

Multiple Scale Methods for Stability Analysis of Fluid-Structure Systems

From September 15, 1992 - September 14, 1993

by

Professor Wing Kam Liu

Principal Investigator

Northwestern University

Department of Mechanical Engineering

2145 Sheridan Road

Evanston, Illinois, 60208

AFOSR Grant Number F49620-92-J-0505

Accesion For	
NTIS	CRA&I
DTIC	TAB
Unannounced	
Justification _____	
By _____	
Distribution / _____	
Availability Codes	
Dist	Avail and/or Special
A-1	

Abstract

Multiple scale methods, which are based on discrete and continuous reproducing kernels, wavelets, and integral window transforms are developed. In this development, a microscope is constructed with a flexible space-time localized window function which translates and dilates in space and time to cover the entire domain of interest. This microscope can magnify, examine, and record the image of the various scales and frequencies of the response locally within the support of the window function. The degree of magnification will depend on the power of the microscope, a flexible space-scale and time-frequency window function. This complete characterization of the unknown response is performed through the integral window transform. This localization process can be achieved by dilating the flexible multiple-scale window function. The zoom in and zoom out capability of the window function is especially useful in examining complex flow phenomena, such as flow induced vibration, dynamic stability of flow-structure interaction, turbulence structures, and high frequency structural dynamics response.

Introduction

Traditionally, researchers in computational analysis have concentrated on bringing more detail into their structural system models, but have ignored the multi-time and multi-spatial scales inherent in the structural response. To obtain resolution of medium frequencies, finite element meshes consisting of several thousand structural and continuum elements are necessary. To resolve the problem in the time domain, either a very small integration time step is required or if modal superposition is used a large number of structural eigenmodes is called for. These solutions often require hours of computer time on even the latest supercomputers. This severely limits the usefulness of these computations since their use in the design process is almost impossible.

Conversely, researchers in structural design and analysis have concentrated on the modeling of various structural components, usually via lumped parameters, but have often used drastic simplifications so that the multi-scales problem is eliminated; however, the accuracy of these methods is limited to the very low end of the spectrum.

In fluid-structure stability problems, the unstable response often arises from a coupling between phenomena associated with substantially different frequencies. For example, vortex formation in a flow about a blade or airfoil is initiated by relatively high frequency modes of the structure. The excitation forces generated by the vortex and the instability itself generally involve low modes of structural response. The complete time integration of the equations for the fluid and structure combined can be prohibitively time-consuming in even two dimensions and is beyond the capability of even the largest supercomputers in three dimensions. Thus it can be seen that methods which can effectively treat problems with large ranges in scale are needed in many types of analysis which arise in structural dynamics problems. This report is aimed at developing such methods and in studying their applications to a class of structural dynamics problems.

The Following papers have been presented at the 1993 ASME Winter Annual Meeting in New Orleans. These papers (2) are being extended and will be submitted for possible publication in International Journals.

(1) Liu, W. K., Adee, J., Jun, S., and Belytschko, T., "Reproducing Kernel Particle Methods for Elastic and Plastic Problems," , *Advanced Computational Methods for Material Modeling*, Eds. Benson, D. J. , and Asaro, R. A., AMD 180 and PVP 268, ASME, pp. 175-190, 1993.

(2) Liu, W. K., and Oberste-Brandenburg, C., "Reproducing Kernel and Wavelet Particle Methods," *Aerospace Structures: Nonlinear Dynamics and System Response*, Eds. Cusumano, J. P., Pierre, C., and Wu, S. T., AD 33, ASME, pp. 39-56, 1993.

The following papers have been or will be submitted to **Journals** for possible publications.

(1) Liu, W. K., Zhang, Y. F., Belytschko, T., Jun, S., Adee, J., and Gu, L., "Reproducing Kernel Particle Methods," submitted to *International Journal of Numerical Methods in Fluids*.

(2) Liu, W. K., Chen, Y. J., and Oberste-Brandenburg, C., "Reproducing Kernel and Wavelet Particle Methods," under preparation.

(3) Liu, W. K., Adee, J., Jun, S., and Belytschko, T., "Reproducing Kernel Particle Methods for Structural Dynamics," under preparation.

The above three papers are given below.

Reproducing Kernel and Wavelet Particle Methods

Wing Kam Liu, Fellow

and

Claus Oberste-Brandenburg

Northwestern University

Department of Mechanical Engineering

2145 Sheridan Road

Evanston, Illinois, 60208

Presented at the 1993 ASME Winter Annual Meeting, New Orleans. Appeared in the Book "Aerospace Structures: Nonlinear Dynamics and System Response" Eds. J. P. Cusumano, C. Pierre, and S. T. Wu. ASME, AD-Vol. 33, p. 39-56, 1993.

This research is supported by AFSOR Grant number F49620-92-J-0505

Abstract

Multiple scale methods, which are based on discrete and continuous reproducing kernels, wavelets, and integral window transforms are developed. In this development, a microscope is constructed with a flexible space-time localized window function which translates and dilates in space and time to cover the entire domain of interest. This microscope can magnify, examine, and record the image of the various scales and frequencies of the response locally within the support of the window function. The degree of magnification will depend on the power of the microscope, a flexible space-scale and time-frequency window function. This complete characterization of the unknown response is performed through the integral window transform. This localization process can be achieved by dilating the flexible multiple-scale window function. The zoom in and zoom out capability of the window function is especially useful in examining complex flow phenomena, such as flow induced vibration, dynamic stability of flow-structure interaction, turbulence structures, and high frequency structural dynamics response.

1. Introduction

In a compressible flow-structure system, the unstable response often arises from a coupling between phenomena associated with substantially different frequencies. For example, vortex formation in a flow about a blade or an airfoil is initiated by relatively high frequency modes of the structure. The excitation forces generated by the vortex and the instability itself generally involve low modes of structural response. The complete time integration of the equations for the compressible fluid and structure combined can be prohibitively time-consuming in even two dimensions and is beyond the capability of even the largest supercomputers in three dimensions. Thus it can be seen that methods which can effectively treat problems with large ranges in scale are needed in many types of analysis which arise in structural dynamics problems.

The development of computational methods for low-frequency response 3D structural systems are now reasonably well established. On the other hand, little success has been made in the structural area characterized by multiple scales, where response is often dominated by the middle part of the spectrum. The author believes that the multiple-scale reproducing kernel particle methods coupled with wavelets proposed here have great promise in dealing effectively with the difficult structural response problems in which the medium frequencies are important, such as problems involving impact, dynamic instability, compressible flow-structure interaction, and other local phenomena.

Because the frequency shift enables the time step to depend only on the size of the frequency band and *not* on the frequency extent of the load, these methods will speed up analysis of medium frequency response immensely. This is particularly attractive for structural response exhibiting multiple time scales. This new development will enable engineers not only to bring more detail into their structural system models, but will also enhance the computer simulations of many classes of multi-scale structural dynamics analysis. It will improve the accuracy, efficiency, and reliability of dynamic analysis.

In the next section, a review of the coupled compressible flow-structure interaction is presented. In section 3, the weak form of the equations of motion is given and some currently available solution methods are discussed. In section 4a, the discrete orthogonal reproducing kernel interpolation functions are reviewed. In section 4b, the multi-resolution wavelets analysis is given. In section 5, we present our proposed approach to study complex structures, the multiple scale reproducing kernel particle methods. Sample examples are given in section 6.

2. Review of Coupled Compressible Flow-Structure Interaction

The ability to solve general classes of fluid-structure interaction problems involving finite deformations and stability depends upon the ability to solve the corresponding uncoupled fluid and structural problems, and also the ability to interface fluid and structural subdomains. During the last two decades, considerable progress has been made in the solutions of free and moving boundary problems which involve large fluid deformations. Among these methods are the marker-and-cell (MAC) methods (Hirt [1975, 1983], Nichols and Hirt [1971], Harlow and Welch [1965]), the volume of fluid (VOF) methods (Amsden and Harlow [1970], Harlow et al. [1976]), moving mesh techniques (Subbiah et al [1989]), Eulerian and arbitrary Lagrangian-Eulerian (ALE) methods (Liu et al. [1988, 1991], Huerta and Liu [1988], Belytschko [1983], Belytschko and Kennedy [1978]), the smoothed particle hydrodynamic (SPH) methods and the free Lagrange methods (Monaghan and Gingold [1983], Gingold and Monaghan [1982], Burton and Harrison [1991]). However, the coupling of these methods with deformable structures is not well understood and often causes difficulties.

In the MAC method, a fixed or Eulerian mesh is used for the fluid calculation and a Lagrangian set of marker particles is used to trace the moving free surface. Marker particles can be spread over all fluid occupied regions with each particle specified to move with the fluid velocity at its location. A free surface is defined as lying at the "boundary" between regions with and without marker particles. More specifically, a mesh is said to contain a free surface if the mesh contains cells with markers and has at least a neighboring cell with no markers. The MAC method offers the distinct advantage of eliminating all logic problems associated with intersecting surfaces. This method is also readily extendable to three dimensional computations. However, the MAC method requires significant increase in running time and storage.

In the VOF approach, a function F is defined whose value is unity at any point fully occupied by fluid and zero otherwise. Cells with F values between zero and one must then contain a free surface. This fractional volume of fluid (VOF) method provides the same coarse interface information available in the marker particle method. In order to trace the free surface, a flow analysis network approach is developed. It uses the flux calculation at the boundary of each control volume to check the fraction of fill instead of tracking marker particles. One limitation of this control volume technique is that the time step must be controlled to ensure that free surface only passes one control volume in a time step.

In a moving mesh approach, a numerical grid generation scheme, which facilitates solutions over arbitrarily shaped boundaries, has to be developed. This approach numerically maps the irregular shape of the flow field to a more regular shape in a computational domain

where the governing equations are solved. The computation time of this method is relatively high because of the large number of time steps and the mesh generation at each time step.

There are two approaches to ALE methods. One approach updates the solution variables in a single time step while the other performs a Lagrangian step followed by an Eulerian or remap (or advection) step. The latter strategy is often referred to as an operator split method. Similar to the moving mesh approach, a new mesh is required for the ALE calculations. However, this new mesh is required only if the Lagrangian mesh is too distorted. The major advantage of the ALE methods is the moving boundaries can be computed with high accuracy of the Lagrangian method, and the mesh can conserve its regularity in avoiding element entanglement. Although a combination of multi-material ALE methods have also been developed, the application of this technique to multiple free surfaces, multiple materials, and fluid-structure interaction remains to be explored.

The SPH (smooth particle hydrodynamics) and the free Lagrange methods are based on algorithms which are truly grid-free or mesh-free. Consequently, these techniques do not have the mesh entanglement problems and at the same time, maintain the high accuracy of the Lagrangian calculations. Similar to a finite difference/element Lagrangian calculation, the continuous fluid is approximated by a set of particles or fluid elements of equal mass. Unlike the traditional Lagrangian finite element/difference calculations, the inter-particle forces among these smooth fluid particles are derived from the pressure and these interacting pressure forces are governed by an interpolating function. Hence, the nodal or element forces (which are usually constructed from a finite element/difference mesh) are no longer needed; and consequently, these free Lagrange methods require no mesh and the mesh distortion problems are completely eliminated. The energy equation is similarly defined for each smooth fluid particle. Since the fluid is modeled by equal mass particles, the density for the fluid is constructed by defining a weighting function in which the density of the equal mass particles is proportional to the number of particles per unit volume. With these approximations, the motion of the fluid is governed by the movement of this set of smooth fluid particles, and the movement of the particles are governed by the particle interacting forces.

Although SPH methods work well if there is no boundary (since the boundary terms are tossed out in the formulation, Libersky and Petschek [1990]), and when the number of unknowns (nodes) is large; SPH methods are not as accurate as the regular finite element methods, Johnson, Peterson and Stryk, [1993]. From our study of SPH interpolation function via a simple one dimensional (1D) Galerkin formulation, we found that there is an additional deficiency in the SPH formulation. It is related to the boundary correction term of the reproducing kernel approximation. We shall make an attempt to identify this deficiency and present our view of improving the SPH kernel approximation.

After reviewing the moving least square interpolation functions, Lancaster and Salkauskas [1981], and the diffuse element methods (DEM), Nayroles et al. [1992]. Belytschko et al. [1993] pointed out that an assumption made by Nayroles et al., the interpolation coefficients are constants, detracts from the accuracy of the method. They developed the Element Free Galerkin Methods (EFGM) and showed that by adding more accurate derivatives and enforcing boundary conditions by Lagrange multipliers, the methods could achieve very high rates of convergence. From our experience, EFGM are more accurate than the finite element methods, and hence, the SPH methods especially for a small set of nodes. One main drawback of EFGM is the computational expense, and we found that it is more computationally intensive than the SPH methods.

The objective of the Reproducing Kernel Particle Methods developed by Liu et al. [1993], is along the same line of development as the SPH, DEM, and EFGM : to develop an accurate and efficient mesh free interpolation functions. A detailed discussion on smooth particle methods, the diffuse element methods and the element free Galerkin method, and the recently developed reproducing kernel particle methods, is also given in the paper.

Since a continuous reproducing kernel can be derived for this method and it is also a free Lagrange particle method, we shall label this development as *Reproducing Kernel Particle Methods* (RKPM). This proposed approach is motivated by the theory of wavelets Chui [1992] and Daubechies [1992], in which a function is represented by a combination of the dilation and translation of a single wavelet, which is a window function. In a wavelet analysis, similar to the SPH interpolation kernel, the interpolation coefficients are defined in terms of the integral window transform of the window function and the solution itself. In this proposed study, we shall make use of the multiple frequency bands and/or multiple scales properties of wavelets analysis (multi-resolution analysis), and the time-frequency and/or space-scale localization properties of the continuous and discrete reproducing kernel approximations.

3. Weak Form of the Equation of Motion and Solution Methods

Consider the weak form of the equations of motion which can be written as:

$$K \langle \delta u^h, u^h \rangle + B \langle \delta u^h(x \in \Gamma_g), u^h(x \in \Gamma_g) - g(x) \rangle = f \langle \delta u^h, p \rangle \quad (3.1)$$

where $K \langle \cdot, \cdot \rangle$, $B \langle \cdot, \cdot \rangle$ and $f \langle \cdot, \cdot \rangle$ are the usual weak form operator of the governing equations, boundary constraint operator on Γ_g , and the force assembly operator, respectively. $\delta u^h(x, t)$, $u^h(x, t)$, $p(x, t)$ and $g(x, t)$ are the test function, trial function, body force, and prescribed data on the boundary Γ_g . The governing equations can be those of structural

dynamics, fluid dynamics, coupled-fluid-structure interaction or structural acoustics, and among others. The classical Galerkin method is to approximate u^h (which is the approximation to $u(x, t)$) by:

$$u^h(x, t) = \sum_{a=1}^A C_a \phi(x - x_a) \quad (3.2a)$$

and

$$\delta u^h(x, t) = \sum_{a=1}^A \delta C_a \phi(x - x_a) \quad (3.2b)$$

where $\phi(x - x_a)$ can be the global finite element shape functions, Hughes [1987], spectral functions Gottlieb and Orszag [1977], the smooth particle hydrodynamic (SPH) interpolation kernel function, Lucy [1977] and Monaghan [1988], multiple scale finite element functions Liu, Zhang and Ramirez [1991], or wavelet-type bases, Chui [1992] and Daubechies [1992], etc. Substitute Eqs. (3.2) into Eq. (3.1) and solve for C_a for $a = 1, \dots, A$ coefficients will result in the discrete approximation of $u(x)$, provided certain continuity requirements are met.

It is noted that the above solution procedures also hold for the various approaches such as the space-time discontinuous finite elements, Hughes and Hulbert [1988], and Shakib and Hughes [1991], deforming space-time discontinuous finite elements, Tezduyar, Behr and Liou [1992]; the arbitrary Lagrangian-Eulerian (ALE) and Eulerian-type finite element methods, Liu et al. [1991], and among others. All these methods employ the same type of interpolations, Eqs. (3.2), except a new set of motion, mesh motion, is introduced through similar equations (3.2). This additional motion is used to control the mesh or grid deformation so that mesh distortion can be minimized and the nodal points connectivity through the mesh or grid description would not give negative Jacobians, Liu et al. [1988].

Equations (3.2) give a good approximation to $u(x, t)$ when the measure of the spacing among x_a , call it h , becomes smaller and smaller. One can then visualize the coefficient C_a as an average value of $u(x, t)$, and $\phi(x - x_a)$ is the weighting function. If h approaches to zero C_a approaches to the true solution at x_a . However, in practice, h does not approach zero and if $u(x, t)$ is a very nonlinear function, solving for the average values, as all of these methods do, would probably leave out the fine details of the response $u(x, t)$.

Therefore, our objective is, instead of solving for the averaged $u(x_a)$ (i.e., C_a), we shall develop an alternative form of Eqs. (3.2), which is based on discrete reproducing kernels and

integral window transforms. In this approach, if we include the time dimension into \mathbf{x} , we can think of $\phi(\mathbf{x} - \mathbf{x}_a)$ as a flexible space-time window function located at \mathbf{x}_a . Since $u(\mathbf{x})$ is an unknown function, our goal then is to interpret the coefficient C_a as a microscope which magnifies, examines, and records the image of the response $u(\mathbf{x})$ around \mathbf{x}_a . This can be achieved by employing a space-time localized window function that can recover the various scales and frequencies of the response $u(\mathbf{x})$ locally around \mathbf{x}_a . This leads us to the use of scaling functions and wavelets which are discussed in the next two sections.

4a. Discrete Orthogonal Reproducing Kernel Interpolation Functions

If $\phi(\mathbf{x} - \mathbf{x}_a)$ is chosen to be the scaling function, Chui [1992], C_a is identified as the integral window transform of the unknown response u and $\phi(\mathbf{x} - \mathbf{x}_a)$ over the domain. That is, the unknown coefficients are to be constructed so that:

$$C_a = C_a(u, \mathbf{x}_a) = \langle u, \phi_a \rangle = \int_V u(\mathbf{x}) \phi(\mathbf{x} - \mathbf{x}_a) d\mathbf{x} \quad (4.1)$$

where $\langle u, \phi_a \rangle$ is the integral window transform, and V is the domain of interest. The reconstruction formula Eq. (3.2a) becomes:

$$u^h(\mathbf{x}, t) = \sum_{a=1}^A \langle u, \phi_a \rangle \phi(\mathbf{x} - \mathbf{x}_a) \quad (4.2)$$

Equation (4.2) is typical for a discrete reproducing kernel Hilbert space. In seeking for the solution $u^h(\mathbf{x}, t)$ using Eq. (4.2) and a similar equation for $\delta u^h(\mathbf{x})$, it is necessary to define nodal point \mathbf{x}_j ; nodal $u_j \equiv u(\mathbf{x}_j)$; and particles with nodal mass ΔM_j and nodal density ρ_j . Consequently, the nodal volume ΔV_j is determined by $\Delta M_j / \rho_j = \Delta V_j$ for $j = 1, \dots, NP$, where NP is the total number of particles inside V . Hence,

$$\sum_{j=1}^{NP} \Delta V_j = V ; \quad \text{and} \quad \sum_{j=1}^{NP} \Delta M_j = \text{total mass} \quad (4.3)$$

Using numerical integration in Eqs. (4.2) and the above definitions, $u^h(\mathbf{x}, t)$ becomes:

$$u^h(\mathbf{x}, t) = \sum_{a=1}^A \langle u, \phi_a \rangle \phi(\mathbf{x} - \mathbf{x}_a)$$

$$= \sum_{a=1}^A \left[\sum_{x_j \in B(x_a)} \phi(x_j - x_a) \Delta V_j u_j(t) \right] \phi(x - x_a) \quad (4.4)$$

where x_j are the quadrature points, and $B(x_a)$ is the support of $\phi(x - x_a)$. Equation (4.4) is a discrete reproducing kernel approximation (DRKA), since $u^h(x, t)$ is interpolated via $\phi(x - x_a)$ through the integral window transform of $u(x, t)$. An interesting interpretation of Eq. (4.4) is as follows. There are a total of A sampling windows spread over the domain V . At each sampling location x_a , a microscope, which is constructed from the integral window transform $\langle u, \phi_a \rangle$, examines the motion of particles ΔM_j carrying nodal values u_j passing through the support $B(x_a)$. If the motion is very nonlinear, the number of "free Lagrange particles" ΔM_j passing through each sampling window $\phi(x - x_a)$ is different from time to time. Therefore, Eq. (4.4) maintains the attributes of the free Lagrange methods, and with the appropriate choice of $\phi(x - x_a)$, gives more accurate results.

Upon examining Eq. (4.4), since only a set of nodal points or particles are involved in DRKA methods, similar to SPH methods, DRKA methods have no problems associated with mesh/grid distortion or negative Jacobian of the elements resulting from large deformation. Hence, it is suitable for large deformation and high velocity flow problems. However, unlike SPH methods in which $\phi(x - x_a)$ in Eq. (3.2a) is the interpolation kernel function that mimic a Dirac Delta function and C_a is the product of the nodal mass ΔM_a and the nodal value of the response u_a ($\approx u(x_a)$) divided by the nodal density ρ_a , (Monaghan [1988]). That is

$$u^h(x, t) = \sum_{a=1}^A \phi(x - x_a) \frac{\Delta M_a}{\rho_a} u_a \equiv \sum_{a=1}^A \phi(x - x_a) \Delta V_a u_a \quad (4.5)$$

Comparing Eqs. (4.4) and (4.5), if only one point integration is used to integrate the integral window transform $\langle u, \phi_a \rangle$, which is a very bad approximation to the integral, especially for very nonlinear or complex $u(x, t)$, the SPH and DRKA methods take a similar form. However, if more than one point quadratures are employed to evaluate the integral window transform $\langle u, \phi_a \rangle$, the difference between the two methods is apparent. It is thus clear from Eq. (4.4) why we call C_a a microscope in which the magnification power will depend on the number of particles examined under the support $B(x_a)$.

4b. Multi-Resolution Wavelets Analysis

In this section, we wish to construct and interpret C_a as a *flexible* power microscope. This microscope can zoom in (sharpen the window function) to pick up the detailed structures of the response $u(x)$; and zoom out (widen the window function) if no further magnification of the response is necessary. This zoom in and zoom out capability is especially useful in examining complex flow phenomena, such as flow induced vibrations; dynamic stability of flow-structure interaction, turbulence structures, structural acoustics, high frequency structure dynamic response, strain localization problems, and other engineering disciplines.

In this development, since C_a is defined in terms of the unknown response $u(x)$ and the multiple scale window function $\phi(x-x_a)$, Eq. (4.2) has to be redefined for the multi-resolution wavelets analysis. The window functions $\phi(x-x_a)$ will be replaced by flexible power window functions $\psi_{ma}(x)$; whereas the integral window transform coefficients $C_a = \langle u, \phi_a \rangle$, $a = 1, \dots, A$, become C_{ma} , which are defined by $\langle u, \psi_{ma} \rangle$. The power of the window function is controlled by an index $m = 0, 1, \dots, M$. The multi-resolution analysis is performed simply by the dilation of the window functions. That is, the discrete reproducing kernel formula Eq. (4.2) can be re-defined as:

$$u^h(x) = \sum_{m=0}^M \sum_{a=1}^{A_m} \langle u, \psi_{ma} \rangle \psi_{ma}(x) = \sum_{m=0}^M \sum_{a=1}^{A_m} C_{ma} \psi_{ma}(x) \quad (4.6a)$$

where the dilation of $\psi_{ma}(x)$ is defined through the integer index m , and $A_0 > A_1 > \dots > A_M$. The arbitrary scale, $a_0 > 0$, is usually set equal to 2. Hence, the flexible space-time and scale-frequency window functions are defined by:

$$\psi_{ma}(x) = a_0^{-m/2} \psi(a_0^{-m}(x-x_a)) \quad a_0 > 0 \quad (4.6b)$$

and the integral window transform $\langle u, \psi_{ma} \rangle$ is given by:

$$C_{ma} = \langle u, \psi_{ma} \rangle = \int_V \psi_{ma}(x) u(x) dx \quad (4.6c)$$

where V is the space (or space-time) domain of interest.

As can be seen from Eq. (4.6b), the mother wavelet $\psi(x)$ can be obtained by setting $m = 0$ and $x_a = 0$. Because of our choice of indexing, $m = 0$ corresponds to the smallest window width. The integral window transform $\langle u, \psi_{0a} \rangle$, the microscope, can pick up the very fine scale and/or high frequencies up to the arbitrary scale a_0 . For $m = M$, it corresponds to the

largest window width, and $C_{Ma} = \langle u, \psi_{Ma} \rangle$, the microscope, can pick up the large scale and/or low frequency response.

It is apparent from Eqs. (4.6) that the microscope C_{ma} located at \mathbf{x}_a can examine the finest scales of $u(\mathbf{x})$ simply by dilation. The magnification factor is determined by the mother window function, and the flexible space-scale and time-frequency localized integral window transform $\langle u, \psi_{ma} \rangle$.

Using a numerical quadrature integration scheme to discretize Eq. (4.6c) gives:

$$C_{ma} = \langle u, \phi_{ma} \rangle = \sum_j \int_{x_j \in B^m(x_a)} \psi_{ma}(\mathbf{x}_j) \Delta V_j u, \quad (4.7a)$$

where $B^m(x_a)$ is the support of the m^{th} scale window function located at \mathbf{x}_a and ΔV_j is the j^{th} nodal volume evaluated at \mathbf{x}_j . Substituting Eq. (4.7a) into Eq. (4.6a), we obtain our desired discrete multi-resolution wavelet analysis of $u(\mathbf{x})$:

$$u^h(\mathbf{x}) = \sum_{m=0}^M \sum_{a=1}^{A_m} \left\{ \int_{x_j \in B^m(x_a)} \psi_{ma}(\mathbf{x}_j) \Delta V_j \psi_{ma}(\mathbf{x}) \right\} u_j \quad (4.8)$$

Similar equation can also be written for $\delta u^h(\mathbf{x})$. Equation (4.8) can be written in a more familiar form of multi-resolution analysis:

$$u^h(\mathbf{x}) = \sum_{m=0}^M u_m^h(\mathbf{x}) = u_0^h(\mathbf{x}) + u_1^h(\mathbf{x}) + \cdots + u_M^h(\mathbf{x}) \quad (4.9a)$$

It can be seen from Eq. (4.7a) that $u^h(\mathbf{x})$ is a direct sum of the M -scale solution. For each refinement m , the m^{th} -scale interpolation, which also represents the m^{th} -frequency/wave number band of the solution, is defined by:

$$u_m^h(\mathbf{x}) = \sum_{a=1}^{A_m} u_{ma}^h(\mathbf{x}) = u_{m1}^h(\mathbf{x}) + u_{m2}^h(\mathbf{x}) + \cdots + u_{mA_m}^h(\mathbf{x}) \quad (4.9b)$$

From Eq. (4.9b), we can view each $u_{ma}^h(\mathbf{x})$ as a flexible power microscope examining $u(\mathbf{x})$ around \mathbf{x}_a and each $u_{ma}^h(\mathbf{x})$ is interpolated through the window function so that:

$$u_{ma}^h(x) = \sum_J \frac{x_J \epsilon B^m(x_a)}{N_{maJ}(x)} u_J \quad (4.9c)$$

and the m^{th} scale- a^{th} wavelet shape function ($N_{maJ}(x)$) of particle J is given by (no sum on m, a and J):

$$N_{maJ}(x) = \psi_{ma}(x_J) \Delta V_J \psi_{ma}(x) \quad (4.9d)$$

From Eq. (4.9c), the summation on J for $x_J \in B^m(x_a)$ will define the global nodal connectivity. However, unlike the usual finite element, the sequence of numbering u_J would not cause any mesh distortion or negative Jacobian problems since there is no element.

If additional particles are added to the domain (this can easily be done by splitting up particles), the adaptive multi-resolution analysis can be summarized as follows:

$$u^h(x) = \sum_{m=0}^M u_m^h(x) \quad \text{multi-resolution analysis} \quad (4.10a)$$

$$= \sum_{m=0}^M \left(\sum_{a=1}^{A_m} u_{ma}^h(x) \right) \quad \text{summation of all frequency bands of interest} \quad (4.10b)$$

$$= \sum_{m=0}^M \left(\sum_{a=1}^{A_m} \left[\sum_J \frac{x_J \epsilon B^m(x_a)}{N_{maJ}(x)} u_J \right] \right) \quad u_J \text{ are examined by the } m^{\text{th}} \text{ scale-}a^{\text{th}} \text{ wavelet under } B^m(x_a) \quad (4.10c)$$

$$= \sum_J \frac{x_J \epsilon B^m(x_a)}{\left\{ \sum_{m=0}^M \sum_{a=1}^{A_m} (\psi_{ma}(x_J) \Delta V_J \psi_{ma}(x)) \right\} u_J} \quad \text{global interpolation functions} \quad (4.10d)$$

As can be seen, there is no change in the multi-resolution analysis Eqs. (4.10a) and (4.10b), since the dilation index m and the number of window functions $\psi_{ma}(x)$ are the same. There is also no change in the order of the window function as $\psi_{ma}(x)$ is derived from $\psi_{0a}(x)$. The only change is in the summation on J under the support $B^m(x_a)$ and the resulting "nodal/particle" matrix will be larger because of the additional global interpolation functions of those nodes/particles. Similar procedures can also be developed for the deletion of particles.

If we can construct discrete multi-resolution wavelet functions according to Eqs. (4.10), we shall have a *truly mesh or grid-free adaptive* method and the interpolation is defined through a set of arbitrary-spaced nodal points or particles. Moreover, if $\psi(x)$ is chosen to be C^k smooth functions, i.e., smooth in its k^{th} derivatives, the discrete multi-resolution reproducing kernel interpolation functions are also C^k .

5. Multiple Scale Reproducing Kernel Particle Methods

The multi-resolution wavelet analysis given in sections 4 is based on an infinite domain assumption. To apply wavelets to analyzing complex structures, this restrictive assumption is no longer valid. Another intrinsic deficiency of orthogonal wavelet is the stringent requirement:

$$\int x^m \psi(x) dx = 0 \quad m = 0, 1, \dots, q \quad (5.1)$$

where q is the degree of polynomials of the mother wavelet $\psi(x)$. From Eq. (5.1) it follows that a q^{th} order wavelet can not represent $1, x, x^2, \dots, x^q$, parts of the solution. To remedy these two restrictions, we shall represent a function $u(x)$ by:

$$u(x) = u^w(x) + P(x)c \quad (5.2)$$

where $u^w(x)$ is the part of the solution that is obtained by the multi-resolution wavelet reconstruction as given in section 4b. $P(x) = \{P_1(x), P_2(x), \dots, P_n(x)\}$ and $c = \{c_1, c_2, \dots, c_n\}^T$ are the vectors of the n linear independent functions and unknown coefficients, respectively. A superscript T denotes the transpose. We can consider the $P(x)c$ term as the residual representation of $u(x)$ within a bounded domain. Following the procedures of deriving the reproducing kernel particle interpolation functions (see Liu et al.[1993]), the multiple scale reproducing kernel interpolation function coupled with wavelets can be shown to be:

$$\begin{aligned} u(x) = u^w(x) + & \int_v C(x, y, a_0) a_0^{-1} \phi\left(\frac{y-x}{a_0}\right) u(y) dy \\ & - \int_v C(x, y, a_0) a_0^{-1} \phi\left(\frac{y-x}{a_0}\right) u^w(y) dy \end{aligned} \quad (5.3)$$

where the parameter a_0 determines the size of the scaling function $\phi(x)$. The form of the correction function $C(x, y, a_0)$ will depend on the choice of $P(x)$. It is noted that the second term in Eq.(5.3) is the reproducing kernel approximation described in Appendix A. The first term is the multi-resolution wavelet part, whereas, the third term *connects* the two reproducing methods. It is interesting to point out that by a proper choice of a_0 , the contribution of the coupling term can be shown to be negligible. With this construction, the wavelet and the reproducing kernel terms give the high and low frequency (or the fine and coarse scales) representations of the solution u . It is also noted that $u^w(x)$ can be expressed by other continuous or discrete multiple scale reproducing kernels.

To further examine this multiple frequency/wave number bands wavelet approximation, we let

$$u^w(x) = \sum_{m=0}^M \sum_{a=1}^{A_m} \langle u, \psi_{ma} \rangle \psi_{ma}(x) \quad (5.4)$$

Substituting Eq.(5.4) into Eq. (5.3) yields:

$$\begin{aligned} u(x) = & \sum_{m=0}^M \sum_{a=1}^{A_m} \left\{ \int_v u(y) \psi_{ma}(y) dy \right\} [\psi_{ma}(x) - \tilde{\psi}_{ma}(x)] \\ & + \int_v C(x, y, a_0) a_0^{-1} \phi\left(\frac{y-x}{a_0}\right) u(y) dy \end{aligned} \quad (5.5)$$

where the definition of:

$$\langle u, \psi_{ma} \rangle = \int_v u(y) \psi_{ma}(y) dy \quad (5.6a)$$

has been used in Eq.(5.5). The approximation of the wavelet functions $\psi_{ma}(x)$ through the reproducing kernel, denoted by $\tilde{\psi}_{ma}(x)$ is:

$$\tilde{\psi}_{ma}(x) = \int_v C(x, y, a_0) a_0^{-1} \phi\left(\frac{y-x}{a_0}\right) \psi_{ma}(y) dy \quad (5.6b)$$

It is now clear from Eq. (5.6b) that $\tilde{\Psi}_{ma}(x)$ is simply an approximation of $\Psi_{ma}(x)$ via the reproducing kernel reconstruction. It is expected that $\tilde{\Psi}_{ma}(x)$ is very close to $\Psi_{ma}(x)$ for low frequency/wave number wavelets. Consequently, the contribution from the low frequency/wave number wavelets is close to zero. However, depending on the choice of a_0 , ϕ , and ψ ; the reproducing kernel might not be able to reconstruct the high frequency/wave number part of the solution (second term in Eq. (5.5)); and these high frequency/wave number components can be readily picked up by multi-resolution wavelets analysis.

Presently, we are working on the theoretical analysis of this type of reproducing kernel methods. Upon the understanding of Eqs. (5.6), we shall implement the correct ϕ , and ψ into the continuous multiple-scale frequency bands approximation of the response:

$$u^h(x) = \int_V C(x, y, a_0, a^m) a_0^{-1} \phi\left(\frac{y-x}{a_0}\right) u(y) dy \quad \text{low frequency band}$$

$$+ \sum_{m=1}^M \int_V C(x, y, a_0, a^m) a_0^{-m} \psi\left(\frac{y-x}{a^m}\right) u(y) dy \quad \text{high frequency band} \quad (5.7)$$

Unlike orthogonal wavelets, equation (5.7) holds for arbitrary domains. Discretization of Eq. (5.7) gives the desired multi-grid/multi-resolution analysis of the complex dynamic systems:

$$u^h(x) = \sum_{j=1}^{NP0} [C(x, x_j, a_0, a^m) \Delta x_j u_j] a_0^{-1} \phi\left(\frac{x_j-x}{a_0}\right) \quad \text{low frequency band}$$

scaling factor coefficients

$$+ \sum_{j=1}^{NP1} [C(x, x_j, a_0, a^m) \Delta x_j u_j] a^{-1} \psi\left(\frac{x_j-x}{a}\right) \quad 1\text{st higher frequency band}$$

1st-scale wavelet coefficients

$$\vdots$$

$$+$$

$$+ \sum_{j=1}^{NPM} [C(x, x_j, a_0, a^m) \Delta x_j u_j] a^{-M} \psi\left(\frac{x_j-x}{a^M}\right) \quad M^{\text{th}} \text{ higher frequency band} \quad (5.8)$$

Mth-scale wavelet coefficients

It is noted that $NPM \geq \dots \geq Np1 \geq np0$; and it constitutes an unstructured multi-grid analysis. We also wish to emphasize that orthogonal wavelets are not necessary; hence there is a larger class of window functions which can give good time and frequency localization.

6. Numerical Examples

The steady-state advection-diffusion problem can be stated for the one-dimensional case as follows:

$$u_{,xx} - au_{,x} = b(x) \quad \text{in } \Omega \quad (6.1)$$

with the boundary conditions

$$u(x_g) = u_1 \quad \text{on } \Gamma_g \quad (6.2a)$$

$$u_{,x}(x_b) = u'_2 \quad \text{on } \Gamma_b \quad (6.2b)$$

where Ω is the domain (i.e., $0 \leq x \leq L$), Γ_g is the boundary with essential boundary conditions and Γ_b the boundary with natural boundary conditions. The whole boundary is $\Gamma = \Gamma_g \cup \Gamma_b$ and $\Gamma_g \cap \Gamma_b = \{\emptyset\}$. $(\cdot)_{,x}$ denotes derivatives with respect to x . u is the scalar unknown, a a given constant, and $b(x)$ a given source term. The parameter a is the advective velocity divided by the diffusion coefficient. The Peclet number is therefore

$$Pe = \frac{a \Delta x}{2} \quad (6.2c)$$

The boundary conditions are given. This problem can be viewed as a heat transfer problem with convective and diffusive heat transfer. The source term $b(x)$ can be caused by a chemical reaction. Following Hughes et. al. [9] the weak form of equation (6.1) with the least square term can be written as

$$\int_{\Omega} w(u_{xx} - a u_{x} - b) d\Omega + \int_{\Omega} (w_{xx} - a w_x) \tau (u_{xx} - a u_x - b) d\Omega = 0 \quad (6.3)$$

where w is an arbitrary test function and τ is a parameter. Using the approximations u^h and w^h for the functions u and w , we obtain the usual matrix equation.

The following numerical examples use a highly irregular source term to cause a nonlinear solution with two peaks. The source term consists of two terms that are very similar and summed together. Each part is

$$\begin{aligned} b_i(x) = & \frac{2c_1c_2e^{c_1(x-x_0)}(e^{2c_2(x-x_0)}-1) \operatorname{Sech}(c_1(x-x_0))^2}{(e^{2c_2(x-x_0)}+1)^2} \\ & + \frac{2c_1^2 \operatorname{Sech}(c_1(x-x_0))^2 \operatorname{Tanh}(c_1(x-x_0))}{(e^{c_2(x-x_0)}+e^{-c_2(x-x_0)})} \\ & - \frac{c_2^2(e^{c_2(x-x_0)}+e^{-c_2(x-x_0)}) * (1-\operatorname{Tanh}(c_1(x-x_0)))}{(e^{c_2(x-x_0)}+e^{-c_2(x-x_0)})^2} \\ & + \frac{2c_2^2(e^{c_2(x-x_0)}-e^{-c_2(x-x_0)})^2 * (1-\operatorname{Tanh}(c_1(x-x_0)))}{(e^{c_2(x-x_0)}+e^{-c_2(x-x_0)})^3} \\ & + a \left(\frac{c_2(e^{c_2(x-x_0)}-e^{-c_2(x-x_0)}) (1-\operatorname{Tanh}(c_1(x-x_0)))}{(e^{c_2(x-x_0)}+e^{-c_2(x-x_0)})^2} + \frac{c_1 \operatorname{Sech}(c_1(x-x_0))^2}{(e^{c_2(x-x_0)}+e^{-c_2(x-x_0)})} \right) \end{aligned} \quad (6.4)$$

where the parameter x_0 governs the position of the peak, c_1 controls the sharpness on the right side of the peak and c_2 controls the decay on the left side. In the previous equation the second indice for the parameters x_0 , c_1 and c_2 is omitted. Therefore $x_0 = x_{0i}$, $c_1 = c_{1i}$ and $c_2 = c_{2i}$ for $i=1,2$.

The resulting source term is

$$b(x) = k_1 b_1(x) + k_2 b_2(x) \quad (6.5)$$

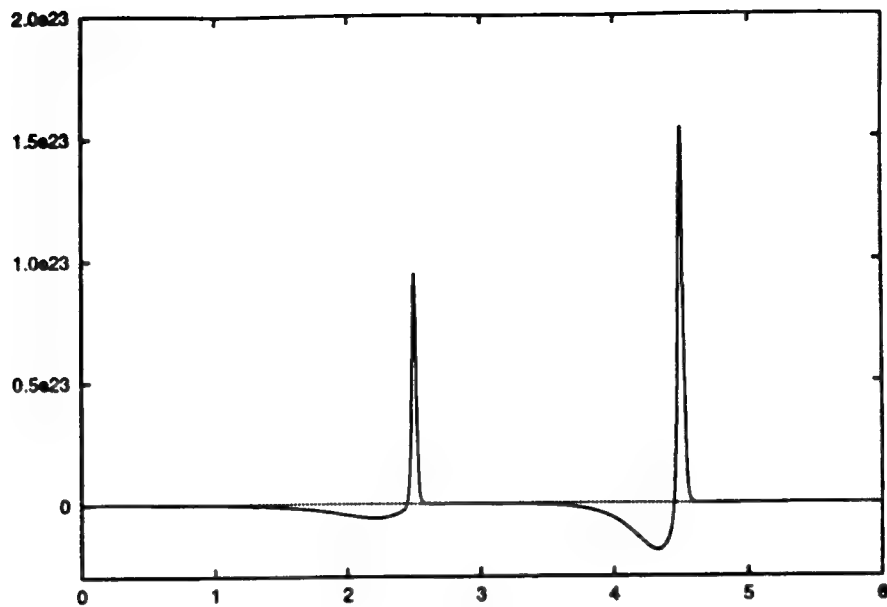


Figure 6.1 Source term used in the examples

with the parameters

i	1	2
x_{0i}	5.0	2.5
c_{1i}	50	50
c_{2i}	1.0	3.0
k_i	0.5	1.0

where the parameter k determines the size of the peak. The source term using these coefficients is shown in figure 6.1.

The homogeneous solution for the advection-diffusion equation on the domain $0 \leq x \leq 6$ with boundary conditions $u(0)=0, u(6) = 1$ becomes

$$u^H(x) = \frac{e^{ax} - 1}{e^{6a} - 1} \quad (6.6)$$

where the particular solution with $b(x)$ given in (6.17)

$$u^P(x) = k_1 u_1^P(x) + k_2 u_2^P(x) \quad (6.7)$$

where

$$u_i^P(x) = \frac{1 - \tanh(c_i(x - x_0))}{e^{c_i(x - x_0)} + e^{-c_i(x - x_0)}} \quad \text{for } i = 1, 2 \quad (6.8)$$

with the appropriate constants from the table above. The parameter a is set to $a=1000$ in the following examples.

The results for the diffusion equation were obtained by setting the parameter a to zero and setting the boundary conditions to $u(0)=0$, $u(6) = 0$.

The results for the Reproducing Kernel Method are obtained by using a Window function W of the form

$$W(z) = e^{-z^2} \quad (6.9)$$

and

$$a_0 = 2^j \Delta x \sqrt{\frac{2}{\pi}} \quad (6.10)$$

To show the influence of the parameter j , the solution of the differential equation is calculated for several j . Note that for $j=-2.2$ the solution becomes unstable and that for a $j<0$ the solution approaches the finite element solution.

Note that the wavelets are scaled with a factor Δx to scale the mother wavelet to the size of the mesh.

The solutions of the Diffusion Equation and the Advection Diffusion Equation using several different methods are shown in Figures 6.1 - 6.6 An error plot for the Diffusion Equation is shown in Figure 6.5. The solution for 31 nodes is not representative, the source term is underintegrated.

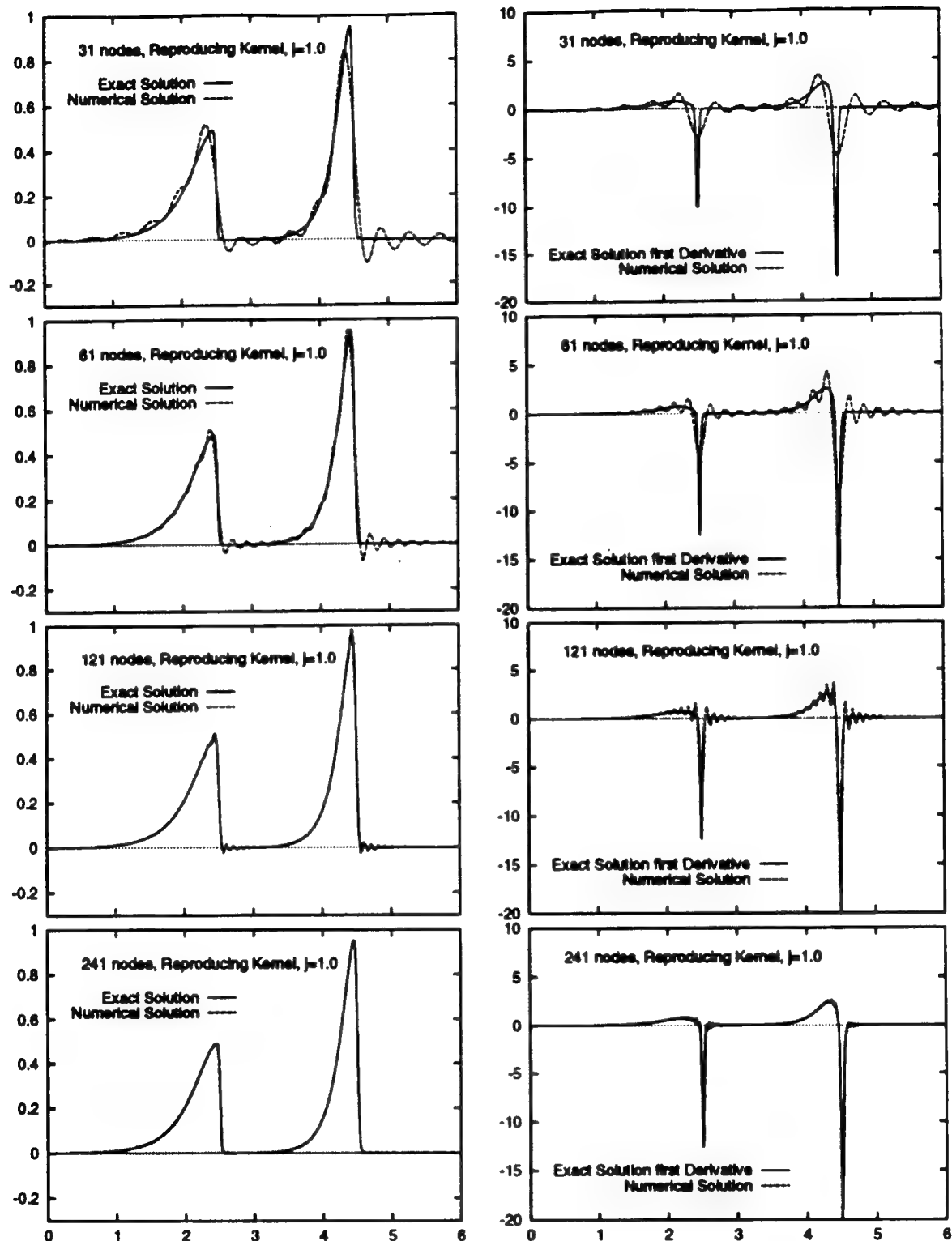


Figure 6.1 Solution of the Diffusion Equation
using Gaussian Reproducing Kernel with $j= 1.0$

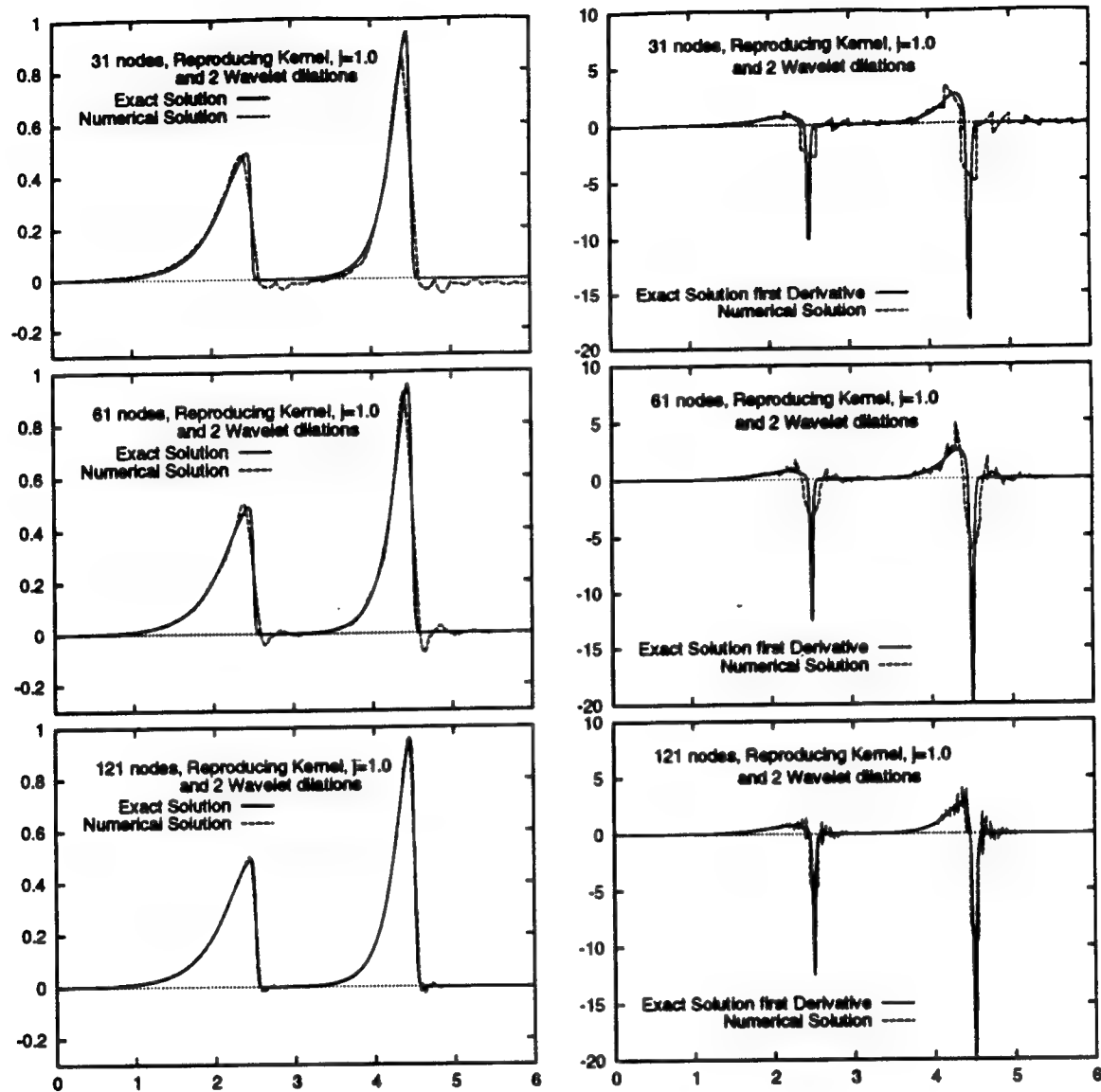


Figure 6.2 Solution of the Diffusion Equation
using two Wavelet dilations

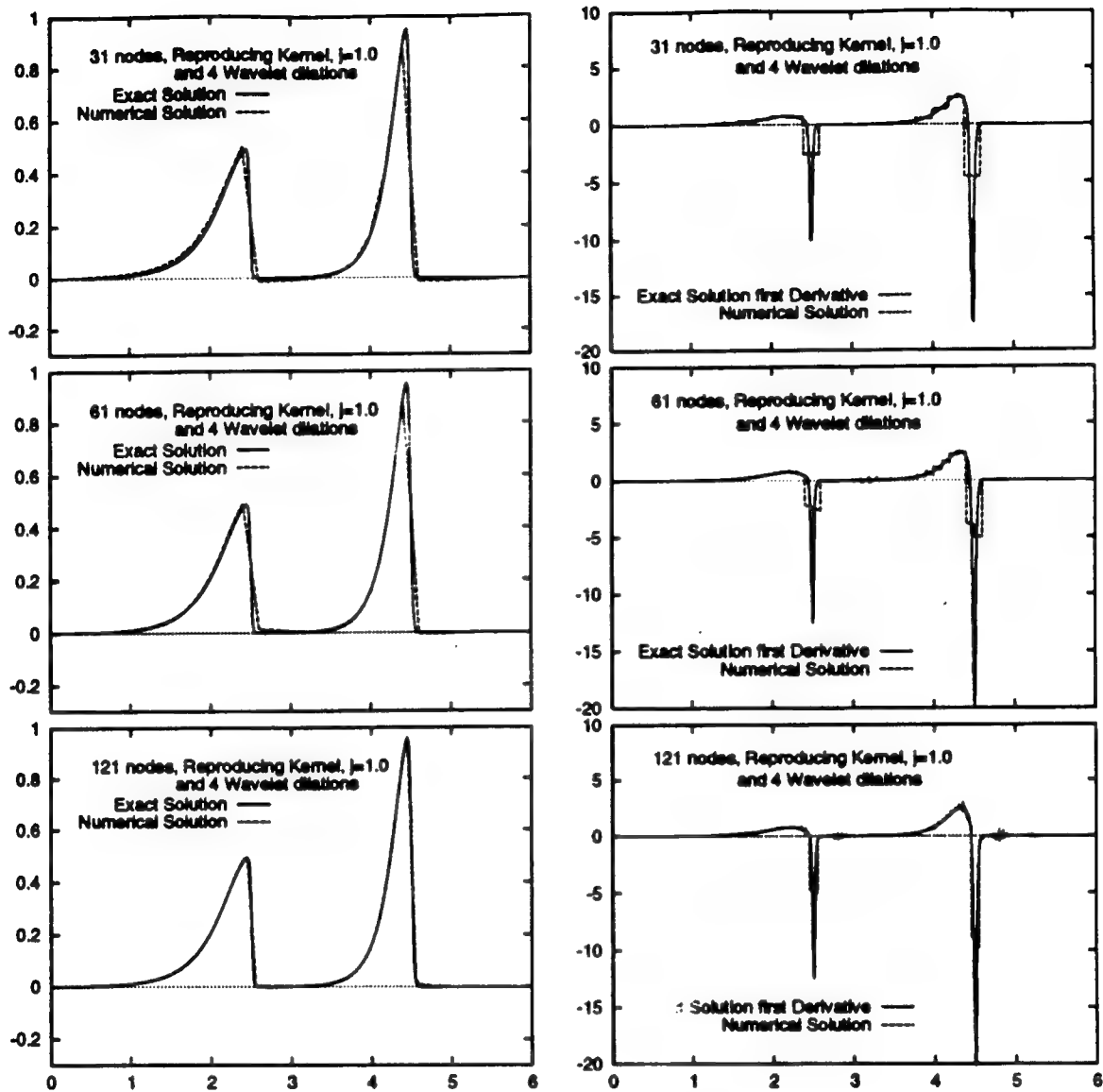


Figure 6.3 Solution of the Diffusion Equation
using four Wavelet dilations

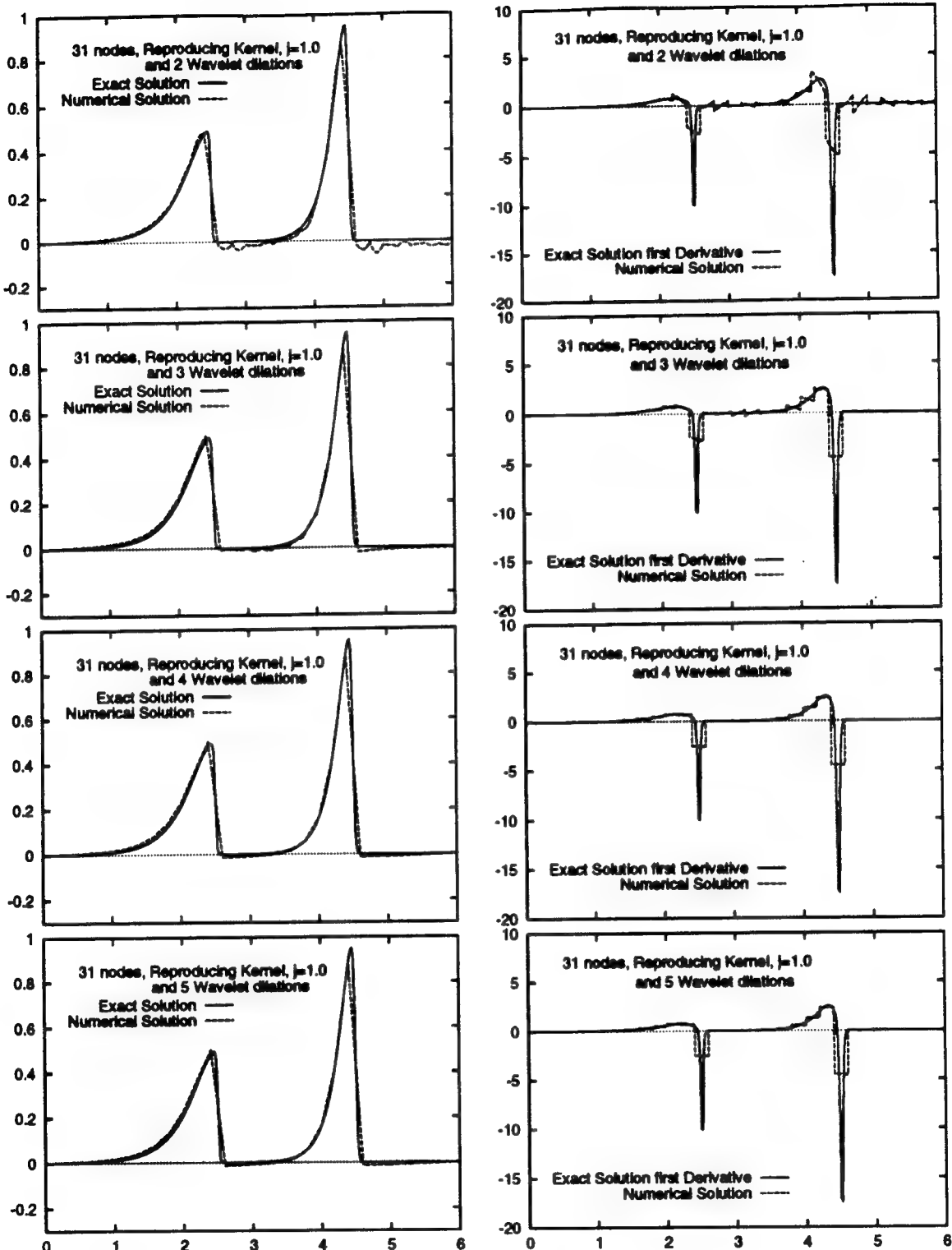


Figure 6.4 Solution of the Diffusion Equation
using 31 nodes and several number of Wavelet dilations

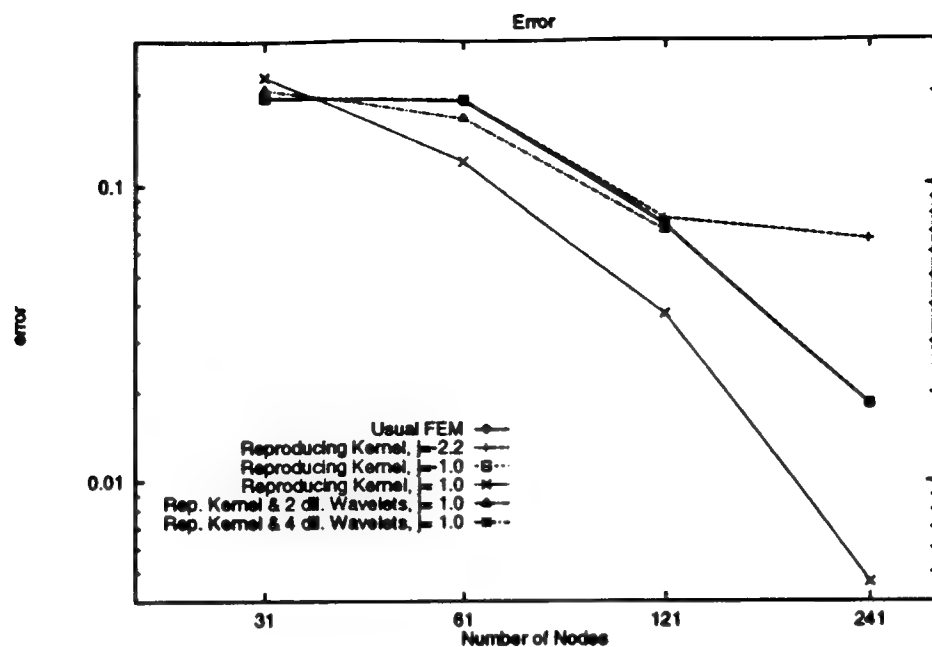


Figure 6.5a Error of numerical solutions for the Diffusion Equation

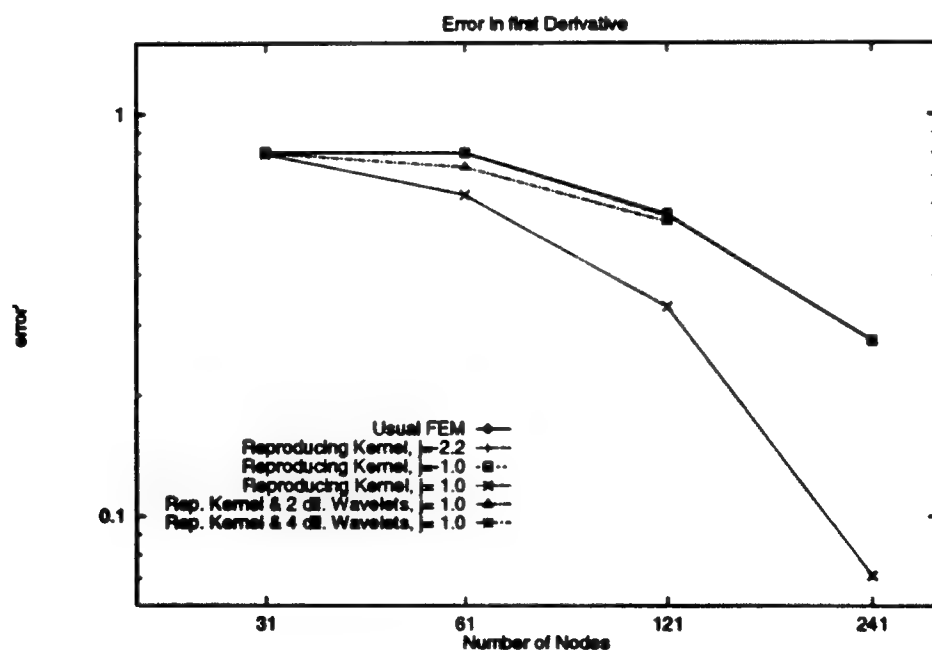


Figure 6.5b Error in the derivative of numerical solutions for the Diffusion Equation

num. of nodes	31	61	121	241
Usual FEM	0.19545	0.18977	0.07468	0.01827
RKPM $j = -2.2$	0.19511	0.18954	0.07829	0.06641
RKPM $j = -1.0$	0.19589	0.19054	0.07507	0.01839
RKPM $j = 1.0$	0.22884	0.11999	0.03746	0.00463
2 WL dil., $j=1.0$	0.20792	0.16593	0.07138	
4 WL dil., $j=1.0$	0.19507	0.19137	0.07507	

Table 6.1a Error of numerical solutions for
the Diffusion Equation

num. of nodes	31	61	121	241
Usual FEM	0.80144	0.79926	0.56435	0.27424
RKPM $j = -2.2$	0.80144	0.79910	0.56383	0.27401
RKPM $j = -1.0$	0.80283	0.80029	0.56555	0.27422
RKPM $j = 1.0$	0.79341	0.63022	0.33317	0.07116
2 WL dil., $j=1.0$	0.79900	0.73682	0.54145	
4 WL dil., $j=1.0$	0.80149	0.79854	0.55935	

Table 6.1b Error in the derivative of numerical solutions for
the Diffusion Equation

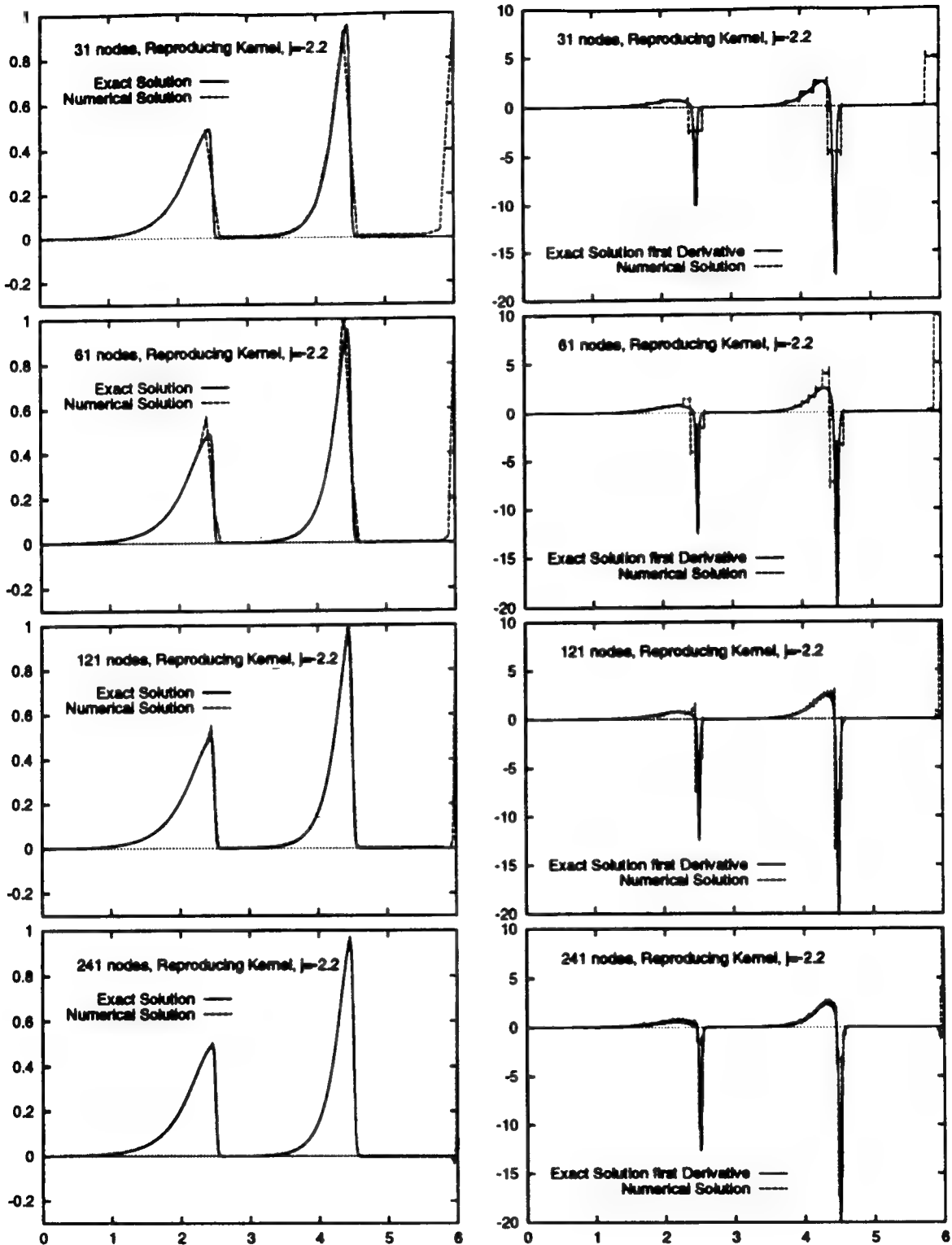


Figure 6.6 Solution of the Advection-Diffusion Equation
using Gaussian Reproducing Kernel with $j = -2.2$

References

Amsden, A. A., and Harlow, F. H., [1970]; "The SMAC Method, A Numerical Technique for Calculating Incompressible Fluid Flow," Tech Report LA-4370, Los Alamos Scientific Laboratory.

Belytschko, T., "An Overview of Semidiscretization and Time Integration Procedures," Computer Methods for Transient Analysis, T. Belytschko and T. J. R. Hughes eds., North-Holland, Amsterdam, 1983, pp. 1-63.

Belytschko, T. and Kennedy, J. M., [1978]; "Computer Models for Subassembly Simulation," *Nuclear Engineering and Design*, **49**, pp. 17-38.

Belytschko, T., Lu, Y. Y. and Gu, L., [1993]; Element Free Galerkin Methods, (*preprint*).

Burton, D. E., and Harrison, A. K., [1991]; "Simulation of Single Mode Richtmyer-Meshkov Instability Using the Adaptive Free Lagrange Method," UCRL-JC-108033, LLNL report.

Chui, C. K., [1992]; *An Introduction to Wavelets*, Academic Press.

Daubechies [1992]; Ten Lectures on Wavelets, CBMS/NSF Series in Applied Mathematics, No. 61, *SIAM Publication*.

Gingold, R. A. and Monaghan, J. J., [1977]; Smoothed Particle Hydrodynamics: Theory and Application to Non-Spherical Stars, *Mon. Not. Roy. Astron. Soc.*, **181**, 375-389.

Gingold, R. A., and Monaghan, J. J., [1982]; "Kernel Estimates as a Basis for General Particle Methods in Hydrodynamics," *J. Comp. Physics*, **46**, pp. 429-453.

Gottlieb, D., and Orszag, S. A., [1977]; Numerical Analysis of Spectral Methods: Theory and Applications, *SIAM*, New York.

Harlow, F. H., Amsden, A. A., and Nix, J. R., [1976]; "Relativistic Fluid Dynamics Calculation with Particle-in-Cell Technique," *J. Comput. Phys.*, **20**.

Harlow, F. H., and Welch, J. E., [1965]; "Numerical Calculation of Time-Dependent Viscous Incompressible Flow of Fluid with Free Surface," *The Physics of Fluids*, **8**, 2182-2189.

Hirt, C. W., et al, [1975]; "SOLA - A Numerical Solution Algorithm for Transient Fluid Flows," Los Alamos Scientific Laboratory report LA-5852.

Hirt, C. W., [1983]; "Flow Analysis for Non-Experts," Engineering Foundation Conference Proceedings, Modeling and Control of Casting and Welding Processes II.

Huerta, A., and Liu, W. K., [1988]; "Viscous Flow with Large Free Surface Motion," *Computer Methods in Applied Mechanics and Engineering*, **69**, 277-324.

Hughes, T. J. R., [1987]; The Finite Element Method, *Prentice-Hall*.

Hughes, T. J. R., and Hulbert, G. M., [1988]; "Space-Time Finite Element Methods for Elastodynamics: Formulations and Error Estimates," *Computer Methods in Applied Mechanics and Engineering*, **66**, 339-363.

Johnson, G. R., Peterson, E. H. and Stryk, R. A., [1993]; Incorporation of An SPH Option into The EPIC Code for A Wide Range of High Velocity Impact Computations, (*preprint*).

Lancaster, P. and Salkauskas, K., [1981]; Surfaces Generated by Moving Least Squares Methods, *Mathematics of Computation*, **37**, 141-158.

Liberky, L. D. and Petschek, A. G., [1990]; Smooth Particle Hydrodynamics With Strength of Materials, *Advances in the Free-Lagrange Method, Lecture Notes in Physics*, 248-257.

Liu, W. K., Zhang, Y. and Ramirez, M. R., [1991]; Multiple Scale Finite Element Methods, *International Journal for Numerical Methods in Engineering*, **32**, 969-990.

Liu, W. K., et al., [1988]; "ALE Petrov-Galerkin Finite Elements for Nonlinear Continua," *Computer Methods in Applied Mechanics and Engineering*, **68**, 259-310.

W.K. Liu, et al., [1991]; "Adaptive ALE Finite Elements with Particular Reference to External Work Rate on Frictional Interface," *Computer Methods in Applied Mechanics and Engineering*, **93**, 189-216.

Lucy, L., [1977]; A Numerical Approach to Testing The Fission Hypothesis, *A. J.*, **82**, 1013-1024.

Monaghan, J. J., [1982]; Why Particle Methods Work, *SIAM J. Sci. Stat. Comput.*, **3**, 422-433.

Monaghan, J. J., [1988]; An Introduction to SPH, *Comp. Phys. Comm.*, **48**, 89-96.

Monaghan, J. J., and Gingold, R. A., [1983]; "Shock Simulation by the Particle Method SPH," *J. Comp. Physics*, **52**, pp.374-389.

Nayroles, B., Touzot, G. and Villon, P., [1992]; Generalizing The Finite Element Method: Diffuse Approximation and Diffuse Elements, *Computational Mechanics*, **10**, 307-318.

Nichols, B. D., and Hirt, C. W., [1971]; "Improved Free Surface Boundary Conditions for Numerical Incompressible Flow Calculations," *J. Comp. Phys.*, **8**.

Shakib, F., and Hughes, T. J. R., [1991]; "A New Finite Element Formulation for Computational Fluid Dynamics: IX. Fourier Analysis of Space-Time Galerkin/Least-Squares Algorithms," *Computer Methods in Applied Mechanics and Engineering*, **87**, 35-58.

Subbiah, S., et al, "Non-isothermal flow of polymers into two-dimensional, thin cavity molds: a numerical grid generation approach," *Int J. Heat Mass Transfer*, **32/3**, 415-434, 1989.

Tezduyar, T. E., Behr, M., and Liou, J., [1992]; "A New Strategy for Finite Element Computations Involving Moving Boundaries and Interfaces - the Deforming-Spatial-Domain/Space Tine Procedure: I. The Concept and the Preliminary Tests," *Computer Methods in Applied Mechanics and Engineering*, **94**, 339-351.

Reproducing Kernel Particle Methods

**Wing Kam Liu¹, Yi Fei Zhang², Ted Belytschko¹,
Sukky Jun², Jonathan Adee², and L. Gu²**

Northwestern University
Department of Mechanical Engineering
2145 Sheridan Road
Evanston Illinois 60208

Submitted to

International Journal of Numerical Methods in Fluids

May, 1993

Revised August, 1993

¹ Professor of Mechanical and Civil Engineering

² Graduate student

Reproducing Kernel Particle Methods

Abstract

A new continuous reproducing kernel interpolation function, which explores the attractive features of the flexible time-frequency or space-wave number localization of a window function, is developed. This method is motivated by the theory of wavelets, and it also has all the desirable attributes of the recently proposed smooth particle hydrodynamics (SPH) methods, moving least square methods (MLSM), diffuse element methods (DEM) and the element free Galerkin methods (EFGM). The proposed method maintains the advantages of the free Lagrange or SPH methods; however, it produces much more accurate results. It is labelled as the reproducing kernel particle method (RKPM). In computer implementation, RKPM is shown to be more efficient than the DEM, and EFGM. Moreover, if the window function is C^∞ , the solution and its derivatives are also C^∞ in the entire domain. Theoretical analysis and numerical experiments reveal the stability conditions and the effect of the dilation parameter on the unusually high convergence rates of the proposed method.

1. Introduction

During the last two decades, considerable effort has been devoted to the development of mesh free or grid free interpolation methods. In most methods, the interpolation functions are usually established by enforcing certain continuity requirements around a set of ordered (equally spaced) points. However, due to deformation, this set of points can become highly disordered and the accuracy deteriorates. In addition, if the interpolation methods, such as finite element and finite difference methods, require a mesh or a grid, the distorted mesh can terminate the calculation due to mesh entanglement problems, among others.

Among the mesh or grid free methods are the Smooth Particle Hydrodynamic (SPH) Methods, which are sometimes called the free Lagrange methods. They depend only on a set of disordered points or particles as developed by Lucy [1977], Gingold and Monaghan [1977], among others. The Diffuse Element Methods (DEM) developed by Nayroles, Touzot and Villon [1992], and the Element Free Galerkin Methods (EFGM) recently proposed by Belytschko, Lu and Gu [1993] are based on the moving least square interpolation functions (MLSM) presented by Lancaster and Salkauskas [1981]. All these methods do not require a finite difference grid nor a finite element mesh. Furthermore, if the kernel functions (used in SPH methods), the weighting functions (used in MLSM, DEM, and EFGM), and their derivatives are continuous, the solution and its derivatives are also continuous. The truly mesh free, the continuous solution, and the continuous derivatives are the key selling points of these methods.

The most attractive feature of SPH methods in a large deformation analysis is the *free Lagrange* concept. Although SPH methods work well if there is no boundary (since the boundary terms are tossed out in the formulation, Libersky and Petschek [1990]) and when the number of unknowns (nodes) is large, SPH methods are not as accurate as the regular finite element methods, Johnson, Peterson and Stryk, [1993]. From our study of the SPH interpolation function via a simple one dimensional (1D) Galerkin formulation (see the numerical examples, Section 7), we found that there is an additional deficiency in the SPH formulation. It is related to the boundary correction term of the reproducing kernel approximation. We shall make an attempt to identify this deficiency and present our view for improving the SPH kernel approximation.

After reviewing the moving least square interpolation functions and the diffuse element methods, Belytschko et al. [1993] pointed out that an assumption made by Nayroles et. al. [1992], the interpolation coefficients are constants, detracts from the accuracy of the method. They showed that by adding more accurate derivatives and enforcing boundary conditions by Lagrange

multipliers, the method could achieve very high rates of convergence. From our experience, EFGM are more accurate than the finite element methods, and hence, the SPH methods especially for a small set of nodes. One main drawback of EFGM is the computational expense, and we found that it is more computationally intensive than the SPH methods.

The objective of this paper is along the same line of development as the SPH, DEM, and EFGM : to develop accurate and efficient mesh free interpolation functions. Since a continuous reproducing kernel can be derived for this proposed method and it is a free Lagrange particle method, we shall label this development as *Reproducing Kernel Particle Methods* (RKPM). This proposed approach is motivated by the theory of wavelets (Chui [1992]) where a function is represented by a combination of the dilation and translation of a single wavelet, which is a window function. In a wavelet analysis, similar to the SPH interpolation kernel, the interpolation coefficients are defined in terms of the integral window transform of the window function and the solution. We shall borrow three key ideas from wavelet analysis: the integral window transform, the dilation and translation of a window function, and the continuous and discrete reproducing kernel approximations. It is noted that the window functions used in this paper are *not* wavelets. Good candidates for the window functions are the scaling functions used to produce wavelets since the scaling functions can be constructed to be orthogonal with respect to its translates.

We shall show the similarities between the smooth particle hydrodynamic methods, the diffuse element methods, the element free Galerkin methods and the reproducing kernel particle methods. We shall also show that SPH and RKPM are indeed developed through a *continuous* reproducing kernel approximation; whereas, DEM and EFGM, like finite elements, are developed through a *discrete* reproducing kernel approximation. As a by product of this development, the concept of the dilation of a window function will be used to explain why the accuracy of the diffuse element methods decreases relative to the element free Galerkin methods.

In the next section, some preliminary concepts of integral window transform and SPH interpolation kernel functions are reviewed. In Section 3, the reproducing kernel particle interpolation functions are derived. In Section 4, the effect of the dilation parameter on the reproducing kernel, time-frequency or space-wave number localization, and the stability condition is discussed. In Section 5, some examples of the reproducing kernel window functions are presented. The similarities among SPH, DEM, EFGM, and RKPM interpolation functions are given in Section 6. Numerical experiments, which confirm the theoretical analysis, are presented in Section 7, followed by a conclusion.

2. Preliminaries

2.1 Dilation and translation of a window function

Let \mathbf{x} denote the spatial coordinates. If $\Phi(\mathbf{x})$ is a window function located at $\mathbf{x} = \mathbf{0}$, which has a support of $B(\mathbf{x})$, then

$$\Phi(\mathbf{x}) \neq 0 \quad \text{in } B(\mathbf{x}) \quad (2.1a)$$

$$\Phi(\mathbf{x}) = 0 \quad \text{outside } B(\mathbf{x}) \quad (2.1b)$$

The dilation and translation of $\Phi(\mathbf{x})$, denoted by $\Phi_{ab}(\mathbf{x})$, is defined as:

$$\Phi_{ab}(\mathbf{x}) = E(a) \Phi\left(\frac{\mathbf{x} - \mathbf{b}}{a}\right) \quad a > 0 \quad (2.2)$$

is a window function, located at $\mathbf{x} = \mathbf{b}$ with a support *scaled* by the dilation parameter a . The function $E(a)$ appearing in Eq. (2.2) scales $\Phi_{ab}(\mathbf{x})$ such that:

$$\int_{R_x} \Phi_{ab}(x) dR_x = \int_{R_x} \Phi(x) dR_x = 1 \quad (2.3)$$

when the support $B(x)$ is within the spatial region of interest, R_x . It is noted that when b is close to the boundary of R_x , ∂R_x , the integral of $\Phi_{ab}(x)$ over R_x will be less than 1. We believe that this is a drawback for the SPH methods, as well as all other reproducing kernel methods, including wavelets, which assume the region is unbounded.

2.2 Integral window transform and SPH interpolation kernel functions

The integral window transform of a real function $u(x)$ with a real window function $\Phi_{ab}(x)$ is defined as:

$$\langle u, \Phi_{ab} \rangle = \int_{R_x} E(a) \Phi\left(\frac{x-b}{a}\right) u(x) dR_x \quad (2.4)$$

As a matter of fact, one of the main concepts of the SPH method is to find a suitable smooth reproducing kernel function $\Phi(x)$ that mimics the Dirac Delta function. Hence, when a is chosen to approach zero and when $b = x$, the reproducing kernel approximation of $u(x)$, denoted by $u^h(x)$, is given by:

$$u^h(x) = \langle u, \Phi_{ax} \rangle = \int_{R_x} E(a) \Phi\left(\frac{y-x}{a}\right) u(y) dR_y \quad (2.5)$$

Discretizing the integral of Eq.(2.5) by NP distinct nodes (points) using a numerical quadrature formula gives:

$$u^h(x) \equiv \sum_{J=1}^{NP} E(a) \Phi\left(\frac{x_J - x}{a}\right) u(x_J) \Delta V_J \quad (2.6a)$$

Equation (2.6a) can be written in a more familiar notation; in terms of generalized global shape functions $N_J(x)$:

$$u^h(x) = \sum_{J=1}^{NP} N_J(x) u_J \quad ; \quad N_J(x) = E(a) \Phi\left(\frac{x_J - x}{a}\right) \Delta V_J \quad \text{no sum on } J \quad (2.6b)$$

where $u_J \equiv u(x_J)$ and $\Delta V_J \neq 0$ is the J^{th} nodal domain (volume in three dimensions (3D), area in 2D, and length in 1D) associated with quadrature points x_J . The sum of all ΔV_J gives the total domain V . That is:

$$\sum_{J=1}^{NP} \Delta V_J = V \quad (2.6c)$$

The SPH methods use a similar interpolation formula as given in Eqs. (2.6). Instead of using ΔV_J and $E(a) \Phi\left(\frac{x_J - x}{a}\right)$, ΔM_J and $\rho_J E(a) \Phi\left(\frac{x_J - x}{a}\right)$ are employed. ΔM_J and ρ_J are the J^{th} particle mass and density, respectively. With this substitution in Eq.(2.6a) or (2.6b), the SPH approximation can be used in standard interpolation Galerkin, collocation, or spectral methods, but the particle methods use information from a set of disordered points based on kernel estimation, Monaghan [1982]. It is also pointed out by Monaghan [1988], SPH works quite well for arbitrarily moving fluid if the number of particles is *large* and in the absence of boundaries; however, there is not a systematic way to handle moving fluid with rigid or moving boundaries in

SPH. Furthermore, it is not clear how to generalize SPH to non-uniform mass particles or the effect of the dilation parameter "a" on the accuracy of the solution.

2.3 Moments

We shall define the following moments for the window function $\Phi(x)$.

$$m_0(x) = \int_{B(x)} \rho \Phi(y) dR_y \quad \text{zero moment} \quad (2.7a)$$

$$m_i(x) = \int_{B(x)} \rho y_i \Phi(y) dR_y \quad \text{first moment} \quad (2.7b)$$

$$m_{ij}(x) = \int_{B(x)} \rho y_i y_j \Phi(y) dR_y \quad \begin{array}{l} i \neq j \text{ cross moment} \\ i = j \text{ second moment} \end{array} \quad (2.7c)$$

In the above equations, the integral is evaluated with respect to the support $B(x)$. Hence, if $B(x)$ is close to the boundary of the spatial region R_X , $m_0(x)$ is less than one. The subscripted indices i and j take values from 1 to NSD, where NSD is the number of space dimensions. If $\Phi(y)$ is symmetric, $m_i(x) = 0$ in the interior of R_X and $m_i(x) \neq 0$ when x is close to the boundary. $m_{ii}(x)$ (no sum on i) denotes the second moment of $\Phi(x)$ in the x_i direction; and $m_{ij}(x)$, $i \neq j$, denotes the cross moment. Definitions for higher order moments can be defined in a similar fashion. We shall employ these moments to analyze the reproducing kernel particle interpolation functions which is described next.

3. Reproducing Kernel Particle Interpolation Functions

The objective is to use the concept of reproducing kernels and the local character of the window function to develop an accurate reproducing kernel function from a suitable smooth window function $\Phi_{ab}(x)$ multiplied by a correction function $C(a, x, b)$. If both $\Phi_{ab}(x)$ and $C(a, x, b)$ are smooth functions within the spatial region R_x , that is, the functions and its derivatives are continuous, then we have developed global interpolation functions that do not require a finite element mesh nor a finite difference grid. In particular, unlike the SPH methods, the dilation parameter a can take a fairly large range of positive values provided certain stability conditions are met.

Our goal then is to develop reproducing kernel particle interpolation functions which will have the following merits.

1) If $\Phi_{ab}(x)$ is an even function, the correction function $C(a, x, b)$ should be one when the support of $\Phi_{ab}(x)$ is not close to the boundary, ∂R_x ; it differs from one when $\Phi_{ab}(x)$ is close to the boundary.

2) A truly element or mesh free particle method similar to SPH methods with much better accuracy, especially when the number of particles is *small*.

3) Similar to MLSM, DEM, and EFGM, RKPM provides smoother approximations of the solution as well as its derivatives; however, RKPM is computationally more efficient and a mathematical analysis of the RKPM is also available.

Consider a function $u(x)$ represented in terms of m linearly independent functions $P_i(x)$ such that:

$$u(x) = \sum_{i=1}^m P_i(x) c_i \quad (3.1a)$$

or in matrix notation:

$$u(x) = P(x) c \quad (3.1b)$$

where $P(x) = \{P_1(x), P_2(x), \dots, P_m(x)\}$, a vector of m linear independent functions, and $c = \{c_1, c_2, \dots, c_m\}^T$ are the unknown coefficients. A superposed "T" denotes the transpose. In order to define c in terms of the solution locally around any point x , we multiply both sides of Eq.(3.1b) by $\rho(y) P^T(y)$ and perform the integral window transform with respect to a positive even window function $\Phi_{ax}(y)$ to yield (Note: x has been replaced by y in Eq.(3.1b)):

$$\langle \rho P^T u, \Phi_{ax} \rangle = \langle \rho P^T P, \Phi_{ax} \rangle c \quad (3.2a)$$

or the vector of coefficients c is solved in terms of the solution u :

$$c = M^{-1}(x) \langle \rho P^T u, \Phi_{ax} \rangle \quad (3.2b)$$

where the $m \times m$ non-singular matrix $M(x)$ is denoted by:

$$M(x) = \langle \rho P^T P, \Phi_{ax} \rangle = \int_{R_x} \rho(y) P^T(y) P(y) E(a) \Phi\left(\frac{y-x}{a}\right) dR_y \quad (3.3)$$

It is noted that $M(x)$ is a continuous function of the translation (x) of the window function $\Phi_{ax}(y)$. Substitute Eq.(3.2b) into Eq.(3.1b) gives the approximation of $u(x)$, denoted by $u^h(x)$ through a continuous reproducing kernel:

$$u^h(x) = \langle \rho P(x) M^{-1}(x) P^T u, \Phi_{ax} \rangle \quad (3.4)$$

Using the definition of the integral window transform, $u^h(x)$ can be shown to be:

$$u^h(x) = \int_{R_x} k(a, x, y) u(y) dR_y \quad (3.5)$$

where the reproducing kernel, which is a modified window function, is :

$$k(a, x, y) = k_{ax}(y) = C(a, x, y) E(a) \Phi\left(\frac{y - x}{a}\right) \quad (3.6a)$$

and the function $C(a, x, y)$ is given by:

$$C(a, x, y) = \rho(y) \{ P(x) M^{-1}(x) P^T(y) \} \quad (3.6b)$$

To write Eq.(3.5) in a discrete reproducing kernel particle form, the integral of Eq.(3.5) is discretized by NP distinct points using a numerical quadrature formula to yield the usual approximation formula:

$$u^h(x) = \sum_{j=1}^{NP} N_j(x) u_j \quad (3.7a)$$

and the reproducing kernel particle interpolation functions are given by:

$$N_J(x) = C(a, x, x_J) E(a) \Phi\left(\frac{x_J - x}{a}\right) \Delta V_J \quad (3.7b)$$

Comparing Eq.(3.7b) with the SPH interpolation formula, Eq.(2.6b), we believe that the discretized correction function

$$C(a, x, x_J) = \rho(x_J) \left\{ P(x) M^{-1}(x) P^T(x_J) \right\} \quad (3.7c)$$

will improve the accuracy of the interpolation kernel tremendously, partly due to boundary corrections. Depending on the choice of $P(x)$, we shall show that the correction function is composed of the moments defined in the previous session. In particular, if $P(x)$ is chosen to be constant and linear polynomials:

$$P(x) = \{1, x_1, x_2, x_3\} \quad (3.8a)$$

it is shown that the continuous function $C(a, x, y)$ takes the following form:

$$C(a, x, y) = C_1(a, x) + C_2(a, x) \cdot \left(\frac{x - y}{a} \right) \quad (3.8b)$$

In Eq.(3.8b), C_1 and C_2 are continuous scalar and vector functions of the zeroth, first and cross moments. A dot denotes the inner product. It will also be shown that $C_1(a, x) = 1$ and $C_2(a, x) = 0$ when the support of $\Phi_{ax}(y)$, $B(x)$, is not close to the boundary of the domain; whereas $C_1(a, x) \neq 1$ and $C_2(a, x) \neq 0$ when the window function moves close to the boundary of the domain. It is noted that $M(x)$ needs to be computed only once, even in a large deformation *free Lagrangian* or *Eulerian* analyses. In the latter case, the density ρ is chosen equal to one.

Remark : It can be seen that if $u(x) = P(x)$, then:

$$\begin{aligned}
 P(x) &= \int_{R_x} \rho(y) P(x) M^{-1}(x) P^T(y) E(a) \Phi\left(\frac{y-x}{a}\right) P(y) dR_y \\
 &= P(x) M^{-1}(x) \int_{R_x} \rho(y) P^T(y) P(y) E(a) \Phi\left(\frac{y-x}{a}\right) dR_y \\
 &= P(x)
 \end{aligned} \tag{3.9}$$

because of the definition of $M(x)$. Therefore if $P(x)$ is chosen to be $\{1, x_1, x_2, x_3, x_1^2, \dots\}$, the reproducing kernel will satisfy the usual isoparametric finite element properties. In a discrete approximation, we have:

$$\sum_{j=1}^{NP} N_j(x) = 1 \quad ; \quad \sum_{j=1}^{NP} N_j(x) x_j = x \quad ; \quad \text{etc.} \tag{3.10}$$

4. Effect of the Dilation Parameter on the Reproducing Kernel and Stability Condition

In this section, we restrict our discussion to one dimension. To explore the accuracy of the RKPM interpolation functions, we shall relate the dilation parameter a (sometimes called a scale) to the frequency content (in time); or the wave number/wavelength content (in space). For simplicity, we let x be the time axis and ω is the frequency axis. A similar interpretation can be made when x and ω are the space and the wave number, respectively.

4.1 Frequency band

by:

Following Chui [1992], we define the center x^* and radius $\Delta\phi$ of a window function $\Phi(x)$

$$x^* = \frac{1}{\|\Phi\|_2^2} \int_{-\infty}^{\infty} x |\Phi(x)|^2 dx \quad (4.1a)$$

$$\Delta\phi = \frac{1}{\|\Phi\|_2} \left\{ \int_{-\infty}^{\infty} (x-x^*)^2 |\Phi(x)|^2 dx \right\}^{1/2} \quad (4.1b)$$

The width of the window function $\Phi(x)$ is defined by $2\Delta\phi$. The norm of $\Phi(x)$ is defined as:

$$\|\Phi\|_2 = (\Phi, \Phi)^{1/2} \quad (4.2a)$$

For our choice of the scaling parameter, the norm of $\Phi_{ab}(x)$ is related to $\Phi(x)$ by:

$$\|\Phi_{ab}\|_2^2 = a^{-1} \|\Phi\|_2^2 \quad (4.2b)$$

Suppose that $\Phi(x)$ is any function such that both $\Phi(x)$ and its Fourier transform $\hat{\Phi}(\omega)$ are window functions. Following the definitions Eqs.(4.1), the center frequency ω^* , and the radius of $\Delta\hat{\Phi}$ of $\hat{\Phi}(\omega)$ are given by:

$$\omega^* = \frac{1}{\|\hat{\Phi}\|_2^2} \int_{-\infty}^{\infty} \omega |\hat{\Phi}(\omega)|^2 d\omega \quad (4.3a)$$

$$\hat{\Delta\Phi} = \frac{1}{\|\hat{\Phi}\|_2} \left\{ \int_{-\infty}^{\infty} (\omega - \omega^*)^2 |\hat{\Phi}(\omega)|^2 d\omega \right\}^{1/2} \quad (4.3b)$$

4.2 Time-frequency band of the parent reproducing kernel function

The center and radius in Section 4.1 are defined over an unbounded domain so that x^* and $\Delta\Phi$ are invariant with respect to the translation (x). Since the kernel function is a function of y and it is defined within R_x only, we redefine a parent kernel function as:

$$k(y) = C(y) a^{-1} \Phi(y) \quad (4.4)$$

where $C(y)$ is equivalent to $C(a, x, y)$ of Eq.(3.6b) and the arguments a and x are dropped here because they are implicit parameters and only y is a variable. Let us denote the center and radius of $k(y)$ as \bar{x} and $\Delta\bar{k}$, respectively.

$$\bar{x} = \frac{1}{\|k\|_2^2} \int_{R_x} y |C(y) a^{-1} \Phi(y)|^2 dy \quad (4.5a)$$

$$\Delta\bar{k} = \frac{1}{\|k\|_2} \left\{ \int_{R_x} (y - \bar{x})^2 |C(y) a^{-1} \Phi(y)|^2 dy \right\}^{1/2} \quad (4.5b)$$

If the Fourier transform of $k(y)$ is denoted by $\hat{k}(\omega)$, the center ($\hat{\omega}$) and the radius ($\Delta\hat{k}$) of $\hat{k}(\omega)$ in the frequency space are given by:

$$\hat{\omega} = \frac{1}{\|\hat{k}\|_2^2} \int_{-\infty}^{\infty} \omega |\hat{k}(\omega)|^2 d\omega \quad (4.6a)$$

$$\Delta \hat{k} = \frac{1}{\|\hat{k}\|_2} \left\{ \int_{-\infty}^{\infty} (\omega - \hat{\omega})^2 |\hat{k}(\omega)|^2 d\omega \right\} \quad (4.6b)$$

From the parent kernel function $k(y)$, the two-parameter reproducing kernel function $k_{ax}(y) = k(a, x, y)$ can be generated by translation (x) and dilation (a):

$$k_{ax}(y) = C\left(\frac{y-x}{a}\right) a^{-1} \Phi\left(\frac{y-x}{a}\right). \quad (4.7)$$

The relationship between the norms of $k(y)$ and $k_{ax}(y)$ are obtained by:

$$\|k_{ax}\|_2 = \left\{ \int_{R_x} \left| C\left(\frac{y-x}{a}\right) a^{-1} \Phi\left(\frac{y-x}{a}\right) \right|^2 dy \right\}^{1/2} \quad (4.8a)$$

$$= a^{1/2} \left\{ \int_{R_x} \left| C(z) a^{-1} \Phi(z) \right|^2 dz \right\}^{1/2} \quad (4.8b)$$

$$= a^{1/2} \|k\|_2 \quad (4.8c)$$

4.3 Time-frequency or space-wave number localization

Because of the linear translation of the reproducing kernel $k_{ax}(y)$, the integral window transform of the response u with $k_{ax}(y)$:

$$\langle u, k_{ax} \rangle = \int_{R_x} C\left(\frac{y-x}{a}\right) a^{-1} \Phi\left(\frac{y-x}{a}\right) u(y) dy \quad (4.9a)$$

localizes the response with a *time window* or a *space window*:

$$[x + a\bar{x} - a\Delta\bar{k} ; x + a\bar{x} + a\Delta\bar{k}] \quad (4.9b)$$

Furthermore, since the domain is bounded, x^* and Δk have been replaced by \bar{x} and $\Delta\bar{k}$ such that:

$$\bar{x} = x^* = \text{constant} ; \Delta\bar{k} = \Delta k = \text{constant} \quad \text{if } B(x) \text{ in } R_x \quad (4.9c)$$

$$\bar{x} = x^* = \text{variable} ; \Delta\bar{k} = \Delta k = \text{variable} \quad \text{if } B(x) \text{ is close to } R_x \quad (4.9d)$$

In Eq.(4.9d), x^* and Δk have to be computed according to Eqs.(4.5). The center and radius of the reproducing kernel function $k_{ax}(y)$ are shown to be:

$$\begin{aligned} \text{center} &= \frac{1}{\|k_{ax}\|_2^2} \int_{R_x} y \left| C\left(\frac{y-x}{a}\right) a^{-1} \Phi\left(\frac{y-x}{a}\right) \right|^2 dy \\ &= \frac{1}{\|k\|_2^2} \int_{R_x} (x + az) \left| C(z) a^{-1} \Phi(z) \right|^2 dz = x + a\bar{x} \end{aligned} \quad (4.10a)$$

$$\begin{aligned} \text{radius} &= \frac{1}{\|k_{ax}\|_2} \left\{ \int_{R_x} [y - (x + a\bar{x})]^2 \left| C\left(\frac{y-x}{a}\right) a^{-1} \Phi\left(\frac{y-x}{a}\right) \right|^2 dy \right\}^{1/2} \\ &= \frac{a}{\|k\|_2} \left\{ \int_{R_x} (z - \bar{x})^2 \left| C(z) a^{-1} \Phi(z) \right|^2 dz \right\}^{1/2} = a\Delta\bar{k} \end{aligned} \quad (4.10b)$$

The window width is defined as $2a\Delta k$. Therefore, the integral reproducing kernel window transform can be interpreted as a *time* or *space-localization* of the response (Chui [1992]). Hence, the integral window transform Eq.(4.9a) gives local information of u with the time or space window in Eq.(4.9b).

Since the Fourier transform of the reproducing kernel $k_{ax}(y)$ denoted by $\hat{k}_{ax}(\omega)$ is also a window function, $\hat{k}_{ax}(\omega)$ is given by:

$$\begin{aligned}\hat{k}_{ax}(\omega) &= \int_{R_x} e^{-i\omega y} \left\{ C\left(\frac{y-x}{a}\right) a^{-1} \Phi\left(\frac{y-x}{a}\right) \right\} dy \\ &= a e^{-i\omega x} \int_{R_x} e^{-i(a\omega)z} \left\{ C(z) a^{-1} \Phi(z) \right\} dz = a e^{-i\omega x} \hat{k}(a\omega) \quad (4.11)\end{aligned}$$

To study u in the frequency domain, we shall employ the Parseval identity (Daubechies[1992]) in which the inner product of any two continuous functions is related to the inner product of the Fourier transform, denoted by \hat{u} and \hat{g} through:

$$\langle u, g \rangle = \frac{1}{2\pi} \langle \hat{u}, \hat{g} \rangle \quad (4.12)$$

Therefore, if we let $g(y) = k_{ax}(y)$, the integral reproducing kernel transform Eq.(3.5) becomes

$$u^h(x) = \langle u, k_{ax} \rangle = \frac{a}{2\pi} \int_{-\infty}^{\infty} \hat{u}(\omega) e^{i\omega x} \hat{k}(a\omega) d\omega \quad (4.13)$$

Equation (4.13) reveals that the integral reproducing kernel window transform also gives local information of $\hat{u}(\omega)$ with a *frequency-window*

$$\left[\frac{\hat{\omega}}{a} - \frac{\Delta\hat{k}}{a} ; \frac{\hat{\omega}}{a} + \frac{\Delta\hat{k}}{a} \right] \quad (4.14)$$

and a bandwidth equal to $2\Delta\hat{k}/a$. It is noted that the ratio of the center frequency and the bandwidth is equal to $\hat{\omega}/(2\Delta\hat{k})$, which is independent of the scaling parameter when the support of the window function is within the domain R_x . We wish to construct $C(y) = C(a, x, y)$ so that the ratio is fairly constant when x is closed to the boundary. Employing the definition of the center frequency, Eq.(4.6a), and the linear transform $\omega' = a\omega$, the center frequency of $\hat{k}(a\omega)$ is shown to be:

$$\begin{aligned} \text{center} &= \frac{1}{\|\hat{k}(a\omega)\|_2^2} \int_{-\infty}^{\infty} \omega |\hat{k}(a\omega)|^2 d\omega \\ &= \frac{1}{a} \frac{1}{\|\hat{k}(\omega')\|_2^2} \int_{-\infty}^{\infty} \omega' |\hat{k}(\omega')|^2 d\omega' = \frac{\hat{\omega}}{a} \end{aligned} \quad (4.15a)$$

Similarly, using Eq.(4.6b), and the linear transformation $\omega' = a\omega$, the radius of $\hat{k}(a\omega)$ can be shown to be:

$$\begin{aligned} \text{radius} &= \frac{1}{\|\hat{k}(a\omega)\|_2} \left\{ \int_{-\infty}^{\infty} \left(\omega - \frac{\hat{\omega}}{a} \right)^2 |\hat{k}(a\omega)|^2 d\omega \right\}^{1/2} \\ &= \frac{1}{a} \frac{1}{\|\hat{k}(\omega')\|_2} \left\{ \int_{-\infty}^{\infty} \left(\omega' - \hat{\omega} \right)^2 |\hat{k}(\omega')|^2 d\omega' \right\}^{1/2} = \frac{\Delta\hat{k}}{a} \end{aligned} \quad (4.15b)$$

where

$$\| \hat{k}(a\omega) \|_2 = a^{-1/2} \| \hat{k}(\omega') \|_2 \quad (4.15c)$$

is the relationship between the norms.

From the above analysis, it is interesting to point out that the integral reproducing kernel window transform in the time or space domain [Eq.(3.5)] and in the frequency or wave number domain [Eq.(4.13)], study the response u in a rectangular *time-frequency* or *space-wave number* window given by:

$$[x + a\bar{x} - a\Delta\bar{k}; x + a\bar{x} + a\Delta\bar{k}] \times [\frac{\hat{\omega}}{a} - \frac{\Delta\hat{k}}{a}; \frac{\hat{\omega}}{a} + \frac{\Delta\hat{k}}{a}] \quad (4.16)$$

The above window narrows to pick up the high-frequency or high wave-number phenomena of u and widens to study the low-frequency or low wave-number response. This suggests that we employ a flexible time-frequency or space wave-number reproducing kernel window to define adaptive refinement of the local response of u around any point x .

4.4 Stability analysis

If $\Phi(y)$ is symmetric, $\hat{\omega}$ is zero. Therefore, the frequency window is always located at $\omega = 0$, and its frequency band becomes:

$$[-\frac{\Delta\hat{k}}{a}; \frac{\Delta\hat{k}}{a}] \quad (4.17)$$

The smaller the a , the larger the frequency band; the larger the a , the smaller the frequency band. This implies that the number of sampling point within $B(x)$ must satisfy the relation:

$$\Delta x \leq \text{CON} \times \pi / \left(\frac{\Delta \hat{k}}{2a} \right) = \text{CON} \times 2\pi a / \Delta \hat{k} \quad (4.18)$$

to avoid aliasing (Brigham [1974]). Δx is called the sampling rate. The constant, CON, will depend on the so-called frame bounds (Daubechies [1992]):

$$A \leq \frac{2\pi}{\Delta x} |\hat{k}(a \omega)|^2 \leq B \quad (4.19)$$

The positive frame bounds coefficients A and B can be estimated numerically. If A/B is close to one, CON will be close to one. Equation (4.18) is referred to as the stability condition of the reproducing kernel window function methods. In practice, CON is chosen much less than one (Liu, Zhang and Ramirez [1991]).

It is well known that even if the sampling rate satisfies Eqs. (4.18) and (4.19), there is not a good choice for a high frequency band window function that can provide accurate frequency and time resolutions of u simultaneously. Therefore, for a small a , an intelligent selection of the frequency band is necessary to be effective. One possible way to employ a larger sampling rate in high frequency or high wave number analysis is the multiple-scale method proposed by Liu, Zhang and Ramirez [1991]. In this approach, the response is divided into multiple frequency bands via a shifting theorem. If $\Phi_{ab}(x)$ is a wavelet, then the center frequency $\hat{\omega} > 0$. By breaking u up into different scales, we shall have a multi-resolution analysis (Chui [1992]).

In this paper, we restrict ourselves to the analysis of a single frequency band, where $\Phi_{ab}(x)$ is chosen to be the scaling function so that $\hat{\omega} = 0$. Consequently, depending on the choice of a and the scaling function, $\Phi(x)$, the integral reproducing kernel window transform, $\langle u, k_{ax} \rangle$, is

a measure of the amount of change of u at the location $x + a\bar{x}$ with the zoom-in (smaller a) and zoom-out (larger a) capability.

4.5 Limitation of very low frequency/wave number analysis

The disadvantage of a single band reproducing kernel analysis is that the method will break down for very low frequency/wave number analysis, such as for large dilation parameter a . This can be seen by interpreting the reproducing kernel Eq.(3.5) as a continuous-time or space convolution:

$$u^h(x) = \int_{R_x} \{C(a, x, y) a^{-1} \Phi\left(\frac{y-x}{a}\right)\} u(y) dy \quad (4.20a)$$

and the reproducing kernel is identified as:

$$k(a, y) = C(a, y) a^{-1} \Phi\left(\frac{y}{a}\right) \quad (4.20b)$$

Applying the Fourier transform to both sides of Eq.(4.20a) and employing the Fubini theorem (Daubechies [1992]) to the right hand side yields:

$$\hat{u}^h(\omega) = \hat{k}(a, \omega) \hat{u}(\omega) \quad (4.21)$$

In order for $\hat{u}^h(\omega)$ to approach $\hat{u}(\omega)$, $\hat{k}(a, \omega)$ must be constructed such that $\hat{k}(a, \omega) = 1$ for all ω ; however, this will violate the Riemann-Lebesgue Lemma that $\hat{k}(a, \omega) = 0$ when ω approaches $\pm\infty$.

An approximation of the convolution identity constructs $\hat{k}(a, \omega)$ so that $\hat{k}(a, \omega) \approx 1$ as a approaches to zero. It is well known that the family of Gaussian functions:

$$a^{-1}\Phi\left(\frac{x}{a}\right) = \frac{1}{a\sqrt{\pi}} e^{-x^2/a^2}, \quad a > 0 \quad (4.22)$$

will satisfy the above conditions provided $C(a, x)$ is constructed so that it is equal to one when Φ_{ax} is in the interior of the domain and is fairly constant when Φ_{ax} moves close to the boundary. With this construction:

$$k(a, x) \equiv a^{-1}\Phi\left(\frac{x}{a}\right) = \frac{1}{a\sqrt{\pi}} e^{-x^2/a^2} \quad (4.23a)$$

and the Fourier transform of $k(a, x)$ is:

$$\hat{k}(a, \omega) = e^{-a^2\omega^2/4} \quad (4.23b)$$

With the Gaussian function, it is noted that a is identified as the standard deviation, and $\hat{k}(a, \omega)$ approaches one as a approaches zero. However, when a is large Eq.(4.19) will break down since $\hat{k}(a, \omega) \neq 1$ unless the frequency content of $u(x)$ is close to zero, which is very restrictive.

From the above argument, the dilation parameter should be chosen within a banded range, say $a_{\min} \leq a \leq a_{\max}$. The maximum a_{\max} will be chosen so that Eq.(4.23b) is close to one. The minimum a_{\min} can be a small number provided the stability condition Eq.(4.18) is met. From our numerical experiments, we found that a can take a large value. We believe that the correction function $C(a, x, y)$ indeed improves the stability as well as the accuracy of the interpolation function. Furthermore, due to the presence of $C(a, x, y)$ which contains the $(x - y)$ term, the reproducing kernel particle interpolation function as given in Eq.(3.7b) will further increase the

order of the *shape function* by one so that the convergence rate will also be increased by one when a is large! This will be discussed further in the next section.

We shall employ the Gaussian function and the cubic spline, which is a good approximation to the Gaussian function, as the window function $\Phi_{ax}(y)$ in the subsequent development. It is further noted that both Gaussian and cubic spline functions are scaling functions used to generate the “Mexican hat” wavelet.

5. Examples of Reproducing Kernel Window Functions

We let the independent functions be:

$$\mathbf{P}(\mathbf{x}) = \{1, x\} \quad 1D \quad (5.1a)$$

$$\mathbf{P}(\mathbf{x}) = \{1, x_1, x_2\} \quad 2D \quad (5.1b)$$

$$\mathbf{P}(\mathbf{x}) = \{1, x_1, x_2, x_3\} \quad 3D \quad (5.1c)$$

By substituting the above vector of independent polynomials into Eqs.(3.3) and (3.6b), the correction function $C(a, x, y)$ can be separated into two terms:

$$C(a, x, y) = C_1(a, x) + C_2(a, x) \cdot \left(\frac{x - y}{a} \right) \quad (5.2)$$

where C_1 and $C_2 = \{C_{21}, \dots, C_{2NSD}\}$ are a scalar and vector, respectively, which can be defined in terms of the zero, first and cross moments. It is noted that all moments are in general a function

of the location of the window function, x , even though they are constants if $B(x)$ is not close to the boundary. The expressions for C_1 and C_2 in 1D, 2D, and 3D are as follows:

One dimension:

$$C_1(a, x) = \frac{m_{11}}{m_0 m_{11} - m_1^2} \quad (5.3a)$$

$$C_2(a, x) = \frac{m_1}{m_0 m_{11} - m_1^2} \quad (5.3b)$$

Two dimensions:

$$C_1(a, x) = \frac{m_{11}m_{22}-m_{12}^2}{m_0(m_{11}m_{22}-m_{12}^2)-(m_1^2m_{22}-2m_1m_2m_{12}+m_2^2m_{11})} \quad (5.4a)$$

$$C_{21}(a, x) = \frac{m_1m_{22}-m_2m_{12}}{m_0(m_{11}m_{22}-m_{12}^2)-(m_1^2m_{22}-2m_1m_2m_{12}+m_2^2m_{11})} \quad (5.4b)$$

$$C_{22}(a, x) = \frac{m_2m_{11}-m_1m_{12}}{m_0(m_{11}m_{22}-m_{12}^2)-(m_1^2m_{22}-2m_1m_2m_{12}+m_2^2m_{11})} \quad (5.4c)$$

Three dimensions:

$$C_1(a, x) = \frac{2m_{12}m_{23}m_{31}+m_{11}m_{22}m_{33}-m_{11}m_{23}^2-m_{22}m_{31}^2-m_{33}m_{12}^2}{D} \quad (5.5a)$$

$$C_{21}(a, x) = \frac{m_1(m_{22}m_{33}-m_{23}^2)+m_2(m_{23}m_{31}-m_{12}m_{33})+m_3(m_{12}m_{23}-m_{31}m_{22})}{D} \quad (5.5b)$$

$$C_{22}(a, x) = \frac{m_2(m_{33}m_{11}-m_{31}^2) + m_3(m_{31}m_{12}-m_{23}m_{11}) + m_1(m_{23}m_{31}-m_{12}m_{33})}{D} \quad (5.5c)$$

$$C_{23}(a, x) = \frac{m_3(m_{11}m_{22}-m_{12}^2) + m_1(m_{12}m_{23}-m_{31}m_{22}) + m_2(m_{31}m_{12}-m_{23}m_{11})}{D} \quad (5.5d)$$

where D , the Jacobian of the $4 \times 4 M(x)$ matrix, is:

$$\begin{aligned} D = & m_0(2m_{12}m_{23}m_{31} + m_{11}m_{22}m_{33} - m_{11}m_{23}^2 - m_{22}m_{31}^2 - m_{33}m_{12}^2) \\ & + m_1(m_{23}^2 - m_{22}m_{33}) + m_2(m_{31}^2 - m_{33}m_{11}) + m_3(m_{12}^2 - m_{11}m_{22}) \\ & + 2m_1m_2(m_{33}m_{12} - m_{23}m_{31}) + 2m_2m_3(m_{11}m_{23} - m_{31}m_{12}) \\ & + 2m_3m_1(m_{22}m_{31} - m_{12}m_{23}) \end{aligned} \quad (5.5e)$$

Because of the special properties of the moments, $C_1(a, x) = 1$ and $C_2(a, x) = 0$ when the window function is within R_x ; whereas $C_1(a, x) \neq 1$, and $C_2(a, x) \neq 0$ when the window function is close to the boundary. It is particularly important to point out that if a is large, the support $B(x)$ is large. Then the linear term appearing in Eq.(5.2), $C_2(a, x) \cdot \left(\frac{x - y}{a}\right)$, plays an important factor in the accuracy and convergence rate of the method.

From Eq.(3.5) and Eq.(3.6), the reproducing kernel function and the approximation $u^h(x)$ are given by:

$$k(a, x, y) = C(a, x, y) E(a) \Phi\left(\frac{y - x}{a}\right) \quad (5.6a)$$

$$u^h(x) = \int_{R_x} k(a, x, y) u(y) dR_y \quad (5.6b)$$

Therefore, if $\Phi(r)$ ($r = ||\mathbf{x} - \mathbf{y}||_2$) is the cubic spline function, the order of polynomials of $\Phi(r)$ is equal to 3. In a Galerkin formulation, the convergence rates of the solution (L2 norm) and its first derivatives (H1 norm) (see numerical examples session for definitions) are expected to be 4 and 3, respectively. However, when a is larger, observing from the discretized Eq.(5.6a) and Eq.(5.2) (with \mathbf{y} replaced by \mathbf{x}_J), the order of the polynomial of the reproducing kernel $k(a, \mathbf{x}, \mathbf{y})$ can be increased by one so that the L2 and H1 convergence rates can be as high as 5 and 4, respectively. This unusual phenomena are observed in our 1D numerical experiments. The convergence rates are much higher when $\Phi(r)$ is replaced by a Gaussian function.

Another interesting observation can also be abstracted from Eq.(5.2). In order to increase the convergence rate by one order, it is suggested to underintegrate the first moments so that it is close to zero, and the term $\mathbf{C}_2(a, \mathbf{x}) \cdot \left(\frac{\mathbf{x} - \mathbf{y}}{a}\right)$ can act as a stabilization term to the SPH methods. At the same time, this stabilization term can also improve the accuracy as well as the convergence rate. One way to achieve this is to use Trapezoidal Rule to integrate the $\mathbf{M}(\mathbf{x})$ matrix (that is, the moments) at each \mathbf{x} .

For higher order polynomials, as well as other independent functions, $\mathbf{P}(\mathbf{x})$ can also be similarly investigated for this class of RKPM interpolation functions; however, from our numerical experiments, we found that using linear polynomials are accurate enough for most purposes. We also found that linear polynomials give numerically more stable calculations than higher order polynomials.

6. Similarities among SPH, DEM, EFGM and RKPM Interpolation Functions

For an illustration of the comparison among the various interpolation funtions, only one dimensional linear polynomials, $\mathbf{P}(\mathbf{x}) = \{1, \mathbf{x}\}$, are implemented. The window function, $\Phi(\mathbf{x})$, is

chosen to be positive definite and an even function. If we use the Trapezoidal Rule to discretize the reproducing kernel Eq.(3.5), the shape function $N_J^R(x)$ of the RKPM is (a>0):

$$N_J^R(x) = \left\{ C_1(x) + C_2(x) \left(\frac{x - x_J}{a} \right) \right\} a^{-1} \Phi \left(\frac{x - x_J}{a} \right) \Delta M_J \quad (6.1a)$$

$$C_1(x) = \frac{m_{11}}{m_0 m_{11} - m_1^2} \quad (6.1b)$$

$$C_2(x) = \frac{m_1}{m_0 m_{11} - m_1^2} \quad (6.1c)$$

where ΔM_J is the J^{th} particle mass. If $m_0 = 1$, $m_{11} \neq 0$, and $m_1 = 0$, the SPH interpolation shape function can be obtained. As a matter of fact, the shape functions of RKPM and SPH are equivalent in an interior, but there is a big difference when they are close to the boundary. Hence, the SPH methods are not accurate when boundaries are present.

Direct differentiation of Eq.(6.1a) gives:

$$N_{J,x}^R(x) = \left\{ C_1'(x) + C_2'(x) \left(\frac{x - x_J}{a} \right) + \frac{C_2(x)}{a} \right\} a^{-1} \Phi \left(\frac{x - x_J}{a} \right) \Delta M_J + \left\{ C_1(x) + C_2(x) \left(\frac{x - x_J}{a} \right) \right\} a^{-2} \Phi' \left(\frac{x - x_J}{a} \right) \Delta M_J \quad (6.2a)$$

$$C_1' = \frac{m_{11}'}{m_0 m_{11} - m_1^2} - \frac{m_{11} (m_0' m_{11} + m_0 m_{11}' - 2m_1 m_1')}{(m_0 m_{11} - m_1^2)^2} \quad (6.2b)$$

$$C_2' = \frac{m_1'}{m_0 m_{11} - m_1^2} - \frac{m_1 (m_0' m_{11} + m_0 m_{11}' - 2m_1 m_1')}{(m_0 m_{11} - m_1^2)^2} \quad (6.2c)$$

In the above expression, a superposed " ' " denotes differentiation with respect to the argument.

Without going into details, the MLSM, DEM and EFGM interpolation functions can be written as (Belytschko et al.[1993]):

$$\bar{N}_j(x) = \sum_{j=1}^2 P_j(x) [A^{-1}(x) B(x)]_{jj} \quad (6.3a)$$

when constant and linear polynomials $P_j(x)$ are employed. The $P(x)$, $A(x)$ and $B(x)$ matrices are defined by:

$$P^T(x) = \{P_1, P_2\} \quad ; \quad P_1(x) = 1 \quad ; \quad P_2(x) = x \quad (6.3b)$$

$$A(x) = \sum_{I=1}^n a^{-1} \Phi\left(\frac{x - x_I}{a}\right) P(x_I) P^T(x_I) \quad (6.3c)$$

$$B(x) = \left\{ a^{-1} \Phi\left(\frac{x - x_1}{a}\right) P(x_1), \dots, a^{-1} \Phi\left(\frac{x - x_n}{a}\right) P(x_n) \right\} \quad (6.3d)$$

where n is the number of points in the neighborhood of x for which the weight function $a^{-1} \Phi\left(\frac{x - x_I}{a}\right) \neq 0$; and x_I are the nodal coordinates of u_I . The derivatives of the EFGM, $\bar{N}_j(x)$, given by Belytschko et al.[1993] are shown as:

$$\bar{N}_{j,x}^E(x) = \sum_{j=1}^2 \{ P_{j,x} [A^{-1}B]_{jj} + P_j [A_{,x}^{-1}B + A^{-1}B_{,x}]_{jj} \} \quad (6.4a)$$

and the derivative of the A^{-1} matrix is given by:

$$\mathbf{A}_{,x}^{-1} = -\mathbf{A}^{-1} \mathbf{A}_{,x} \mathbf{A}^{-1} \quad (6.4b)$$

The derivative of $\bar{N}_J(x)$ of DEM developed by Nayroles et al.[1992] assumes \mathbf{A} and \mathbf{B} constant so that:

$$\bar{N}_{J,x}^D(x) = \sum_{j=1}^2 P_{j,x} [\mathbf{A}^{-1} \mathbf{B}]_{jJ} \quad (6.5)$$

It is noted that no particle mass ΔM_J nor nodal length Δx_J are included in Eqs.(6.3) through (6.5). Furthermore, the \mathbf{A} and \mathbf{B} matrices need to be computed at each quadrature point x .

Although it is not very apparent, an interesting result arises from these three conditions.

1) The nodal coordinates, x_I , are equally spaced.

2) The Trapezoidal Rule is used to numerically integrate $\mathbf{M}(x)$.

3) The integration weights Δx_J , ΔM_J , and ρ_J in Eqs.(6.1a) and (6.2) are all set equal to 1.

\bar{N}_J^R and $\bar{N}_{J,x}^R$, Eq.(6.1a) and Eq.(6.2), can be shown to be equivalent to \bar{N}_J and $\bar{N}_{J,x}^E$, Eq.(6.3a) and Eq.(6.4a), respectively.

With the above assumptions, $\bar{N}_{J,x}^D$ can be similarly defined from the RKPM interpolation functions (with $\Delta M_J = 1$):

$$N_{J,x}^D(x) = -\frac{m_1}{a(m_0m_{11}-m_1^2)} a^{-1} \Phi\left(\frac{x-x_J}{a}\right) \Delta M_J$$

$$-\frac{m_0}{a(m_0m_{11}-m_1^2)} \left(\frac{x-x_J}{a}\right) a^{-1} \Phi\left(\frac{x-x_J}{a}\right) \Delta M_J \quad (6.6)$$

Comparing Eq.(6.2) with Eq.(6.6), depending on $\Phi(x)$, the derivative $\bar{N}_{J,x}^D$ might not be an accurate approximation to $\bar{N}_{J,x}^R$, especially for large a values. For example, let us use the cubic spline functions:

$$\Phi(r) = \frac{2}{3} \cdot \frac{4r^2}{\Delta x^2} + \frac{4r^3}{\Delta x^3} \quad \text{for } 0 \leq \frac{r}{\Delta x} \leq \frac{1}{2} \quad (6.7a)$$

$$\Phi(r) = \frac{4}{3} \cdot \frac{4r}{\Delta x} + \frac{4r^2}{\Delta x^2} - \frac{4r^3}{3\Delta x^3} \quad \text{for } \frac{1}{2} \leq \frac{r}{\Delta x} \leq 1 \quad (6.7b)$$

$$r = || y - x ||_2 \quad (6.7c)$$

as the window function, and the dilation parameter is set such that $a = 2^{j+0.5}$ for $j \geq 0$. The parameter $j = 0$ is adjusted so that Δx is right at the stability limit (see Eq.(4.18) and Eq.(4.19)). This corresponds to the smallest time bandwidth or the largest frequency bandwidth of the window function. Let us consider a set of 21 equally spaced nodes with $\Delta x = 0.3$ representing the domain, $0 \leq x \leq 6.0$. If we use a trapezoidal rule to discretize the domain, then $\Delta x_1 = \Delta x_{21} = 0.15$, and $\Delta x_2 = \Delta x_3 = \dots = \Delta x_{20} = 0.3$. With this discretization and $\rho = 1$, the shape function given in Eq.(6.1a), its derivatives using Eq.(6.2) [exact] and Eq.(6.6) [approximation] are depicted in Figures.1 and 2, respectively for nodes 1, 10, and 21. As might be seen for $j = 0$ (right at the stability limit), the shape functions and its derivatives look similar to those for the usual linear finite elements; however, the derivatives of RKPM shape functions are continuous and they try to

reproduce the finite element discontinuous derivatives. For $j = 1.0$ and $j = 2.0$, there is not much difference between the two derivatives especially for node 10 where the support is within the domain. There is a large difference between the two derivatives when the shape functions are located at the boundaries ($x = 0.0$ and $x = 6.0$). This difference will produce inaccurate derivatives in Eq.(6.6), and the solution deteriorates.

If we pick $\Phi(r)$ as the Gaussian function such that:

$$a^{-1} \Phi\left(\frac{x - y}{a}\right) = \frac{1}{a\sqrt{\pi}} e^{-(x - y)^2/a^2}, \quad a > 0 \quad (6.8a)$$

$$a = 2^{(j+0.5)} \sigma; \quad j \geq 0 \quad \text{and} \quad \frac{\Delta x}{\sigma\sqrt{\pi}} = \frac{1}{\sqrt{2}} \quad (6.8b)$$

With σ as the standard deviation, the *exact* derivative given in Eq.(6.2) and the *approximate* derivative given in Eq.(6.6) become, respectively:

$$N_{j,x}^R(x) = \left\{ C_1'(x) + C_2'(x) \left(\frac{x - x_j}{a} \right) + \frac{C_2(x)}{a} \right\} a^{-1} \Phi\left(\frac{x - x_j}{a}\right) \Delta M_j - \frac{2}{a} \left\{ C_1(x) + C_2(x) \left(\frac{x - x_j}{a} \right) \right\} \left(\frac{x - x_j}{a} \right) a^{-1} \Phi\left(\frac{x - x_j}{a}\right) \Delta M_j \quad (6.9a)$$

$$N_{j,x}^D(x) = - \frac{m_0}{a(m_0 m_{11} - m_1^2)} \left(\frac{x - x_j}{a} \right) a^{-1} \Phi\left(\frac{x - x_j}{a}\right) \Delta M_j - \left\{ \frac{m_1}{a(m_0 m_{11} - m_1^2)} \right\} a^{-1} \Phi\left(\frac{x - x_j}{a}\right) \Delta M_j \quad (6.9b)$$

When the derivatives of the shape function are not evaluated close to the boundaries ($m_1=0$), the two derivatives are represented with the same function $a^{-1}\Phi\left(\frac{x - x_j}{a}\right)$ but different coefficients.

When the derivatives are evaluated close to the boundaries, the two derivatives are again represented by the same Gaussian function, and from numerical experiments, the quadratic term, $\left(\frac{x - x_j}{a}\right)^2$, appearing in Eq.(6.9a) does not play an important role. Therefore, the approximation in Eq.(6.9b) is a good approximation to Eq.(6.9a). This is further elaborated in the next section.

7. Numerical Experiments

We employ a one dimensional Laplacian type equation:

$$u_{,xx} + 2s^2 \operatorname{sech}^2[s(x - 3)] \tanh[s(x - 3)] = 0 \quad (7.1a)$$

with essential boundary conditions:

$$u(0) = -\tanh(3s) \quad (7.1b)$$

$$u(6) = \tanh(3s) \quad (7.1c)$$

The parameter s controls the degree of localization of the gradient of u ($u_{,x}$). As s increases, $u_{,x}$ has an increasing gradient. The exact solution is:

$$u(x) = \tanh[s(x - 3)] \quad (7.1d)$$

In a numerical approximation, we employ a Galerkin formulation of Eq.(7.1a) and the boundary conditions are enforced via the standard Lagrange multiplier approach. For a detail description of this problem and the implementation of the boundary conditions (Belytschko et al. [1993]).

We shall utilize the cubic spline and Gaussian function described in section 6 as window functions. For simplicity, linear polynomials, $P(x) = \{1, x\}$, and $s = 10$ are used throughout. Five different discretizations with $\Delta x = 0.3$ (21 nodes), 0.15 (41 nodes), 0.075 (81 nodes), 0.0375 (161 nodes), and 0.025 (241 nodes) are solved. It is noted that similar to SPH, DEM, and EFGM, RKPM does not require an element nor element connectivities. The standard L2 and H1 error norms are defined as:

$$(L2 \text{ norm})^2 = \int_0^6 (u^{\text{exact}} - u^h)^2 dx \quad (7.2a)$$

$$(H1 \text{ norm})^2 = \int_0^6 (u_{,x}^{\text{exact}} - u_{,x}^h)^2 dx \quad (7.2b)$$

The rates of convergence are defined as the slopes p and q appearing in the $\ln(\text{error})$ vs. $\ln(\Delta x)$ equations:

$$\ln(L2 \text{ norm}) = \ln G_1 + p \ln \Delta x \quad (7.3a)$$

$$\ln(H1 \text{ norm}) = \ln G_2 + q \ln \Delta x \quad (7.3b)$$

The smaller the constants G_1 and G_2 , the more accurate the method. Also, the higher p and q , the faster the rate of convergence. To obtain the convergence plots, ten and twelve Guass quadrature

points are used to integrate the matrices and the errors, respectively. Nevertheless, only three to five Guass quadrature points are sufficient to integrate the matrices accurately. The Trapezoidal Rule is used to integrate all the moments and the $M(x)$ matrices.

The exact solution of $u_{,x}$ and the SPH Galerkin approximation using a Gaussian window, 81 nodes ($\Delta x = 0.075$), $\sigma = \Delta x/(0.1\sqrt{\pi})$, and $\Delta x/(0.5\sqrt{\pi})$ is depicted in Figure 3. It shows the SPH solution depends very much on the dilation parameter (or the standard deviation). As a matter of fact, for a given Δx , the larger the σ (the larger window), the better the gradient is at the center. However, both choices of σ give bad approximations of the gradient of u at the boundaries. This confirms that SPH interpolation functions do not work well with boundaries.

The L2 and H1 norms plots for the spline window function are in Figures 4 and 5, respectively. As can be seen in Figures 4b and 4d, and Figures 5b and 5d, Eq.(6.2) works better than Eq.(6.6) when a is large (i.e., j is large). Similar conclusions can also be drawn from Figures 4a and 4c, and Figures 5a and 5c. One interesting observation is that the L2 and H1 convergence rates (see Figures 4c and 5c) can be as high as 5.7 and 3.9, respectively. This confirms our analysis in Section 6.

Similarly, the L2 and H1 convergence rates plots shown in Figures 6 and 7 are produced using the Gaussian window function. The standard deviation and the dilation parameter are chosen such that:

$$\frac{\Delta x}{\sigma\sqrt{\pi}} = \frac{1}{\sqrt{2}} \quad \text{and} \quad a = 2^{(j+0.5)}\sigma \quad (7.4)$$

As predicted in Section 6, the two formulas for the derivatives give virtually identical results. It is interesting to point out that the L2 and H1 convergence rates can go as high as 15.92, and 14.91,

respectively. Finally, in Table 1, the peak values of $u_{,x}$ are compared with the standard linear finite element method (FEM) and the exact solution. The RKPM is able to capture the high resolution of the steep localized gradient using a flexible space-wave-number Gaussian window function.

8. Conclusions

In this paper, a review of the mesh or grid free interpolation functions is presented. The dilation and translation of a window function, the integral window transform, and the SPH interpolation kernel functions are reviewed. By understanding the merits and deficiency of the SPH, MLSM, DEM, and EFGM methods, a new continuous reproducing kernel particle interpolation kernel function is derived in terms of a flexible time-frequency or a space-wave number localized window function. Comparing to the SPH interpolation function, a continuous correction function to the SPH methods, which is composed of the various moments of the window function, is identified.

The effect of the dilation parameter and the stability condition of this new discretized reproducing kernel particle interpolation function are discussed. The convergence rate of this class of RKPM interpolation functions using a Galerkin method is shown to be at least one order higher than that of the window function when the dilation parameter is large. Since the correction function and the window function can be chosen to be smooth, the solution as well as its derivatives are continuous throughout the entire domain of interest, unlike the usual finite element methods. The numerical experiments confirm the theoretical analysis presented in this paper.

Acknowledgement

The support of this research by AFSOR grant number F49620-92-J-0505 and ONR grant number N00014-93-I-0292 to Northwestern University is gratefully acknowledged.

References

Belytschko, T., Lu, Y. Y. and Gu, L., [1993]; Element Free Galerkin Methods, (*preprint*).

Brigham., E. O., [1974]; *The Fast Fourier Transform*, Prentice-Hall, Englewood Cliffs, N.J.

Chui, C. K., [1992]; *An Introduction to Wavelets*, Academic Press.

Daubechies [1992]; Ten Lectures on Wavelets, CBMS/NSF Series in Applied Mathematics, No. 61, *SIAM Publication*.

Gingold, R. A. and Monaghan, J. J., [1977]; Smoothed Particle Hydrodynamics: Theory and Application to Non-Spherical Stars, *Mon. Not. Roy. Astron. Soc.*, **181**, 375-389.

Johnson, G. R., Peterson, E. H. and Stryk, R. A., [1993]; Incorporation of An SPH Option into The EPIC Code for A Wide Range of High Velocity Impact Computations, (*preprint*).

Lancaster, P. and Salkauskas, K., [1981]; Surfaces Generated by Moving Least Squares Methods, *Mathematics of Computation*, **37**, 141-158.

Liberky, L. D. and Petschek, A. G., [1990]; Smooth Particle Hydrodynamics With Strength of Materials, *Advances in the Free-Lagrange Method, Lecture Notes in Physics*, **395**, 248-257.

Liu, W. K., Zhang, Y. and Ramirez, M. R., [1991]; Multiple Scale Finite Element Methods, *International Journal for Numerical Methods in Engineering*, **32**, 969-990.

Lucy, L. [1977]; A Numerical Approach to Testing The Fission Hypothesis, *A. J.*, **82**, 1013-1024.

Monaghan, J. J. [1982]; Why Particle Methods Work, *SIAM J. Sci. Stat. Comput.*, **3**, 422-433.

Monaghan, J. J. [1988]; An Introduction to SPH, *Comp. Phys. Comm.*, **48**, 89-96.

Nayroles, B., Touzot, G. and Villon, P., [1992]; Generalizing The Finite Element Method: Diffuse Approximation and Diffuse Elements, *Computational Mechanics*, **10**, 307-318.

	Reproducing Kernel Particle Methods (GAUSSIAN)						FEM	EXACT
	j=0.5	j=1.0	j=1.5	j=2.0	j=2.5	j=3.0		
$\Delta x=.300$	3.5100	3.8315	4.6672	5.3217	5.4837	5.1865	3.3168	9.9923
$\Delta x=.15$	6.3599	6.7798	7.6968	8.3095	8.5252	8.5419	6.0343	9.9980
$\Delta x=.075$	8.7556	9.0684	9.6081	9.8416	9.8864	9.9010	8.4687	9.9995
$\Delta x=.0375$	9.6788	9.7992	9.9605	9.9984	9.9995	9.9996	9.5562	9.9998
$\Delta x=.005$	9.8580	9.9155	9.9861	9.9998	9.9999	9.9999	9.7967	9.9999

Table 1. Comparison of derivative peak values among RKPM, FEM, and exact solution.

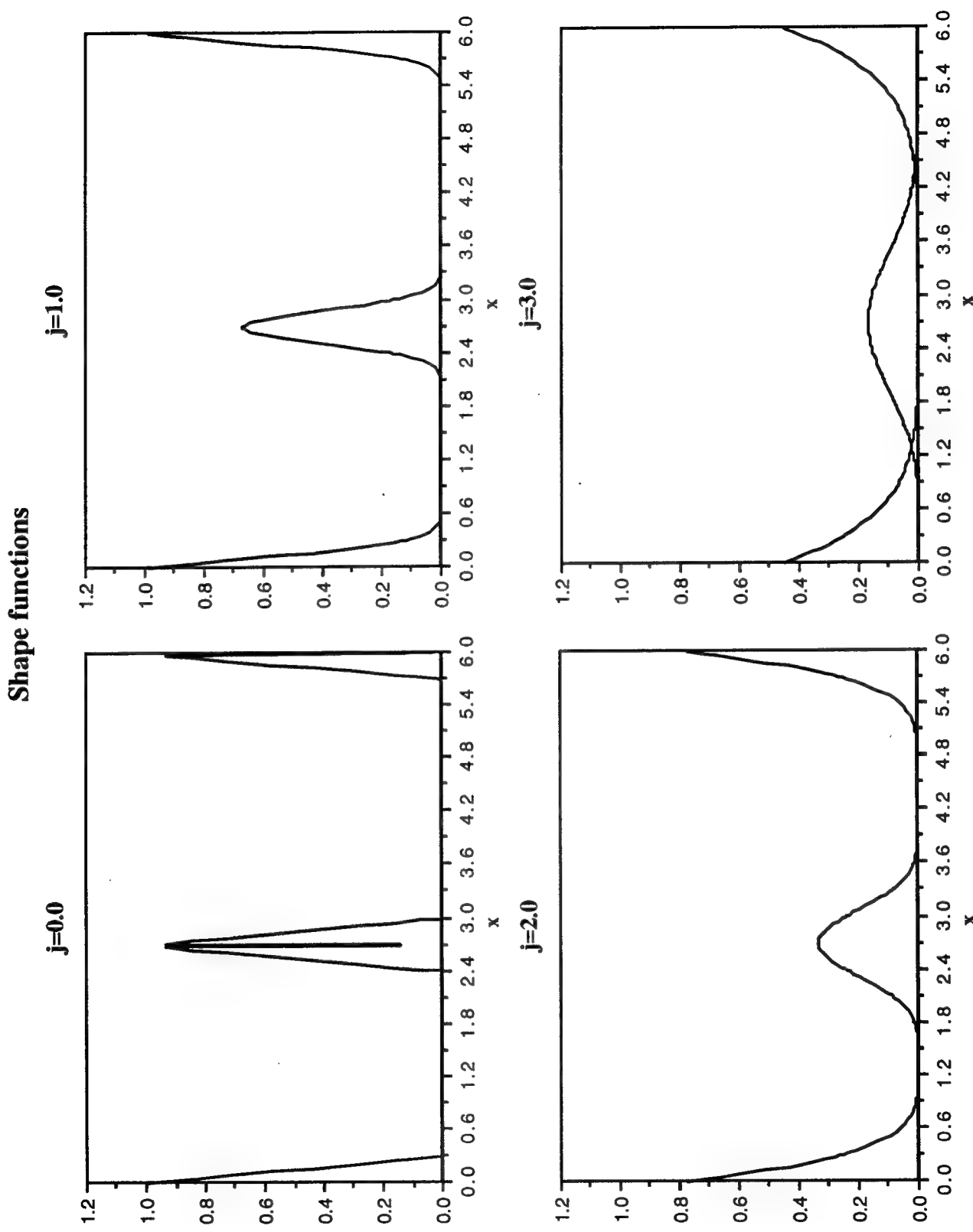


Fig. 1. Plots of interpolation functions at node 1 ($x = 0.0$), node 10 ($x = 2.7$), and node 21 ($x = 6.0$).

Derivatives of shape functions

2

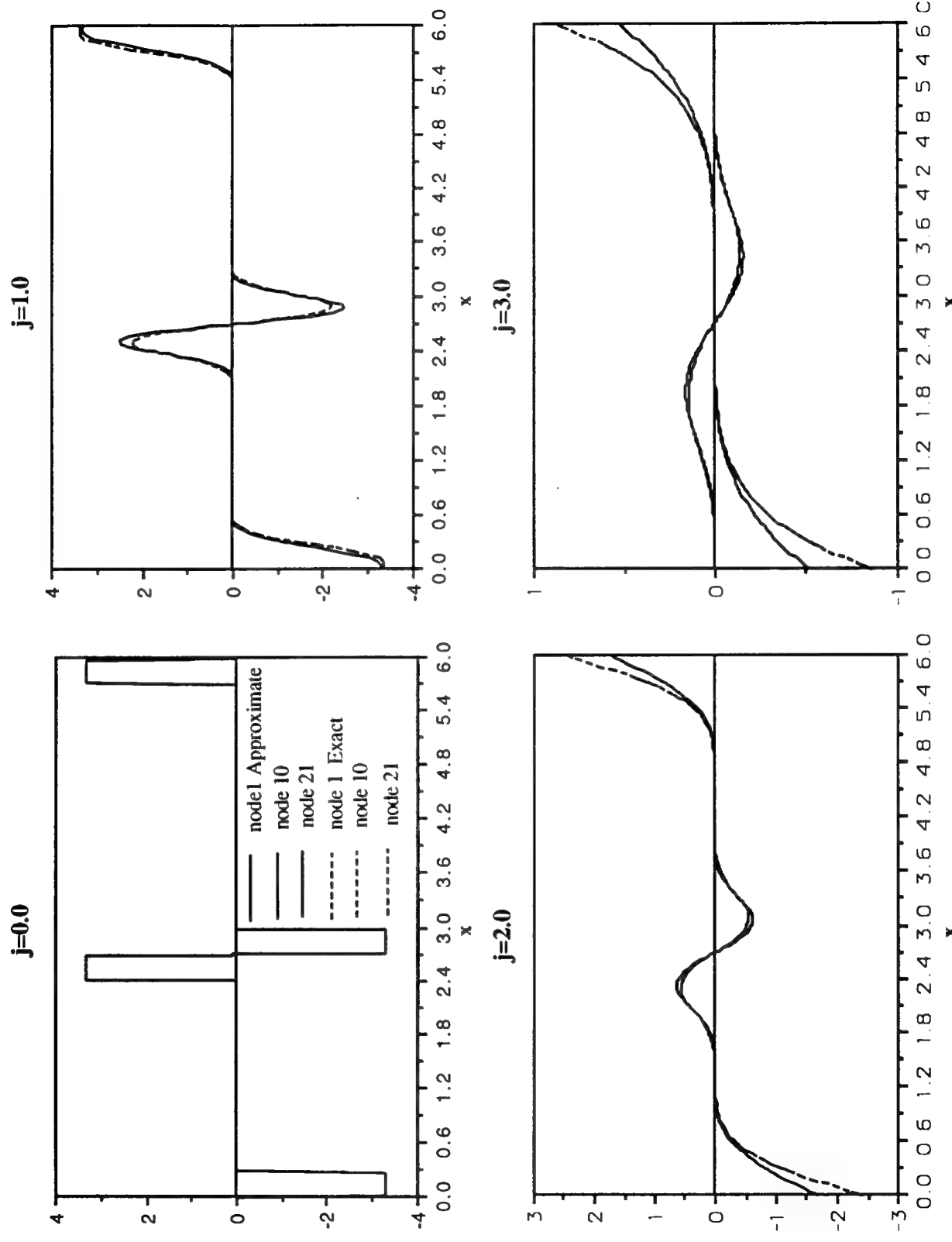


Fig. 2. Derivatives of interpolation functions using exact and approximate formulas at node 1 ($x = 0.0$), node 10 ($x = 2.7$), and node 21 ($x = 6.0$).

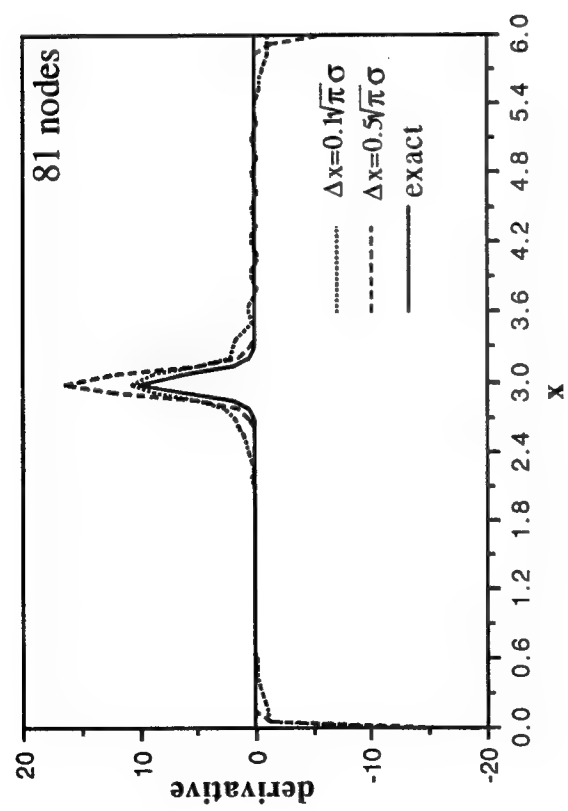


Fig. 3. Comparison of SPH solutions with exact solution.

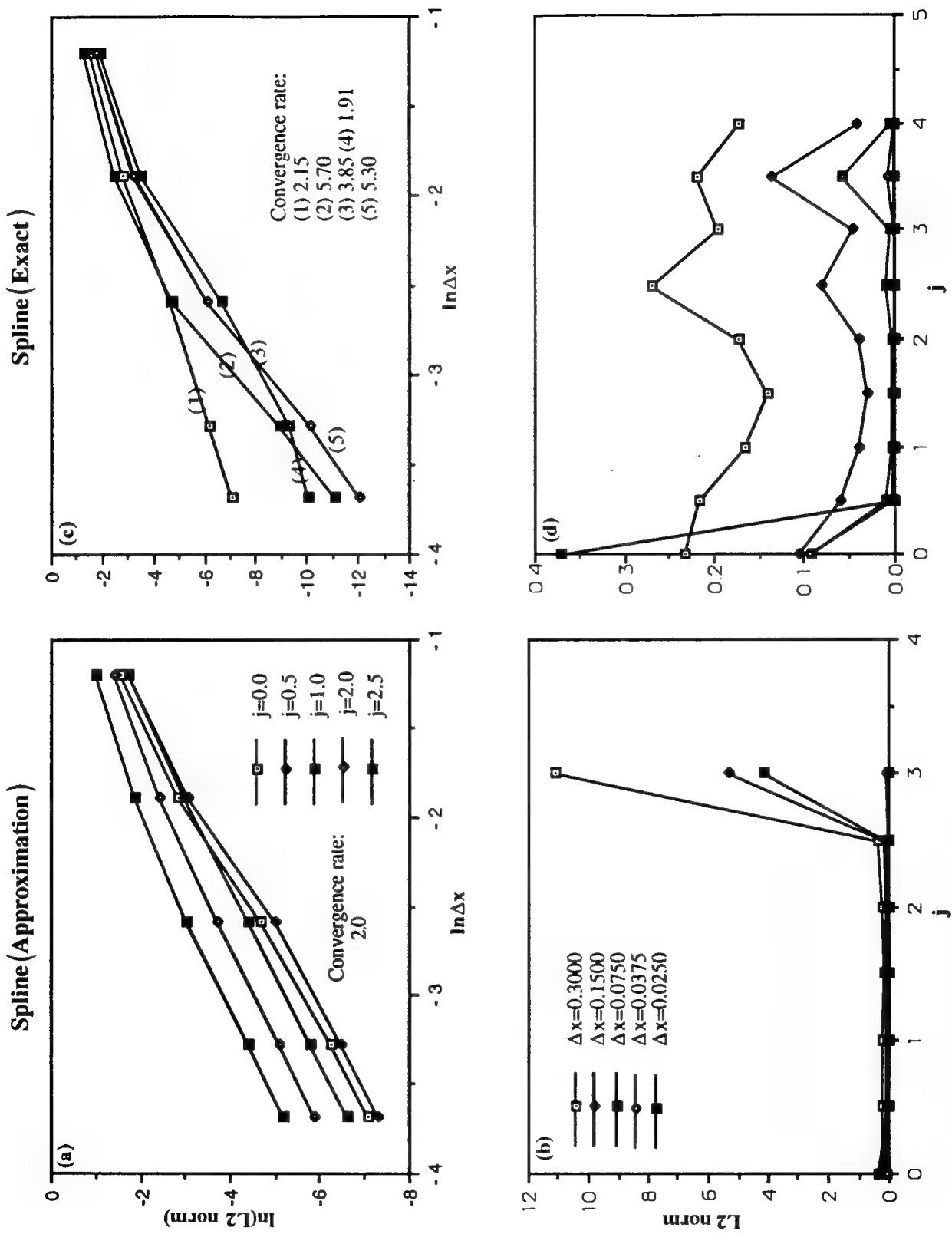


Fig. 4. L_2 norm and convergence plots using approximate and exact formulas for the derivatives of the interpolation function using a (cubic spline) window function.

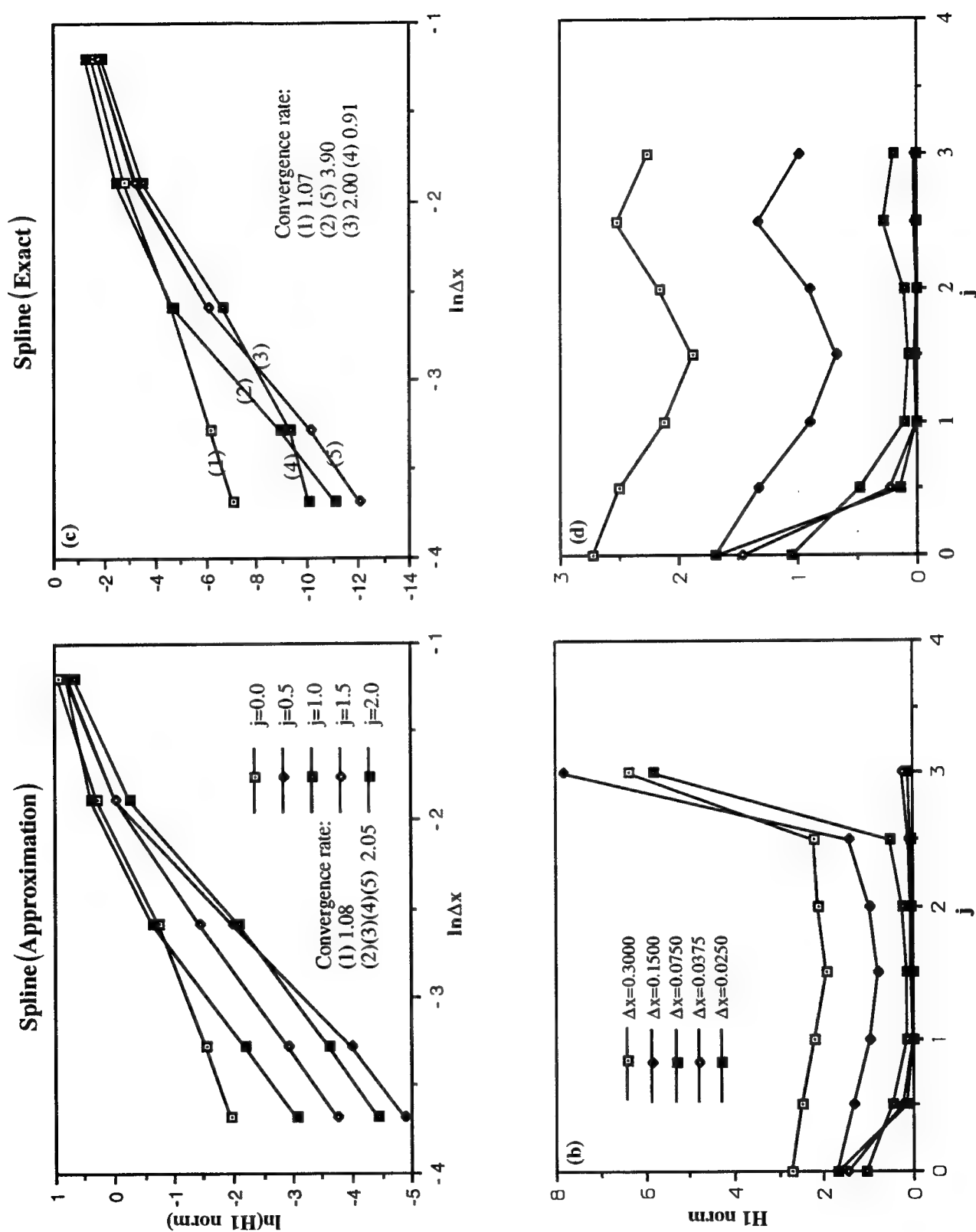


Fig. 5. $H1$ norm and convergence plots using approximate and exact formulas for the derivatives of the interpolation function using a (cubic spline) window function.

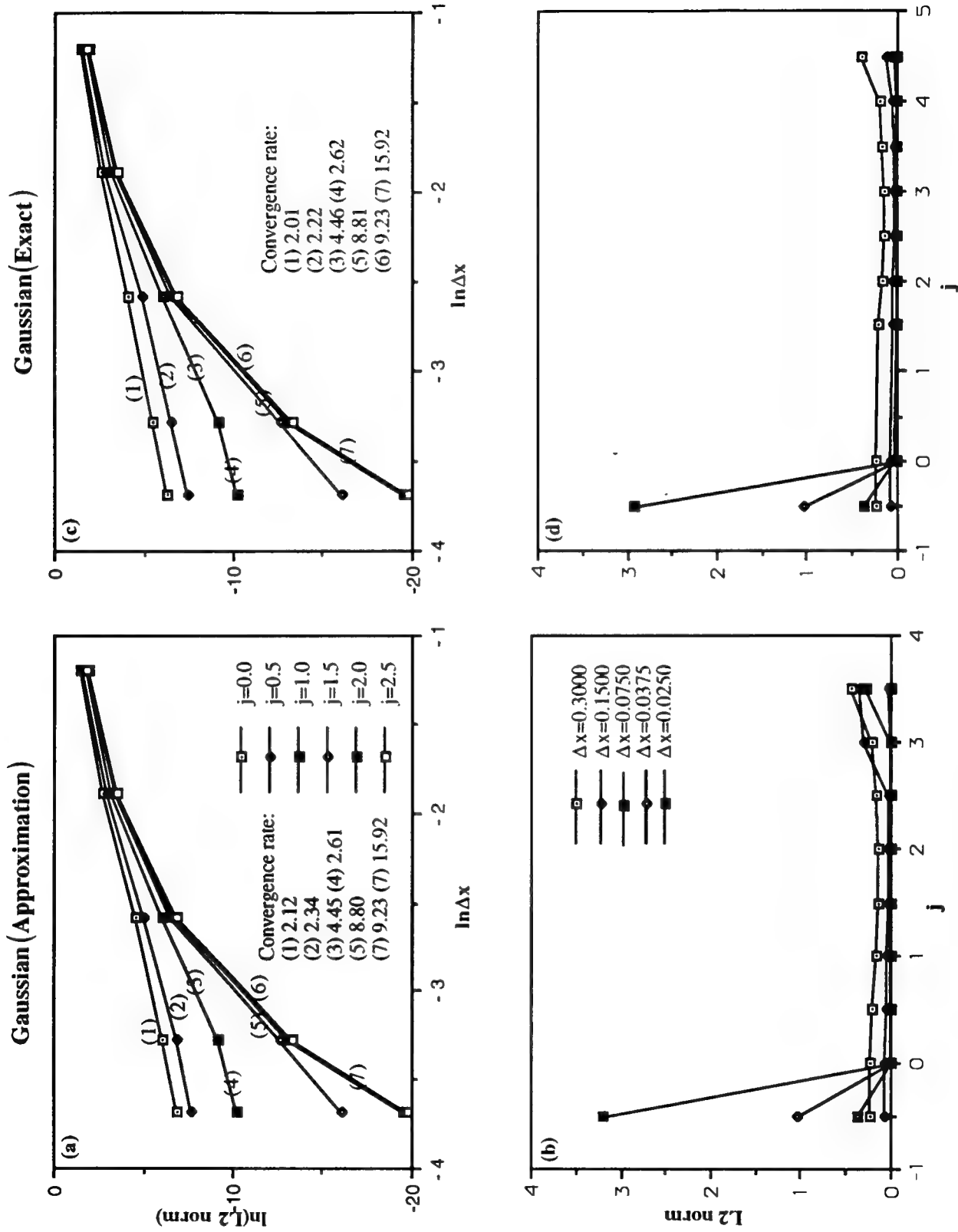


Fig. 6. L_2 norm and convergence plots using approximate and exact formulas for the derivatives of the interpolation function using a (Gaussian) window function.

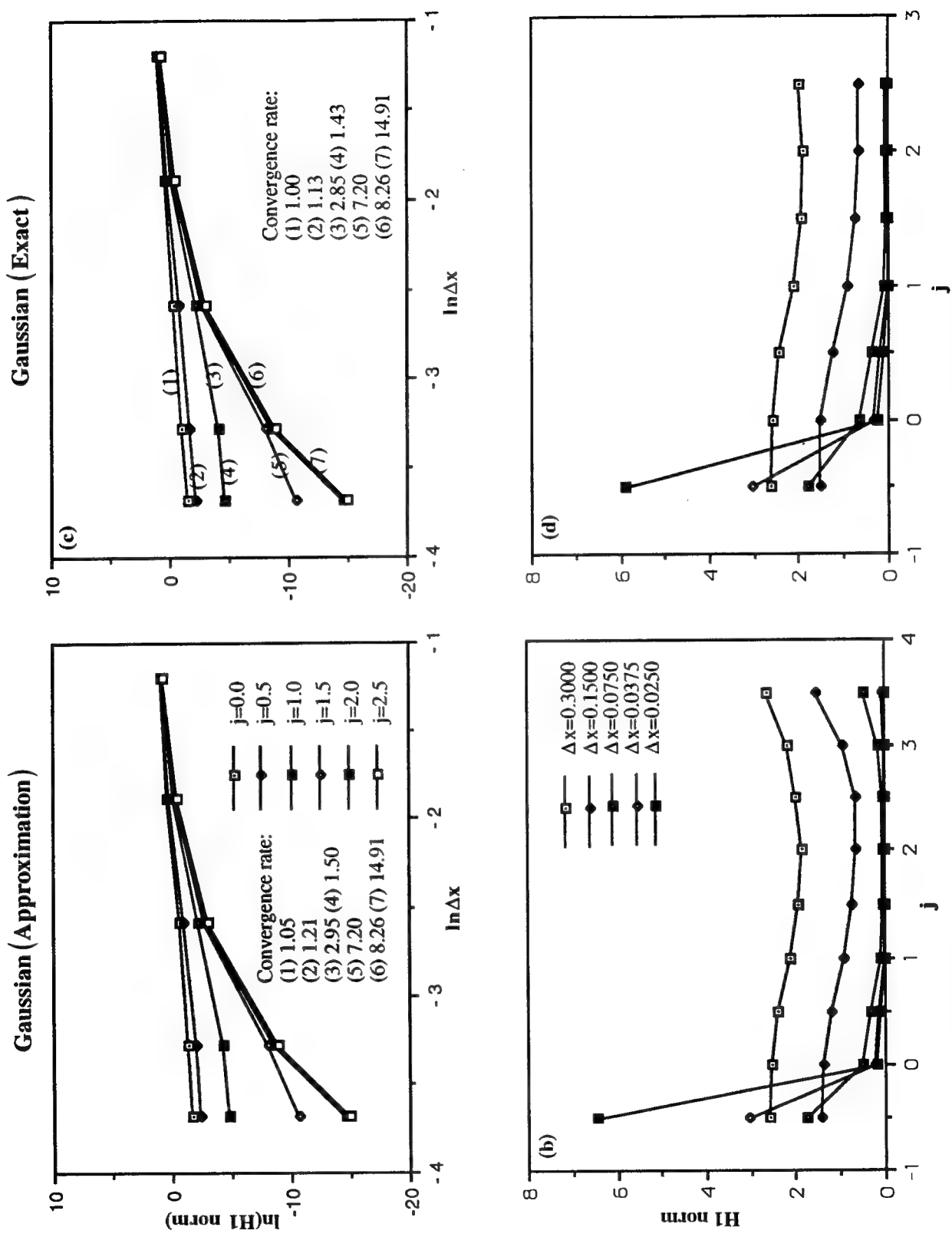


Fig. 7. H_1 norm and convergence plots using approximate and exact formulas for the derivatives of the interpolation function using a (Gaussian) window function.

REPRODUCING KERNEL PARTICLE METHODS FOR ELASTIC AND PLASTIC PROBLEMS

Wing Kam Liu¹, Jonathan Adee², Sukky Jun² and Ted Belytschko¹

**Northwestern University
Department of Mechanical Engineering
2145 Sheridan Road
Evanston, Illinois 60210**

Presented at the 1993 ASME WAM Meeting, New Orleans. Appeared in *Advanced Computational Methods for Material Modeling*, Eds. Benson, D. J. , and Asaro, R. A., AMD 180 and PVP 268, ASME, pp. 175-190, 1993.

Abstract

This analysis explores a Reproducing Kernel Particle Methods which incorporates several inviting features. The emphasis is away from classical mesh generated elements in favor of a mesh free system which only requires a set of nodes or particles in space. Using a Gaussian distribution, flexible window functions are implemented to provide refinement in the solution process. It also creates the ability to analyze a specific frequency range in dynamic problems reducing the computer time required. This advantage is achieved through an increase in the critical time step when the frequency range is low and a large window is used. The stability of the window function is investigated to provide insight on Reproducing Kernel Particle Methods. Furthermore, there are no explicit elements in the formulation, allowing the derivatives to also be continuous, or C^∞ . The analytic theory is confirmed through numerical experiments by performing reconstructions and solving an elastic-dynamic one dimensional problem.

1. Introduction

There is always a drive to find new, more advantageous ways to analyze problems using numerical methods. Typical finite elements use linear or quadratic shape functions to define the response within each element. For large deformation or high frequency problems, the elements must be very small to accurately predict the characteristic response. To avoid these problems, the Reproducing Kernel Particle Method (RKPM) advantages are exploited.

There is no explicit mesh, so mesh creation time is saved. Since a mesh is not required, there are not any problems due to mesh entanglements allowing for large deformations and unrestrained movement of nodes. Not only is mesh creation time saved, but mesh recreation time is eliminated since to refine the problem in an area of interest one needs only to add points in the interesting region. The method for meshless finite elements based on the moving least square interpolant was used by Lancaster and Salkauskas (1981) for graphics, but has been given new life recently by Nayroles et al. (1992) with application to Diffuse Element Methods. This was followed by the Element Free Galerkin Method (EFGM) by Belytschko et al. (1993) that improved upon Nayroles method, including a correction to the derivative of the shape function. There has also been work performed on Smooth Particle Hydrodynamic (SPH) method. The SPH method, developed by Gingold and Monaghan (1977) and others, provides a meshfree environment but it has some difficulty creating accurate solutions on the boundaries or when a small number of particles is used [Monaghan (1988)]. The SPH method is similar in basic construction as the Gaussian Reproducing Kernel (GRK) to be presented here, but it lacks key features of the GRK.

In this Gaussian Reproducing Kernel, the procedure used is based on continuous reproducing kernel particle construction. It can also be viewed as a continuous Least Square polynomial. However, by exploiting the moment definitions of the flexible window function, the reproducing kernel can be reduced to a simplified form so its properties can be investigated. Second, a localized flexible window function is incorporated by translating the function across the entire domain to reproduce the response. The window function, part of the shape function, is controlled by two parameters. Unlike the typical finite elements which only have one, the two parameters allow a greater problem solving ability. The flexible window allows for response frequencies or wave numbers to be selectively reproduced in the numerical approximation. Essential to the development of this method is an understanding of the stability limits of the flexible window function, as well as the critical time step in dynamic analyses. The aforementioned properties of the flexible window function and reproducing kernel create interesting characteristics for the kernel stability. Determining equations are developed for both of these stability limits.

The reproducing kernel in this derivation turns out to be similar to a free Lagrangian particle method [Liberky (1990)] with one major difference--the development of a correction

function. The primary motivation behind the correction function is to provide accurate solutions at the boundaries, but by careful integration techniques it is also possible for the correction function to provide stability to the solution. Free Lagrangian methods provide accurate solutions in the interior of the problem when the number of particles is large, but they do not provide a means to get an accurate solution near the boundary. This method incorporates correction functions that are relatively dormant in the interior and then provide correction on demand at the boundaries.

Through the implementation of a window function and the knowledge of the Fourier transform, it is possible to develop a new type of shape function that can still be used in the usual Galerkin formulation. The derivative of the shape function, and thus reproducing kernel, can be obtained by direct differentiation. The development of the proposed shape function will be derived in detail later, but for now we describe its characteristics. The two parameters in the shape function provide the ability to translate and dilate the window function. Translation is required to move the window function around the domain since the window functions themselves have a compact support. The ability to translate replaces the need to define elements. The dilation parameter is used to provide refinement to the solution by reducing the number of calculations necessary to find a solution. The larger the dilation parameter, the smaller the frequency band is in the solution, and the larger the critical time step becomes in dynamic analyses. The refinement parameter transformation between the time and frequency domain (or space and wave number) controls the solution space. This introduces the ability to choose the size of the frequency or wave number range in the calculation.

2.0 Development of the Reproducing Kernel

Prior examples of reproducing kernels can be found. The most obvious may be its use in the Fourier Transform Analysis. The Fourier Transform motivates this analysis since this is where the concept to analyze specific frequency bands incorporated into this type of reproducing kernel analysis originates.

The general form of a reproducing kernel is a class of functions that output the function itself when the integral over the domain is performed. The Fourier Transform is an excellent example of a reproducing kernel. Its intricacies are defined by the following set of equations

where the Fourier Transform, $\hat{f}(\omega)$ of a function, $f(x)$, is defined by equation (2.0.1) and the inverse Fourier Transform is described by (2.0.2).

$$\hat{f}(x) = \int_{-\infty}^{\infty} e^{-ix\omega} f(x) dx \quad (2.0.1)$$

$$f(x) = \frac{1}{2\pi} \int_{-\infty}^{\infty} e^{ix\omega} \hat{f}(\omega) d\omega \quad (2.0.2)$$

The bounds of the Transform can be easily described if the interesting spectrum contains a single frequency band. The bounds of the Fourier transform, $\hat{f}(\omega)$, are given in equation (2.0.3).

$$\begin{aligned} \hat{f}(\omega) &\neq 0 & \text{if } |\omega| \leq \Omega \\ \hat{f}(\omega) &= 0 & \text{if } |\omega| > \Omega \end{aligned} \quad (2.0.3)$$

It is now possible to show that by performing the inverse transformation on the transformation to obtain the original function, the following solution is obtained where $f(x) \neq 0$ only in the domain $x \in [0, L]$.

$$\begin{aligned}
 f(x) &= \frac{1}{2\pi} \int_{-\Omega}^{\Omega} e^{ix\omega} \left[\int_{-\infty}^{\infty} e^{-iy\omega} f(y) dy \right] d\omega \\
 &= \frac{1}{2\pi} \int_{-\infty}^{\infty} \left[\int_{-\Omega}^{\Omega} e^{i(x-y)\omega} f(y) dy \right] d\omega \\
 &= \int_{-\infty}^{\infty} \frac{\sin[\Omega(x-y)]}{\pi(x-y)} f(y) dy \\
 &= \int_0^L \frac{\sin[\Omega(x-y)]}{\pi(x-y)} f(y) dy = \int_0^L \Phi(x-y) f(y) dy
 \end{aligned} \tag{2.0.4}$$

This representation of a reproducing kernel using a sinc function is presented in Chui (1992) as well as Liu (1991). In Liu's analysis, the multiple scale analysis predicts a critical time step according to the following equation.

$$\frac{\Delta t}{\Delta \omega} \leq \frac{2\pi}{\Omega} \tag{2.0.5}$$

This is used as a guideline since equation (2.0.5) determines the sampling rate to prevent aliasing using the reproducing kernel for a given frequency band, $D\omega$. It is believed that after discretizing the continuous reproducing kernel, a similar form exists for the stability condition of the reproducing kernel in space (see section 4).

2.1 Window Function Selection

The *ideal* window function, $F(x)$, is chosen such that the following two conditions are satisfied. Its integral over the domain, R_x , must be unity, and it must also be orthogonal.

$$1) \quad \int_{R_x} \Phi(x) dR_x = 1 \tag{2.1.1}$$

over the entire domain, rather the value is zero. Furthermore, most wavelets cannot capture constant or linear terms, so they cannot reproduce the simplest of functions very well. For these reasons wavelets are not considered here, but appealing characteristics are used from the wavelet analysis, Chui (1992). Splines are always an option since we can custom tailor them, but they produce unnecessary irregularities. The Gaussian function is not orthogonal, but the Gaussian function is used in this analysis because of its special properties. It is also important to keep in mind that the integration over the entire domain will be less than one on the boundaries.

2.2 Development of Window Function

Like the Fourier series, we want to be able to reconstruct any function or response $u(x)$ by a series of window functions, $F(x)$. Since $F(x)$ is a localized function, it becomes necessary to translate the function to represent the entire response. This is performed by inserting the argument, $s - x$, in the function. Now the response is represented by the following integral.

$$\int_{R_x} C \Phi(s - x) dR_x = 1 \quad (2.2.1)$$

Where C is the correction function to be defined later in the construction, section 2.4. Or it could be an arbitrary constant as in free Lagrangian particle methods, Libersky (1990).

To the window function argument, it is also necessary to add the dilation or refinement parameter, r . This is incorporated by dividing the window function argument by this refinement parameter. For notational purposes this definition is used for the window function:

$$\frac{1}{r} \Phi\left(\frac{s-x}{r}\right) \equiv \Phi_{rx}.$$

$$\int_{R_x} C \Phi_{rx}(x) dR_x = \int_{R_x} C \Phi(x) dR_x = 1 \quad (2.2.2)$$

An intuitive sense of the refinement parameter can be revealed by thinking of the parameter as the *standard deviation*. when the Gaussian distribution is used for the window function. The additional constant, r^{-1} , is the proper constant only for one dimension, Liu (1993). This constant scales the window function such that integral over the domain of the window equals one according to equation (2.2.2). It also is useful to derive the moment equations in section 2.4.1.

$$\int_{R_x} C \frac{1}{r} \Phi\left(\frac{s-x}{r}\right) dR_x = 1 \quad (2.2.3)$$

This completes the development of the window function to be used in this 1-D analysis.

2.3 The Reconstruction Equation

The concept that any function can be represented as a sum of linearly independent functions initiates the analysis, starting with the following definition.

$$u(x) = P(x) d \quad (2.3.1)$$

Where $P(x) = [P_1(x), P_2(x), \dots, P_n(x)]$ which is any number of linearly independent functions

dimensional case, $P(x) = [1, x]$, or for a quadratic one dimensional case, $P(x) = [1, x, x^2]$, etc. This Moving Least Square Interpolant type of reconstruction has been used by Nayroles (1992) and Belytschko et al. (1993), for the Element Free Galerkin Method.

It is possible to solve for the unknown coefficients \mathbf{d} by using the window function. The variable x is changed to s in equation (2.3.1), and then both sides are premultiplied by $r \mathbf{P}^T(s)$ and the integral window transform is applied, Liu (1993) (Note: r is the density and it is included here to make the transition to a large deformation case easier.) The integral window transform multiplies both sides by the window function, Φ_{rs} , and then integrates over the domain.

$$\int_{R_x} \rho \mathbf{P}^T(s) u(s) \Phi_{rs} ds = \int_{R_x} \rho \mathbf{P}^T(s) \mathbf{P}(s) \Phi_{rs} ds \mathbf{d} \quad (2.3.2)$$

$$C(x) = \int_{R_x} \rho \mathbf{P}^T(s) \mathbf{P}(s) \Phi_{rx} ds \quad (2.3.3)$$

Equation (2.3.3) is used in the next section to complete the construction of the correction function. (In that section the merits of C are discussed which shows why the term is sometimes referred to as the boundary correction function.) By making this definition for C , the solution for \mathbf{d} can be substituted back into (2.3.1), obtaining the reconstruction equation in (2.3.5) which can also be written as one integral (2.3.6).

$$\mathbf{d} = C^{-1}(x) \int_{R_x} \rho \mathbf{P}^T(s) u(s) \Phi_{rx} ds \quad (2.3.4)$$

$$u(x) = \mathbf{P}(x) C^{-1}(x) \int_{R_x} \rho \mathbf{P}^T(s) u(s) \Phi_{rx} ds \quad (2.3.5)$$

$$u(x) = \int_{R_x} \rho \mathbf{P}(x) C^{-1}(x) \mathbf{P}^T(s) u(s) \frac{1}{r} \Phi\left(\frac{s-x}{r}\right) ds \quad (2.3.6)$$

2.4 Correction Function

Comparing the reconstruction equation in (2.3.6) to the SPH method establishes that the only difference is the appearance of the $\mathbf{P}(x) C^{-1}(x) \mathbf{P}^T(s)$ term in the GRK method. This term is defined as the correction function, and its merits are analyzed in this section. For simplicity, the characteristics of this function are derived here in one dimension for linear polynomials $\mathbf{P}(x)$, but it can be shown to be valid for multiple dimensions as well, Liu (1993). Expanding equation (2.3.3) reveals the following.

The inverse of this matrix will be computed along with the r , $\mathbf{P}(\mathbf{x})$ and $\mathbf{P}^T(\mathbf{s})$ from the reconstruction formula in equation (2.3.6) to form the correction function. The entire term, $\mathbf{P}(\mathbf{x}) \mathcal{C}^{-1}(\mathbf{x}) \mathbf{P}^T(\mathbf{s})$, function simplifies to one number regardless of the number of terms used for $\mathbf{P}(\mathbf{x})$ and $\mathbf{P}^T(\mathbf{s})$.

2.4.1 Definition of Moments

In order to compute equation (2.4.1) moments are defined in the following manner.

$$m_0 = \int_{B(\mathbf{x})} \rho \Phi(z) dz \quad (2.4.1.1)$$

$$m_1 = \int_{B(\mathbf{x})} \rho z \Phi(z) dz \quad (2.4.1.2)$$

$$m_{11} = \int_{B(\mathbf{x})} \rho z^2 \Phi(z) dz \quad (2.4.1.3)$$

These moment equations are integrated over the region $B(\mathbf{x})$, where $B(\mathbf{x})$ is the region where the window function is non-zero. The calculation could be performed over the entire domain; however, there are many unnecessary calculations involved. In order to determine the support $B(\mathbf{x})$ using the Gaussian function, a three standard deviation criterion can be enforced which insures the calculation of 99.7% of the total area. The moment equations have the following characteristics that provide for an accurate solution near the boundary, and lie relatively dormant in the interior.

	Interior Region	Near Boundaries
m_0	$= 1$	< 1
m_1	$= 0$	$\neq 0$
m_{11}	$= r^2$	$\neq r^2$

Although our initial indication from the correction function was that it vanished in the interior, it is now known that through careful integration of the function and its inverse the function can have a profound effect on the stability of the kernel, see figures 4 and 5. It is noted that the stabilization effect is much more pronounced in the data when the number of nodes is relatively small.

2.4.2 Final Correction Function Form

The solution to $\mathbf{P}(\mathbf{x}) \mathcal{C}^{-1}(\mathbf{x}) \mathbf{P}^T(\mathbf{s})$ can be written in the simplified form shown below through manipulation. Equation (2.4.1) can be inverted and substituted back into the reconstruction in equation (2.3.6) to reveal a continuous reproducing kernel for the function u . This is the final reconstruction equation to be used in this analysis! (Note that the correction term is simplified into the sum of two terms which are defined in the following manner.)

$$C_1 = \frac{m_{11}}{(m_0 m_{11} - m_1^2)} \quad (2.4.2.1)$$

$$C_2 = \frac{m_1}{(m_0 m_{11} - m_1^2)} \quad (2.4.2.2)$$

$$u(x) \equiv \int_{R_x} \left[C_1 + C_2 \left(\frac{x-s}{r} \right) \right] u(s) \frac{1}{r} \Phi \left(\frac{x-s}{r} \right) ds \quad (2.4.2.3)$$

This is the reconstruction equation which is the basic building block of this method, and its intricacies are revealed throughout this investigation. In order to proceed, it is necessary to define the discretized form in order to implement the reconstruction into the numeric solution process later.

$$u^h(x) \equiv \sum_{J=1}^{NP} \left[C_1 + C_2 \left(\frac{x-x_J}{r} \right) \right] \frac{1}{r} \Phi \left(\frac{x-x_J}{r} \right) u(x_J) \Delta M_J \quad (2.4.2.4)$$

The discretized reconstruction equation can be written in a more familiar form to perform the numerical analysis. The shape function is defined as N_J in equation (2.4.2.6).

$$u^h(x) = \sum_{J=1}^{NP} N_J(x) u_J \quad (2.4.2.5)$$

$$N_J(x) = \left[C_1(x) + C_2(x) \left(\frac{x-x_J}{r} \right) \right] r^{-1} \Phi \left(\frac{x-x_J}{r} \right) \Delta M_J \quad (2.4.2.6)$$

By analyzing the properties of the moments, in a continuous case the values for C_1 and C_2 are found to equal 1 and 0 respectively in the interior of a solution (assuming a sufficiently large number of particles), but definitely not equal to these values on the boundary. In this continuous integral case, the GRK will be identical to the SPH in the only in the interior. However, in the discretized form, the effect of the correction function will depend on the integration technique used as well as the number of particles in the integration domain. These variables will determine whether the correction function will only act on the boundaries or enhance the stability of the solution throughout the entire domain.

2.5 Gaussian Reproducing Kernel Formulation

It is important at this point to define the Gaussian function used in this analysis at this time. The refinement parameter is defined to contain a measure of normalization so that a given dilation of the window function always contains the same number of nodes, regardless of particle density. The refinement parameter can also be recognized as the standard deviation in the Gaussian equation.

$$r^{-1} \Phi \left(\frac{x-s}{r} \right) = \frac{1}{r \sqrt{\pi}} e^{-(x-s)^2/r^2} \quad (2.5.1)$$

$$r = 2^j \Delta x \sqrt{\frac{2}{\pi}} \quad (2.5.2)$$

Defining the Gaussian function in this way has the advantage of maintaining the same number of nodes for support while changing the distance between nodes, but the window and shape functions will change while changing nodal coordinates as well as the j refinement. The parameter j can be any real number but stability limits are set in section 5. In prior analyses, the following definition was found to be optimal [Liu (1993)], so it is chosen as a starting point for this analysis.

2.6 Dynamic Frequency Analysis

One of the interesting aspects of this method is its ability to preconceive the frequency range studied in the analysis. The frequency range captured can be determined by calculating the Fourier Transform of the window function. The window function's shape can be changed by the refinement parameter, r , allowing for adaptability in the solution process. Even though the Fourier Transform of the Gaussian function is also bell shaped, a cutoff frequency for the banded window has been found to be $1/r$, Liu (1993). This method matches the area under the Gaussian function with the area of the straight box created by the cutoff frequency. The approximation, $1/r$, for the highest accurately reconstructed frequency inside the window function enables an understanding of the limitations of this method in its straight form.

Unfortunately for this undeveloped implementation of this method, the frequency window is always centered around $w = 0$. This means that we cannot selectively consider only higher frequency bands; it is necessary to capture all the frequencies below the highest frequency of interest. The ability of this method to capture high frequencies is also limited by the stability of the reproducing kernel itself. Although the number of nodes in any one window function is variable, there must be at least two nodes to remain stable. This is necessary in order to have connectivity between window functions. Without the variable connectivity being always greater than two nodes, the response cannot be translated along to the adjacent nodes.

It is hoped that the Multiple Scale Methods by Liu (1991), can be included in subsequent analyses to shift the interested frequency bands away from the origin, removing the unnecessary calculation of the frequencies in between the interesting areas. Another approach is to use wavelets to capture the high frequency bands which is being investigated by Liu, Oberste-Brandenburg, and Chen.

3.0 Given Function Reconstruction

The reproducing kernel is used to perform given function reconstruction, or curve fitting, as a demonstration and evaluation technique before it is implemented into a mesh free Galerkin type formulation. This is done by using the discretized form of the reconstruction equation (2.3.6) to reproduce a known function. The Trapezoidal Rule is used here for integration despite the fact that it is known to under integrate. The dilation parameter has a profound effect on the shape function. Examples of shape functions for several values of the dilation parameter are shown below. Note that for $j = -2$ the window function approaches the ordinary finite element shape function.

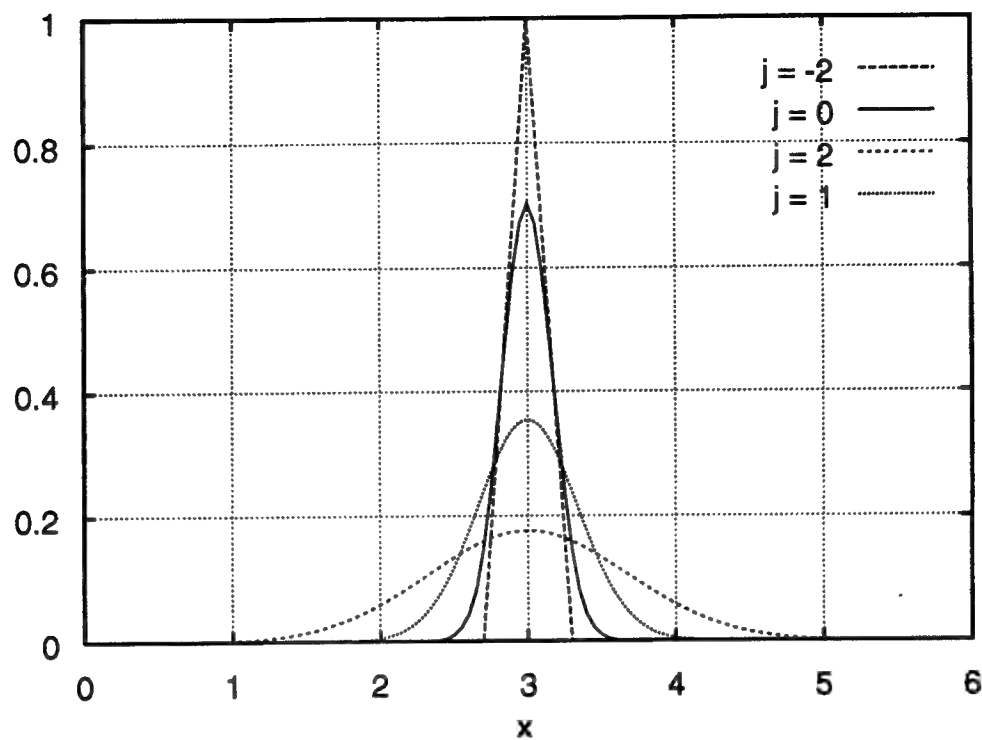


Figure 1 Shape function dilations for $j = -2, 0, 1, 2$

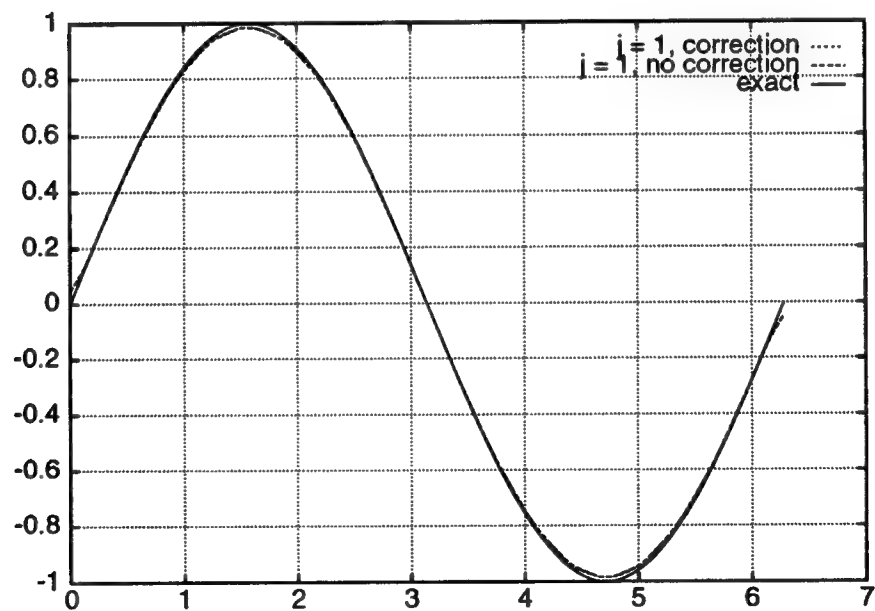


Figure 2 Reconstruction of $\sin(\omega x)$ where $\omega = 1$ with 21 nodes, demonstrating the advantage of the GRK over SPH near the boundaries.

Figure 1 portrays that as the dilation parameter decreases in magnitude, the window function approaches a Dirac delta function. If it was possible to reproduce the Kronecker delta function, all the frequencies would be able to be reproduced. Unfortunately, without additional tools this is not easily possible without large number of particles, due to the stability limit of the window function itself requiring a minimum of two nodes in its support, section 5.1.

This reconstruction develops confidence in the method and helps to illustrate the intricacies. Most notably, it will show the difference between the reproducing kernel method and SPH methods. The big difference is the effect of the correction function, which enables an accurate approximation throughout the entire domain of the response as well as an increased range of stable operation, especially for a small number of particles. The accuracy of the correction function can be analyzed using a simple reconstruction of a known function.

It is readily seen in figure 2 that the SPH solution is not even able to reproduce a simple sinusoidal wave near the boundaries.

In order to relate a feel for the performance of the dilation parameter, figures 3 and 4 depict a sinusoidal reconstruction with and without the correction function. Figure 3, which does not contain the boundary correction function, is a measure of the SPH method. The instability of the SPH method proves that the GRK correction function is enhancing stability of the solution as well as correcting the reconstruction near the boundaries.

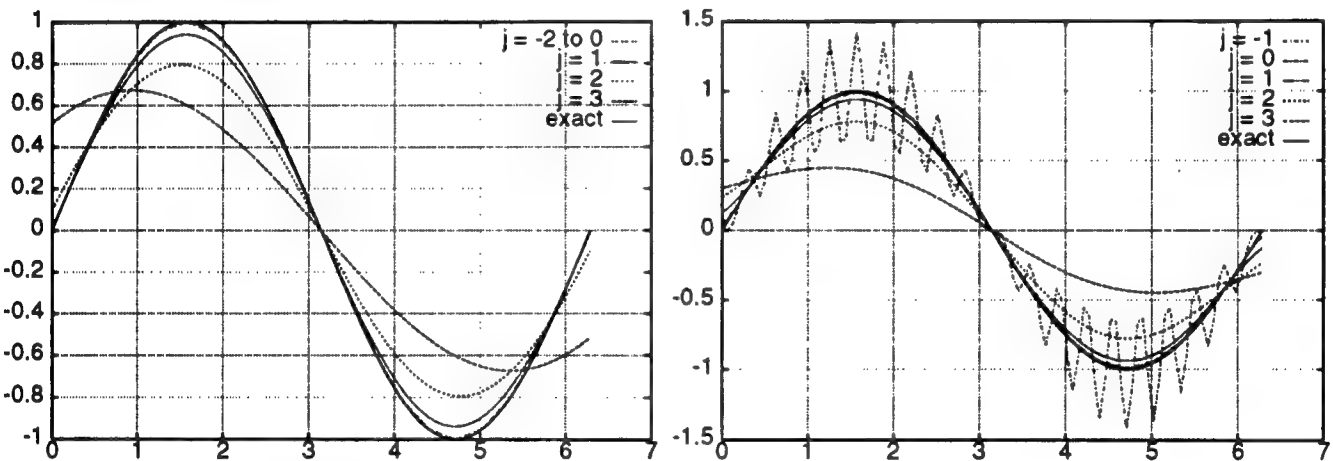


Figure 3 {Left} $\sin(x)$ reconstruction using the GRK, 21 Nodes.
 Figure 4 {Right} $\sin(x)$ reconstruction for $\sin(x)$ using 21 nodes.

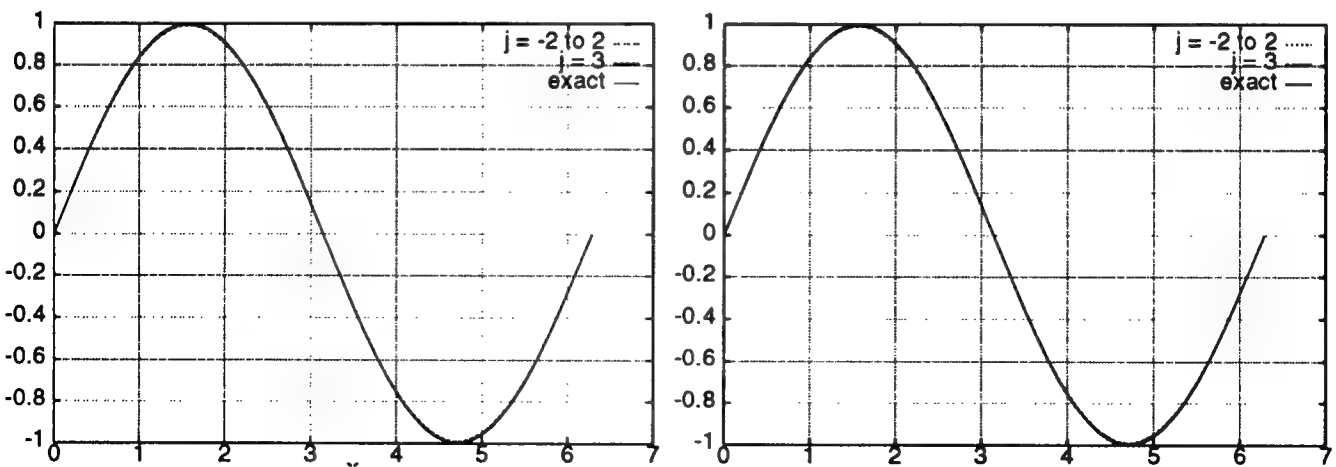


Figure 5 {Left} $\sin(x)$ reconstruction using the GRK, 201 Nodes.
Figure 6 {Right} SPH reconstruction for $\sin(x)$ using 201 nodes.

It is important to note that $j = -2$ was not plotted in figure 4 since the instability of SPH method would have required a much larger scale. This occurs because the SPH kernel does not satisfy the consistency condition for small number of nodes; however, for large numbers of nodes the SPH method performs adequately (figure 6).

Knowing the behavior of the dilation parameter, namely the effect of the j parameter, our discussion is turned toward a brief look at the frequency content of the window function. By dilating the Gaussian function (figure 1), it is easily seen how the function changes shape with the parameter j . It is this dilation that enables the types of analyses discussed in section 2.6.

A reconstruction is now performed on a sinusoidal wave that has been augmented to increase its frequency as well as dampen its amplitude.

$$f(x) = \sin\left(\frac{\pi}{2}(x + .6x^2)\right) e^{-0.1x} \quad (3.0.1)$$

The results in figure 7 clearly show the ability of the window function to capture more or less of the frequency content. The larger the values for the refinement parameter the more quickly the reconstruction attempt fails.

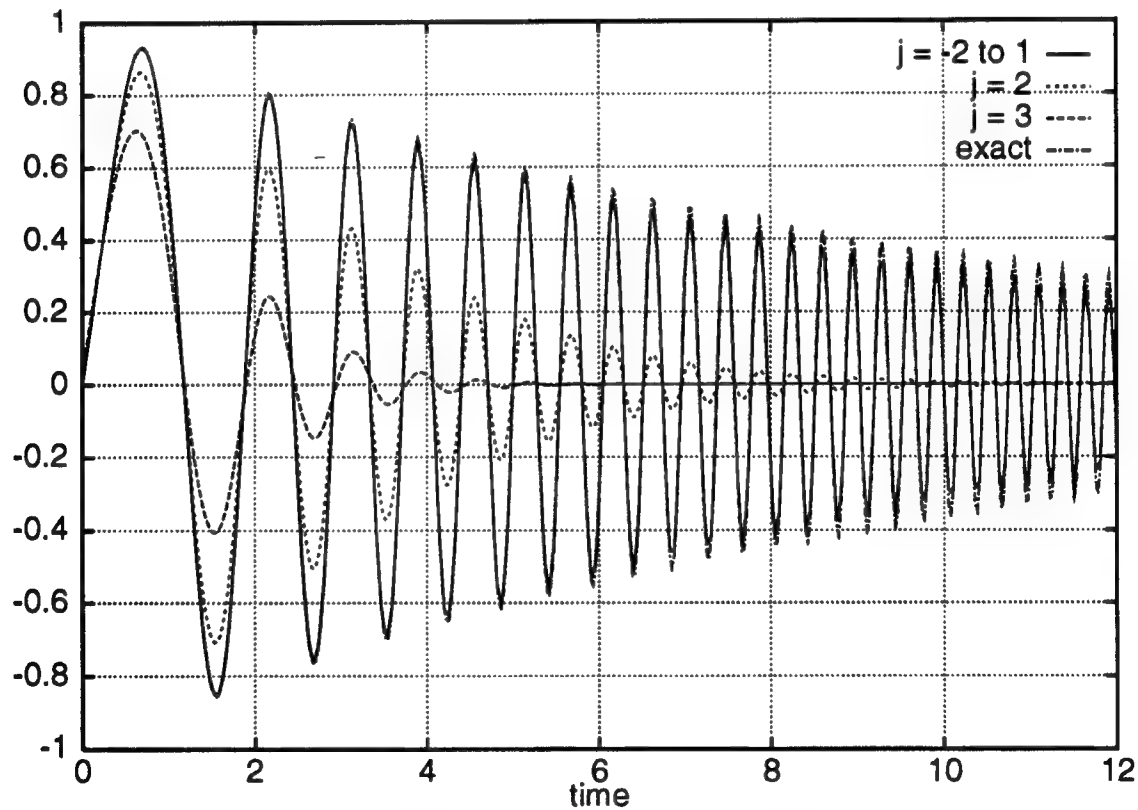


Figure 7 The reconstruction of a sine wave with increasing frequency and damped oscillations for several values of j with 201 nodes.

4.0 Galerkin GRK Formulation

The reproducing kernel can be implemented into a Galerkin formulation in a similar way as typical finite elements. The major difference in construction is the loop occurs over nodes instead of elements, but the formulation is almost identical beginning from the weak form of the momentum equation. The following variables are used: t is the traction, b is the body force, s is the stress tensor, and \ddot{u} denotes acceleration.

$$\int_{R_x} \rho \delta u_i \ddot{u}_i \, dR_x + \int_{R_x} \delta u_{i,j} \sigma_{ij} \, dR_x = \int_{R_x} \delta u_i b_i \, dR_x + \int_{\partial R_x^t} \delta u_i t_i \, d\Gamma_x \quad (4.0.1)$$

This paper analyzes a one dimensional bar with a step force applied at one end (figure 10). The element matrices are simple, included a lumped mass matrix, but it is important to keep in mind that the matrices have a variable connectivity depending on the number of nodes in the support of the window function, NEN .

$$\{m_{ab}^e\} = \left\{ \int_{R_x^e} \rho_o^e N_a N_b 1 \, dR_x^e \right\} \quad a, b = 1, \dots, NEN \quad (4.0.2)$$

$$f^{int}(x, \sigma)^e = \{(f_a^{int})^e\} = \left\{ \int_{R_x^e} \sigma^e N_{a,x} \, dR_x^e \right\} \quad a = 1, \dots, NEN \quad (4.0.3)$$

$$f^b(x, b)^e = \{(f_a^b)^e\} = \left\{ \int_{R_x^e} N_a b^e \, dR_x^e \right\} \quad a = 1, \dots, NEN \quad (4.0.4)$$

$$f^t(x, t)^e = \{(f_a^t)^e\} = \left\{ \int_{\partial R_x^t \cap \partial R_x^e} N_a t^e \, d\Gamma_x^e \right\} \quad a = 1, \dots, NEN \quad (4.0.5)$$

It is also difficult to implement the boundary conditions since several shape functions can be present at the node dictating the necessary response. The natural boundary conditions are simply entered into the force vector; however, the essential boundary conditions are more difficult to satisfy. In this analysis the essential boundary condition is satisfied by substituting a sum on all the shape functions in place of the row in the stiffness matrix that corresponds to the constrained nodes. The shape function and its derivative are derived with the correction function in the next two sections.

4.1 Properties of the Shape Functions

Using the final form of the continuous reproducing kernel (found in section 2.4), it is quite easy to obtain the familiar form of a Galerkin approximation. If the equation is now numerically integrated and terms are grouped to follow the standard technique, the shape

$$u^h(x) = \sum_{J=1}^{NP} N_J(x) u_J \quad (4.1.1)$$

$$u(x) = \sum_{J=1}^{NP} \left[C_1 + C_2 \left(\frac{x - x_J}{r} \right) \right] \frac{1}{r} \Phi \left(\frac{x - x_J}{r} \right) u(x_J) \Delta M_J \quad (4.1.2)$$

$$N_J(x) = \left[C_1(x) + C_2(x) \left(\frac{x - x_J}{r} \right) \right] r^{-1} \Phi \left(\frac{x - x_J}{r} \right) \Delta M_J \quad (4.1.3)$$

The characteristics of this new shape function must be carefully analyzed to avoid erroneous results. The most apparent difference is that the shape function does not meet the Kronecker delta identity since each node is influenced by several shape functions. However, the shape function will meet the consistency condition. This can be proven by the following equation (4.1.4) where the reconstruction equation can be substituted to reproduce itself. It is also pointed out that the integration method used to calculate C and C^{-1} must be similar in order to cancel and meet this condition. It is also proposed by Liu[93] that by using the Trapezoidal Rule to integrate the moments defined within C , the stability of the kernel is increased.

$$\begin{aligned} P(x) &= \int_{R_x} \rho P(x) C^{-1}(x) P^T(s) \Phi \left(\frac{s - x}{r} \right) P(s) ds \\ &= P(x) C^{-1}(x) \int_{R_x} \rho P^T(s) P(s) \frac{1}{r} \Phi \left(\frac{s - x}{r} \right) ds \\ &= P(x) \end{aligned} \quad (4.1.4)$$

The shape functions will meet the following isoparametric shape function properties.

$$\sum_{J=1}^{NP} N_J(x) = 1 \quad \text{and} \quad \sum_{J=1}^{NP} N_J(x) x_J = x \quad (4.1.5)$$

4.2 Shape Function Derivatives

Unlike the Moving Least Square Methods, Diffuse Element Methods, and Element Free Galerkin Methods, the derivative of the GRK shape function can simply be obtained by differentiation. It is necessary to consider the correction terms as well as the window function itself to obtain the derivative of the shape function.

$$\begin{aligned} N_{J,x}(x) &= \left\{ C_1(x) + C_2(x) \left(\frac{x - x_J}{r} \right) + \frac{C_2(x)}{r} \right\} r^{-1} \Phi \left(\frac{x - x_J}{r} \right) \Delta M_J \\ &+ \left\{ C_1(x) + C_2(x) \left(\frac{x - x_J}{r} \right) \right\} \frac{1}{r} \Phi' \left(\frac{x - x_J}{r} \right) \Delta M_J \end{aligned} \quad (4.2.1)$$

$$C_2 = \frac{m_1}{m_0 m_{11} - m_1^2} - \frac{m_1 (m_0 m_{11} + m_0 m_{11} - 2m_1 m_1)}{(m_0 m_{11} - m_1^2)^2} \quad (4.2.4)$$

Now it is necessary to calculate the derivatives of the moments which can be combined with the derivative of the Gaussian window function to reveal the final derivative in equation (4.2.8).

$$m'_0(x) = \int_{B(x)} \frac{2}{r^2 \sqrt{\pi}} \left(\frac{x-s}{r} \right) e^{-\left(\frac{x-s}{r} \right)^2} ds \quad (4.2.5)$$

$$m'_1(x) = \int_{B(x)} \frac{1}{r^2 \sqrt{\pi}} \left[2 \left(\frac{x-s}{r} \right)^2 - 1 \right] e^{-\left(\frac{x-s}{r} \right)^2} ds \quad (4.2.6)$$

$$m'_{11}(x) = \int_{B(x)} \frac{2}{r^2 \sqrt{\pi}} \left(\frac{x-s}{r} \right) \left[\left(\frac{x-s}{r} \right)^2 - 1 \right] e^{-\left(\frac{x-s}{r} \right)^2} ds \quad (4.2.7)$$

$$N_{J,x}(x) = \left\{ C_1(x) + C_2(x) \left(\frac{x-s}{r} \right) + \frac{C_2(x)}{r} \right\} r^{-1} \Phi \left(\frac{x-s}{r} \right) \Delta M_J \quad (4.2.8)$$

$$- \frac{2}{r} \left\{ C_1(x) + C_2(x) \left(\frac{x-s}{r} \right) \right\} \left(\frac{x-s}{r} \right) r^{-1} \Phi \left(\frac{x-s}{r} \right) \Delta M_J$$

5.0 Stability Analysis

It is interesting to note that the stability of this type of analysis is two-fold. First there is the stability of the Reproducing Kernel itself, and then there is the stability of the time integration method. In this analysis an Explicit Newmark Beta Predictor/Corrector Type algorithm is implemented (Hughes and Liu [78]).

5.1 Reproducing Kernel Stability

The stability of the kernel is mainly a function of the number of nodes encompassed by the Gaussian window function. (Theoretically the number of nodes covered is the number of nodes in the analysis, since the function has an infinite domain.) The number of significant nodes in a shape function is controlled by the refinement parameter, r . From the aforementioned definitions for the shape of the window function the following equation can be derived to estimate the number of nodes under any given window function. If the radius of a given window function, Dx_C , is defined as the distance from the center to the edge of the windows significant support .

Then a ratio can be defined to relate the height of the Gaussian function at the peak to the small value where it is safely approximated to be zero.

$$\Delta x_c = \Delta x \left(\frac{n-1}{2} \right) \quad (5.1.2)$$

Using these definitions it is possible to derive the kernel stability stated in equation (5.1.3) where the variables are as follows.

n = the number of nodes covered by the Gaussian function

j = the parameter controlling the dilation

R = the ratio between the value at a node in the tails of the function to the significance of the peak of the Gaussian function.

$$n = 1 + \sqrt{\frac{-2 \ln R}{\pi}} * 2^{j+1} \quad (5.1.3)$$

Theoretically the number of nodes should be at least two in order to maintain the variable connectivity window arrays. This is verified analytically through solutions that were run with values as low as -2.5 for j when the entire domain is used as the support of the Gaussian function, and as low as -2.2 when the support of the Gaussian function is limited. Solutions for the number of nodes in the support of a window function for various height ratios are shown in the following

j	n (2s)	n (3s)
-2.2	1.69	2.04
-2	1.80	2.20
-1	2.60	3.39
0	4.19	5.79
1	7.38	10.57
2	13.77	20.15
3	26.53	39.30

NOTE: 2s and 3s corresponds to $R = 1.83e-2$ and $R = 1.23e-4$ respectively.

5.2 Critical Time Step

In order to perform analyses on the structural dynamic class of problems, it is very important to understand the relationship between this new shape function and the critical time step. This is determined here by performing the standard eigenvalue analysis, solving the determinant of $[K - \omega^2 M]$. This calculation only needs to be performed for the element case since it is known that the maximum element frequency determines the upper bound for the critical time step. The critical time step was found to depend on several parameters including the dilation parameter and the boundary correction function.

Using symbolic manipulation this determinant was solved for GRK shape functions containing several different numbers of nodes. By evaluating the determinant it was found that there is only one non-zero eigenvalue, regardless of the number of nodes in the support of the shape function. The result was able to be simplified for equally spaced nodes to equation (5.2.3) by defining the following terms.

$$D(x, s) = C_1(x) + C_2(x) \left(\frac{x-s}{r} \right) \quad (5.2.1)$$

$$D'(x, s) = C_1'(x) + C_2'(x) \left(\frac{x-s}{r} \right) + \frac{C_2(x)}{r} \quad (5.2.2)$$

$$\lambda_{max} = \left(\frac{2c^2}{l^2} \right) r^2 \sum_i^{NP} [D_i \Phi_{xi} + D'_i \Phi_{xi}]^2 \Delta x_i \quad (5.2.3)$$

where

dx is the length between nodes (density = 1)

Dx_i is the integration weight using Trapezoidal Rule

NP is the number of nodes in the shape function's support

Finally, the critical time step is shown for a central difference time integration scheme in equation (5.2.4). By substituting the maximum eigenvalue corresponding to the maximum frequency, the critical time step can be calculated.

$$\Delta t \leq \frac{2}{\omega_{max}} \quad (5.2.4)$$

$$\Delta t \leq \frac{l}{c} \left(\frac{\sqrt{2}}{r} \right) dx \left[\sum_i^{NP} [D_i \Phi_{xi} + D'_i \Phi_{xi}]^2 \Delta x_i \right]^{-1/2} \quad (5.2.5)$$

Results for the critical time step were calculated using equation (5.2.5). The results are shown in the following table for 21 nodes. This can be compared to the standard finite element $\Delta t \leq l/c$ which is 2.455×10^{-5} s.

j	Δt (Analytic)	Δt (Numeric)
-1	2.456×10^{-5}	2.432×10^{-5}
0	3.473×10^{-5}	3.223×10^{-5}
1	4.912×10^{-5}	5.651×10^{-5}

The discretized form of the critical time step was perceived to have an simple translation to the continuous form. The discretized form contains the derivative of the reproducing kernel squared. Then the largest eigenvalue and thus the critical time step is as follows:

$$\lambda = \left(\frac{2c^2}{l^2} \right) r^2 \int_{B(x)} \left[D(x,y) \Phi \left(\frac{x-y}{r} \right) + D'(x,y) \Phi \left(\frac{x-y}{r} \right) \right]^2 dy \quad (5.2.6)$$

$$\lambda = \left(\frac{2c^2}{l^2} \right) r^2 \int_{B(x)} k_{,x}(x,y)^2 dy \quad (5.2.7)$$

where $k(x,y)$ is the reproducing kernel defined by equation (5.2.8).

$$k(x,y) = D(x,y) \Phi \left(\frac{x-y}{r} \right) \quad (5.2.8)$$

steel) $E = 3 \times 10^7$ psi, $\tau = 7.24 \times 10^{-4}$ slugs/in³, and $A = 1$ in². For the elastic - plastic problem, yield stress $\sigma_y = 30000$ psi, $E_p = E/4$ and $F_0 = 5000$ lb are employed.

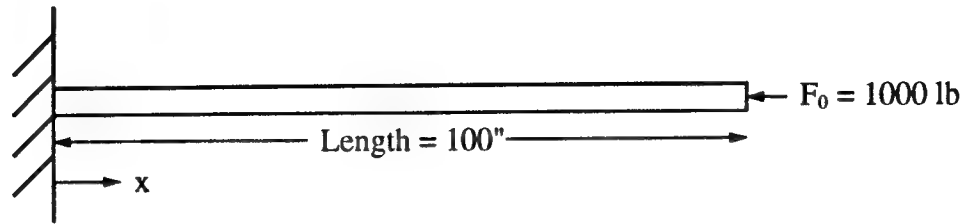


Figure 8 1-D linear elastic rod with step input.

The solution for the linear elastic deforming rod was obtained with the GRK and a Explicit Newmark-Beta predictor/corrector algorithm. These results coincided accurately with the closed form solution.

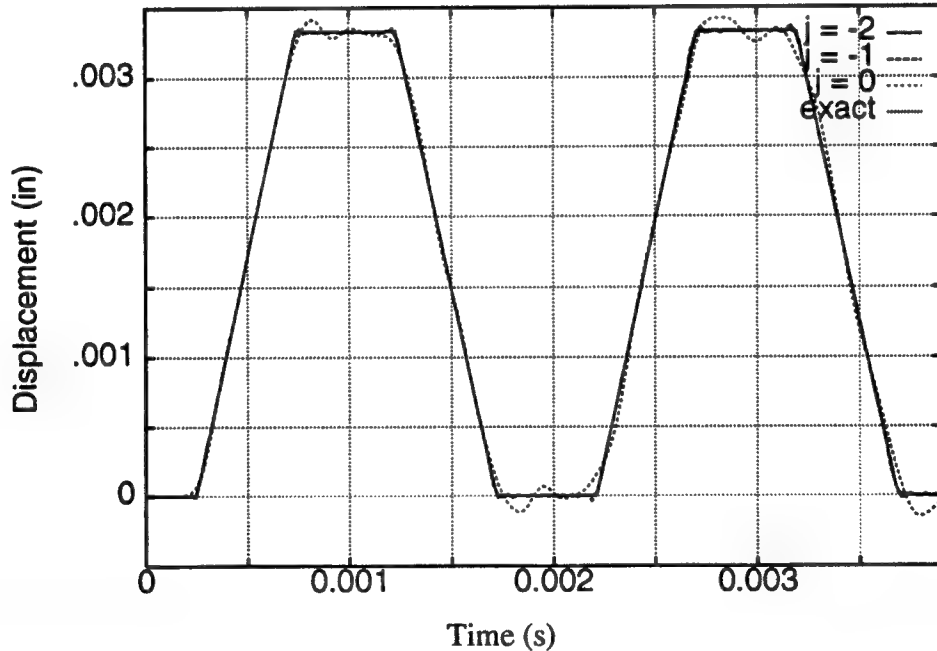


Figure 9 Displacement for node 11 (center node) showing a range for the dilation parameter and the exact solution.

In order to visualize the effect of the dilation parameter in this application, the shape function are plotted in figure 10 along with the nodes which depicts the number of significant nodes providing the support of each shape function in each dilation (Technically every node is in the support of every Gaussian shape function.) This is shown directly above the plot for velocity

versus time which incorporated the shape functions in figure 10 to obtain this response (figure 11).

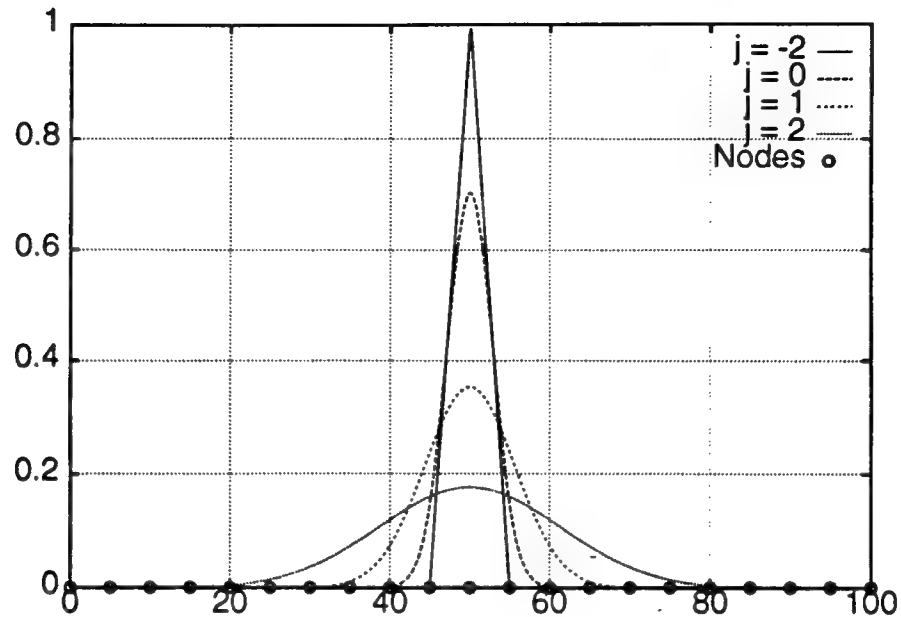


Figure 10 Shape functions used to calculate the wave propagation, with nodal support.

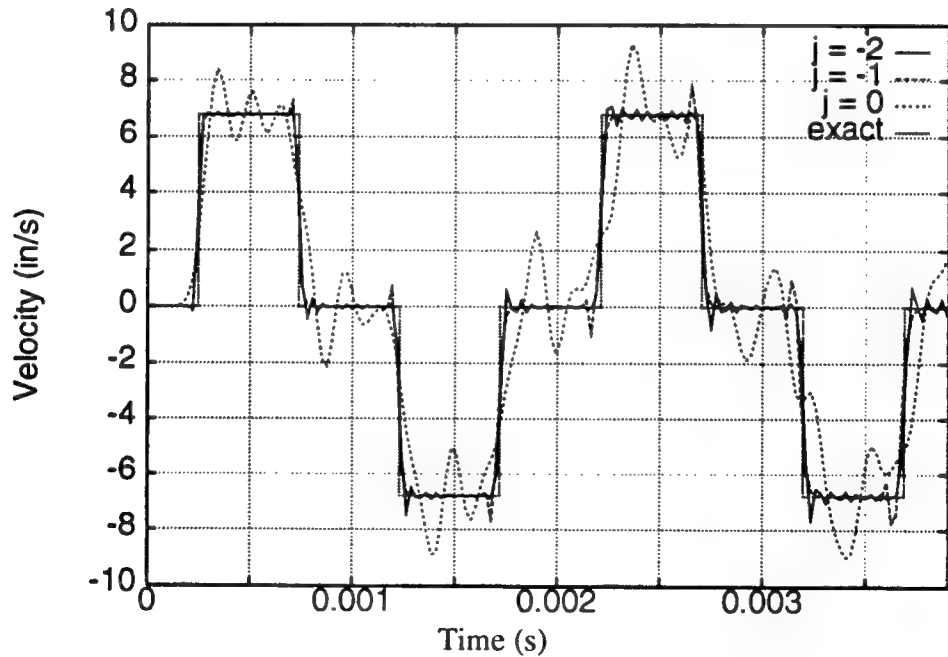


Figure 11 Velocity for node 11 (center node) showing a range for the dilation parameter and the exact solution.

For completeness the stress is also plotted, figure 14.

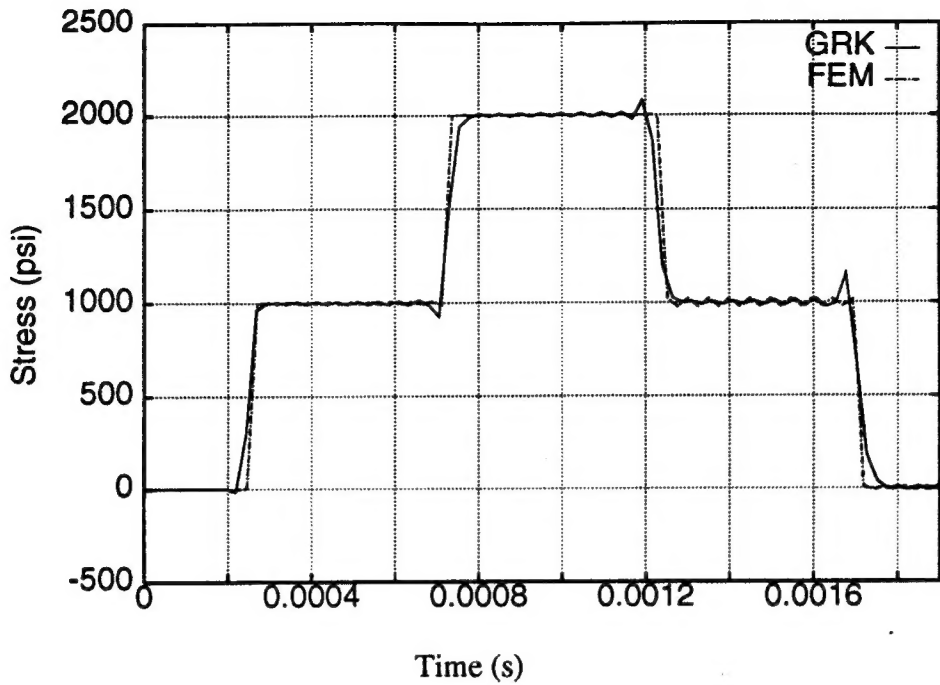


Figure 12 The axial stress is plotted for the middle node versus time.

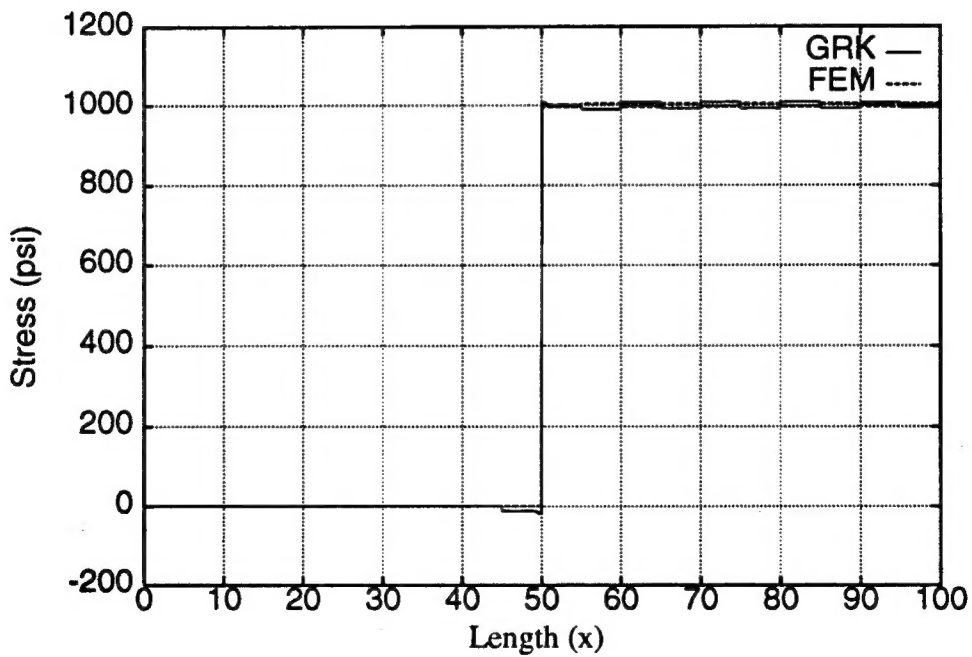


Figure 13 Axial stress at the tenth time step as a function of position.

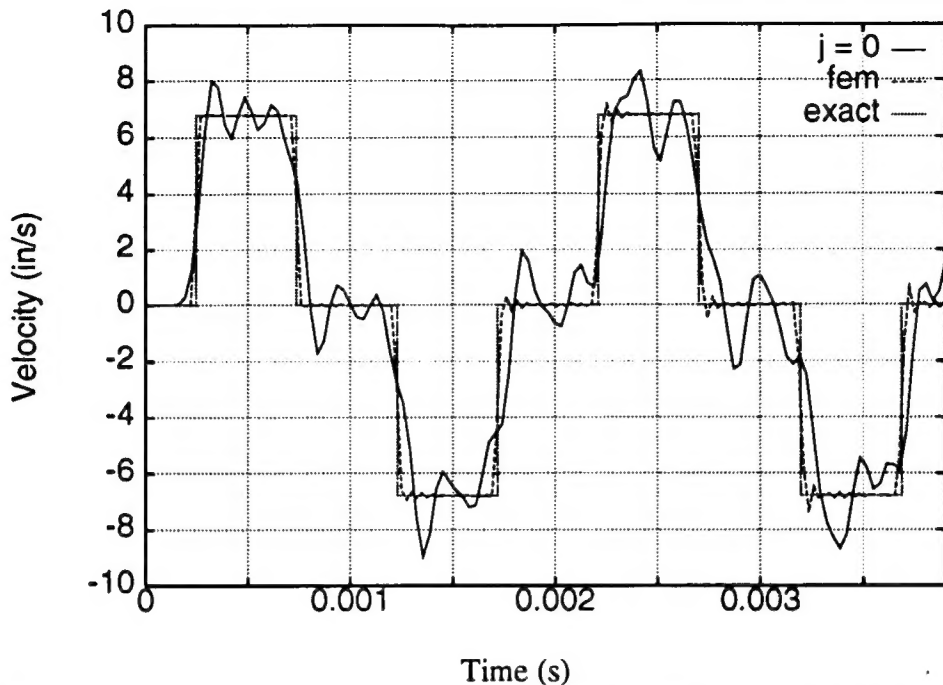


Figure 14 GRK run with $j = 0$ and a time step of 3.32×10^{-5} which is 1.35 times the FEM critical step.

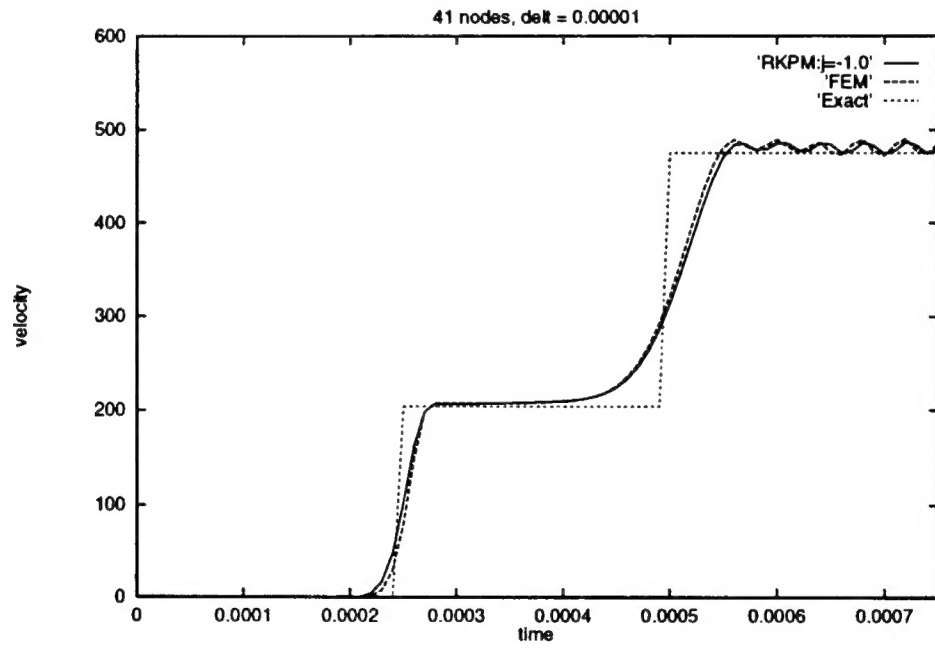


Figure 15 Elastic-plastic responses at the midpoint of the rod.

Although the solution in figure 14 is not as accurate as the finite element solution, it is interesting to note that the problem was run at 1.35 times the FEM critical time step.

7.0 Conclusions

The theory for a Gaussian Reproducing Kernel is presented here with numerical experiments performed to confirm the derived equations. The GRK method is proven here to possess the ability to solve a dynamic problem. Results are also presented to verify the supposition that the correction function can provide both boundary correction and reproducing kernel stability. Furthermore the implementation of the flexible window function as frequency control has been initiated.

The results from the numerical experiments not only verified the theory presented, but it produced several encouraging results. Among the most important is the ability of the Gaussian Reproducing Kernel to perform at time steps larger than the critical time step for standard finite elements. It is also important that results for the correction function proved that it provided boundary correction as well as enhancing the stability of the reconstruction equation. The increased stability of the reconstruction equation enables the ability to use fewer particles in analyses. The correction function increased the stable range of the dilation parameter over the SPH method.

The advantageous characteristics of the GRK were not able to produce superior results over the standard finite element method due to the finite element's inherent ability to solve this elastic-dynamic problem exactly when run at the critical time step. Nonetheless, the theory has been derived and it is logical that characteristics such as continuous derivatives, flexible window filtering, and the kernel's increased stability, and increased critical time step ability are valuable tools that can be exploited in further experiments.

Acknowledgments

The support of this research by AFSOR grant number F49620-92-J-0505, NSF grant number MSS-9015978 and ONR grant number N00014-93-I-0292 to Northwestern University is gratefully acknowledged.

References

Belytschko, T., Lu, Y. Y. and Gu, L., "Element Free Galerkin Methods", (1993). (*preprint*)

Chui, C. K., An Introduction to Wavelets, Academic Press (1992).

Daubechies, I., Ten Lectures on Wavelets, CBMS/NSF Series in Applied Mathematics, No. 61, SIAM Publication [1992].

Hughes, T.J.R., The Finite Element Method, Prentice-Hall Inc., (1987).

Hughes, T.J.R., and Liu, W.K., "Implicit-Explicit Finite Elements in Transient Analysis," *Journal of Applied Mechanics*, 45, pp. 371-378, (1978).

Gingold, R. A. and Monaghan, J. J., "Smoothed Particle Hydrodynamics: Theory and Application to Non-Spherical Stars", *Mon. Not. Roy. Astron. Soc.*, 181, 375-389 (1977).

Johnson, G. R., Peterson, E. H. and Stryk, R. A., "Incorporation of An SPH Option into The EPIC Code for A Wide Range of High Velocity Impact Computations", (1993) (*preprint*).

Lancaster, P. and Salkauskas, K., "Surfaces Generated by Moving Least Squares Methods", *Mathematics of Computation*, 37, 141-158 (1981).

Libersky, L. D. and Petschek, A. G., "Smooth Particle Hydrodynamics With Strength of Materials", *Advances in the Free-Lagrange Method, Lecture Notes in Physics*, **395**, 248-257 (1990).

Liu, W.K., Zhang, Y., Belytschko, T., Jun, S., Adey, J., Gu, L., "Reproducing Kernel Particle Methods", *International Journal of Numerical Methods in Fluids*, Submitted May (1993).

Liu, W. K., Zhang, Y. and Ramirez, M. R., "Multiple Scale Finite Element Methods," *International Journal for Numerical Methods in Engineering*, **32**, 969-990, (1991).

Monaghan, J. J., "Why Particle Methods Work", *SIAM J. Sci. Stat. Comput.*, **3**, 422-433, (1982).

Monaghan, J. J., "An Introduction to SPH", *Comp. Phys. Comm.*, **48**, 89-96, (1988).

Nayroles, B., Touzot, G. and Villon, P., "Generalizing The Finite Element Method: Diffuse Approximation and Diffuse Elements", *Computational Mechanics*, **10**, 307-318, (1992).

AIR FORCE SCIENTIFIC RESEARCH (AFSC)
NOTICE OF TRANSMISSION TO DTIC

This technical report has been reviewed and is
approved for public release IAW AFR 190-12
Distribution is unlimited.

Joan Beagle
STINFO Program Manager

Approved for public release;
distribution unlimited.